LIST OF FIGURES

LIST OF TABLES

CHAPTER 1

INTRODUCTION

1.1 Overview

In recent years, wood-plastic composites (WPCs) have been widely used as building materials. This, fairly new, material has a lot of desirable characteristics, such as low density, non-toxic, recyclable, and low abrasive finish (Clemons, 2002).

The mechanical performance of WPCs depends on the inherent properties of the constituent materials, interactions between these materials, processing, product design, and service environment. The increased use of this material has made it essential for researchers and engineers to perform mechanical and computer analysis for material characterization.

Considering the material performance and advantages, there is a strong potential for this material to be used in the wind energy industry (Brøndsted, Lilholt, & Lystruo, 2005).

Wind energy is one of the key solutions to the global energy problem. Different types of wind turbines have been manufactured to convert the kinetic energy of the wind into electricity. One of the main parts of a wind turbine is the rotorblades. In a typical wind

turbine, the rotor and its three rotorblades constitute a flimsy structure, consisting of cantilever-mounted blades on a central hub.

Different types of materials such as wood, aluminium, and composites have been used in the manufacturing of rotorblades. Carbon and glass fibre composites are the main candidates in material selection for this industry. However, to the best of our knowledge, WPCs have not been developed on an industrial scale to manufacture rotorblades (Brøndsted, Lilholt, & Lystruo, 2005).

In cold climate regions such as Canada, the performance of the materials at cold temperatures is one of the decisive factors in material selection. In cold regions, wind turbines are exposed to severe conditions characterized by temperatures below $-50°C$ and wind speeds sometimes exceeding 25 m/s. Therefore, it is essential to have a complete knowledge of the material properties in these extreme conditions.

In order to investigate the application of WPCs in the rotorblades industry, the first step is to study the mechanical behaviour of this material under the operational conditions of a wind turbine.

The next step is to look into the material requirements relevant to the rotorblades industry. The operational parameters and conditions require the material to have a high stiffness, low density, and long fatigue life. Therefore, the material selection will be carried out by comparing the performance of the material with the requirements.

1.2 Problem description

The mechanical properties of WPCs at high temperatures and thermoforming temperatures have been investigated by many researchers (Erchiqui, Derdouri, Gakwaya, Godard, & Garcia-Rejon, 2001). Several studies are focused on hyperelastic and viscoelastic behaviour of this material at different temperatures (Erchiqui, Ozdemir, Souli, Ezzaidi, & Dituba-Ngoma, 2011) (Feng, 1992) (Joye, Poehlein, & Denson, 1973).

Several experimental approaches have been used to determine the mechanical properties of thermoplastics (Treolar, 1944) (Joye, Poehlein, & Denson, 1973) (Alexander, 1971). However, thus far, the mechanical behaviour of WPCs at cold temperatures has not been investigated. In this project the bubble inflation technique is used to characterize the behaviour of the specimens at cold temperatures.

Considering several advantages of WPCs such as being non-toxic and recyclable, there is a growing interest in the application of this material in the rotorblades industry. Therefore, this study was motivated by the need to understand the behaviour of this material at cold temperatures and investigate its application in the industry. It was carried out under a grant from NSERC/Hydro-Quebec/UQAC Industrial Chair on Atmospheric Icing of Power Network (INGIVRE) at the University of Quebec at Chicoutimi.

1.3 Research objectives

1.3.1 General objective

This PhD project focuses on the material characterization for wood-plastic composites and the development of their application in the construction of rotorblades for wind turbines in cold climate regions.

1.3.2 Specific objectives

To achieve the general aim of the project there are specific objectives that need to be fulfilled. The specific objectives are as follows:

- **Experimental modelling of the material deformation:** the composite materials used in this project are provided by the plastic laboratory at UQAT. The HDPE samples are also prepared from the same HDPE sheet that is used in the manufacturing of WPC specimens. In this project, the bubble inflation technique that was introduced by Joye (Joye, Poehlein, & Denson, 1973) is selected as the experimental approach. This selection is justified due to the accuracy of this method in large deformation experiments and simple boundary conditions in spherical coordinates. The experimental setup is to model the free-flow of thin circular membranes under the effect of pressure. In this context, it is necessary to establish an experimental setup that is robust and provides accurate data for mechanical modelling. The experimental setup is designed according to the instructions

provided by the co-director of the project and is prepared at CIGELE laboratory of UQAC. It is also important to develop the mathematical model of the bubble inflation and understand the boundary conditions of the experiments. The quality of the experimental results plays a significant role in material characterization.

- **Finite element modelling:** This objective is to tackle the computer modelling aspects of the project. The aim of the computer modelling is to provide a learning library for the Artificial Neural Networks in order to obtain the optimum material constants. Abaqus, as a finite element package, is used to model the elastic and hyperelastic behaviour of the specimens at different temperatures. A membrane with the same dimensions and boundary conditions as the experiments is modelled in Abaqus for the purpose of finite element modelling.
- **Determining the optimum material constant:** As mentioned above, the main objective of this project is to determine the material constants for elastic and hyperelastic constitutive equations. This goal is achieved by using the neural network. Although the neural network toolbox is available in Matlab, for the purpose of this study, the neural network code is developed in order to obtain more accurate results.
- **Results verification:** It is very important to verify the results from the neural network as valid material constants. For this purpose, a set of wind tunnel experiments are carried out to measure the deformation of the specimens. Furthermore, the experimental results are compared with results from the computer

simulations in order to estimate the error between deformation values measured in experiments and computer modelling.

- **Rotorblades application:** After verifying the material constants, the application of WPCs is investigated in the rotorblades industry. The mechanical performance of WPCs is compared with the material requirements relevant to the industry in order to perform the material selection.

1.4 Methodology

The methodology describes how each of the aforementioned objectives will be addressed. The wood-plastic composite specimens used in this project were manufactured at the plastic laboratory of UQAT. The polymer matrix of the composite is HDPE and its melting point is 135°C. The coupling agent used is Fusabond 226DE Dupont. The amount of coupling agent used is 3% of the total weight of the composite. This amount was found to be optimal in order to improve the homogeneity of the matrix, ensuring better distribution of the fibres in the polymer matrix. In the composite, wood is in the form of sawdust that was previously dried. Five different mass concentrations of fibres were produced: 20, 30, 40, 50, and 60wt%. At the end, circular samples with a diameter of 79.2 mm were prepared.

The purpose of the experimental modelling is to plot the pressure changes against the bubble height at the pole of the membrane. The system is installed in the cold room to run the tests at cold temperatures. The effects of different pressures and temperatures are

tested on the formation of the bubble. The temperature range is $-50°C$ to $+50°C$ and the inflation time is a few seconds. The test setup is equipped with a pressure gauge that can measure the pressure inside the bubble. A position sensor is used to monitor the height at the centre of the membrane. The sensor measures the height of the bubble without direct contact with the target.

The setup that is used for the experiments consists of a cold chamber and a set of instruments used to control, regulate, and monitor the process. The instruments are a pressure regulator, a flow meter, two pressure sensors, two temperature sensors, a laser sensor, a data acquisition card, a transmitter, and a computer. On the computer the LabVIEW software is installed to collect the information from the sensors and data acquisition card.

Finite element modelling is carried out in Abaqus, under the licence that has been purchased by CIGELE laboratory. In this step, the deformation of different membranes at different temperatures is modelled with various material constants. Young's modulus and C_1 represent the material constants for elastic and hyperelastic models, respectively. For each membrane at each temperature a minimum number of six simulations are done to increase the accuracy of the material characterization.

The optimum material constants are obtained by applying the neural network. A supervised learning neural network is used for this purpose. The architecture selected is the

Multilayer Perceptron with back-propagation of error. A sigmoid function is used as the transfer function of the neurons in the hidden layer.

Results verification is done by a set of wind tunnel experiments on an HDPE sheet at three different temperatures: 0°C, −15°C, and −30°C. At each temperature the deformation under four different wind speeds (10, 15, 20, and 25 m/s) is monitored.

At the final step, the application of WPCs in the rotorblades industry is investigated by comparing the material performance with the material requirements relevant to the industry.

1.5 Statement of originality and contribution to knowledge

To the best of our knowledge, the application of wood-plastic composites in the rotorblades industry has not yet been investigated, despite several advantages of this fairly new material (Brøndsted, Lilholt, & Lystruo, 2005). Furthermore, the mechanical behaviour of this material has not yet been characterized at cold temperatures such as −25°C and −50°C (Erchiqui, Derdouri, Gakwaya, Godard, & Garcia-Rejon, 2001).

The application of the neural networks in material characterization and the learning library obtained from Abaqus are unique to this project and has not yet been used. Moreover, the results verification by means of wind tunnel experiments and Abaqus has contributed significantly to the quality of the results obtained in this project.

This study is the first to use the bubble inflation technique to characterize the polymeric materials at cold temperatures. It is also the first study that reviews the application of WPCs in the rotorblades industry for cold climate regions. Carbon and glass fibres have been widely used in this industry, but WPCs have not yet been developed on an industrial scale to manufacture rotorblades.

The originality of the project is not limited to the originality of concept but extends to the unique approach taken to fulfil the main objective. This fact is mostly owing to the strategy that is used in this project of amalgamating the experimental approach, finite element modelling, and the Artificial Neural Networks results in order to find the optimum materiel constant.

1.6 Thesis outline

The dissertation is structured as follows:

Chapter one provides general information of the subject and defines the problem that is tackled in this project. The general and specific objectives are defined and the methodology of the work is explained. Finally, the originality of this study and its contribution to the current knowledge is presented.

Chapter two includes general information on the subject with a detailed review of the current literature. It introduces the wood-plastic composites and their current application in various industries. Previous studies on polymeric materials and different

experimental approaches are investigated. Furthermore, the fundamental knowledge of wind turbines, rotorblades, and material selection for the rotorblades industry are presented. The elastic and hyperelastic behaviour of the materials with a brief description of neural networks are reviewed.

Chapter three presents the experimental modelling of the project. The selection of the experimental approach with a description of the constituent parts is provided. The sample preparation and conditions of the experiments are explained in detail. The mathematical model of the bubble inflation is reviewed in order to better understand the boundary conditions of the tests.

Chapter four explains the computer modelling aspects of the project. The elastic and hyperelastic behaviour of the specimens are modelled in Abaqus. At the end of this chapter, the stress distribution in the membrane under pressure, and the values of von Mises principal stresses are provided.

Chapter five opens with a detailed study of the Artificial Neural Networks (ANNs). Their application in this project is explained in detail in order to obtain the optimum material constants. Finally, the material requirements for the rotorblades industry are compared with the material constants obtained in this project and the final material selection is performed.

Chapter six is used to verify the results of the project using a set of wind tunnel experiments and modelling. At the end of this chapter, a review of the effects of humidity and icing on WPCs and rotorblades is provided.

Chapter seven constitutes the conclusion of this study and gives a number of recommendations with respect to future work.

CHAPTER 2

LITERATURE REVIEW

2.1 Introduction

In this chapter a review of the relevant literature is presented, in order to better understand the principles of the project and explain the basic concepts pertinent to the work.

First, wood-plastic composites are introduced and the previous studies and different experimental approaches for material characterization are investigated. Furthermore, the fundamental knowledge of wind turbines, rotorblades, loading conditions, material requirements, and material selection for the rotorblades industry are presented.

Finally, the elastic and hyperelastic behaviour of materials is reviewed, followed by a brief description of the Artificial Neural Networks.

2.2 Wood-plastic composites

In recent years, there has been an increasing interest in the development of wood-plastic composites (WPC) for use as building materials, due to the abundance, low cost, and processability of wood as a filler. One reason that this fairly new material has outperformed

competing plastic products in decking is that the addition of wood filler is an effective way to increase product stiffness, although strength usually suffers (Clemons, 2002).

Using natural reinforcements such as wood in composite materials, instead of mineral reinforcements, has several advantages such as low density, low cost, and a less abrasive finish. The natural reinforcements are also non-toxic and recyclable.

The term wood-plastic composite refers to any composites that contain wood (of any form) and thermosets or thermoplastics. Thermosets are plastics that, once cured, cannot be melted by reheating. These include resins such as epoxies and phenolics. Thermoplastics are plastics that can be repeatedly melted, such as polyethylene and polyvinyl chloride (PVC) (Clemons, 2002). This study focuses on wood-thermoplastic composites, which are most often simply referred to as wood-plastic composites (WPCs) with the understanding that the plastic component is a thermoplastic.

Because of the limited thermal stability of wood, only thermoplastics that melt or can be processed at temperatures below 200°C are commonly used in WPCs. Currently, most WPCs are made with polyethylene, both recycled and virgin, for use in exterior building components. However, WPCs made with wood-polypropylene are typically used in automotive applications and consumer products, and these composites have recently been investigated for use in building profiles. Polystyrene and Acrylonitrile-butadiene-styrene (ABS) are also being used. The plastic is often selected based on: its inherent

properties, availability, and cost; the product need; and the manufacturer's familiarity with the material (Clemons, 2002).

The wood used in WPCs is most often in particulate form (e.g., wood flour) or very short fibres, rather than longer individual wood fibres. Products typically contain approximately 50 percent wood, although some composites contain very little wood and others as much as 70 percent.

Wood and plastics are not the only components in WPCs. These composites also contain materials that are added in small amounts to affect processing and performance. Although formulations are highly proprietary, additives such as coupling agents, light stabilizers, pigments, lubricants, fungicides, and foaming agents are all used to some extent (Clemons, 2002).

The manufacturing of thermoplastic composites is often a two-step process. Compounding and pelletizing followed by either extrusion or injection moulding (IM). In the plastic laboratory at UQAT (University of Quebec at Abitibi-Temiscamingue) a Cincinnati Milacron extruder (55-mm counter-rotating conical twin-screw extruder having L/D ratio of 22:1) is used to compound the dry CTMP (chemi-thermo-mechanical pulp) fibres at a proportion of 40wt% and HDPE (high density polyethylene) at 60wt%. The obtained compound is then air cooled and ground with a Nelmor rotary knife grinder equipped with a screen with a 9.6 mm diameter opening to form WPC pellets. In the second stage of the process, composites are formed using either extrusion or IM. A Cincinnati

Milacron 35mm conical counter-rotating twin-screw extruder is used to form extruded samples. The length-to-front diameter ratio of the screws is 23:1. A Sumitomo 55-US ton SE-DU Series injection moulding machine is used to form injection-moulded samples (Migneault, Koubaa, Erchiqui, Chaala, Englund, & Wolcott, 2009).

The wide variety of WPCs makes it difficult to discuss the performance of these composites. Performance depends on the inherent properties of the constituent materials, interactions between these materials, processing, product design, and service environment. Adding wood to unfilled plastic can significantly increase its stiffness but can often make it more brittle. Most commercial WPC products are considerably less stiff than solid woods. Adding fibres rather than flour increases mechanical properties such as strength, elongation, and unnotched Izod impact energy (Clemons, 2002). Since WPCs absorb less moisture, and do so more slowly than solid wood, they have better fungal resistance and dimensional stability when exposed to moisture.

The increased use of WPCs in the past decade has made it essential for researchers to perform computer aided polymer analysis on them. The recent progress demonstrates the need for an accurate description of the material behaviour under the combined effects of applied stress and temperature (Erchiqui, Derdouri, Gakwaya, Godard, & Garcia-Rejon, 2001).

From the experimental point of view, there are several approaches to determine the mechanical properties of rubbers and thermoplastics. In general, for these tests the

measured variables are the displacement, strain, force and time. Treolar (Treolar, 1944) performed one-dimensional tests. The test consists of a simple extension, simple shear, and uniaxial compression.

There are three different types of two-dimensional tests:

- The equibiaxial extension on a rectangular membrane (Meissner, Raible, & Stephenson, 1981): a test to stretch a thermoplastic membrane in two directions, the XY plane of the membrane, leaving the third direction free.
- Blow a biaxial axisymmetric membrane (Treolar, 1944) (Rivlin & Saunders, 1951) (Joye, Poehlein, & Denson, 1973) (Verron, Marckmann, & Peseux, 2001) (Derdouri, Erchiqui, Bendada, Verron, & Peseux, 2000): a test to blow an initially flat circular membrane with the airflow.
- Extension and simultaneous blowing of a hollow axisymmetric cylinder (Alexander, 1971) (Benjeddou, Jankovich, & Hadhri, 1993): a test to use the stretch forces for extension, while at the same time blowing the cylinder using the airflow.

Following these tests, the problem of parameter identification for mechanical and rheological constitutive equations is addressed. These equations govern the structural behaviour of the membrane. This problem is tackled by conventional methods of optimization (Levenberg, 1944) (Marquard, 1963) combined with numerical methods (Erchiqui & Derdouri, 2005) and the experimental results. However, in the most recent

studies, the Artificial Neural Networks approach has been applied in order to identify the material constants (Erchiqui, Ozdemir, Souli, Ezzaidi, & Dituba-Ngoma, 2011).

The principle of the identification program is based on the optimization of the estimated error between the values calculated theoretically and those obtained experimentally by means of the least squares method. In the area of structural behaviour, several studies are devoted to quasistatic problems (Verron, Pesseux, Derdouri, & Connolly, 1997) (Erchiqui, Derdouri, & Verron, 2001). For example, some studies focus on the case of blowing membranes, initially flat and circular (Verron, Pesseux, Derdouri, & Connolly, 1997). Others, such as the work of Rivlin (Rivlin & Saunders, 1951), Ogden (Ogden, 1972), and Erchiqui (Erchiqui, Derdouri, & Verron, 2001), are concerned with the case of hyperelastic materials. The remainder of the studies focus on viscoelastic materials, like those of Lodge (Lodge, 1964) and Christensen (Christensen, 1980). Identification of the mechanical parameters, according to these authors, is done in two stages. The first stage is to solve, in quasistatic regime, a system of nonlinear differential equations of the first order describing the equilibrium of the membrane. The results of this system provide the pressure values corresponding to deformation values. The second step is to optimize the error between the calculated and measured pressure values by use of the least squares method. Erchiqui has adapted this approach to determine the mechanical parameters of thermoplastics like ABS (Acrylonitrile Butadiene Styrene) and HIPS (High Impact Polystyrene) (Erchiqui & Derdouri, 2005). In addition to conventional techniques, in recent decades there has been a growing interest in the use of algorithms and stochastic techniques

to solve problems of identification and physical simulations. One example of such a technique is the Artificial Neural Networks (Haykin, 1998) (MacKay, 1992). Erchiqui used this method for characterization of softened polymers (Erchiqui & Kandil, 2006). In this study, the Artificial Neural Networks approach is used in order to find the material constants.

2.3 Wind turbines

2.3.1 Wind energy

Renewable energy resources, of which wind energy is prominent, are part of the solution to the global energy problem. Over the past few decades, different types of materials such as wood, aluminium and composites have been used in manufacturing wind turbine blades. However, wood-plastic composites have not been developed to an industrial technical level for manufacturing wind turbine blades thus far. This PhD project focuses on the material characterization for wood-plastic composites and their potential application in the construction of rotorblades in cold climate regions, particularly in severe weather conditions characterized by temperatures below $-50°C$ and wind speeds sometimes exceeding 25 m/s.

In a typical wind turbine, the rotor and its three rotorblades constitute a rather flimsy structure, consisting of cantilever-mounted blades on a central hub. The basic design aspects for a rotorblade are the selection of material and shape. The material should be stiff,

strong, and light. The shape should be aerodynamic, similar to that of an airplane wing (Brøndsted, Lilholt, & Lystruo, 2005).

The rotor and rotorblades are exposed to external loads. These originate from the wind and from gravity. The operational parameters and conditions lead to the following requirements focused on stiffness, density, and long-time fatigue (Brøndsted, Lilholt, & Lystruo, 2005):

- High material stiffness is needed to maintain optimal aerodynamic performance
- Low density is needed to reduce gravity forces
- Long-fatigue life is needed to reduce material degradation

Over time, different types of composite materials have been developed and used in manufacturing rotorblades. Carbon and glass fibre composites have been extensively used over the past few decades.

The optimal design of the rotorblades today is a complex and multifaceted task that requires optimization of material properties, performance, and economy. Given the recent focus on environmental and ecological issues, including the increasing concern over limited resources, the use of wood-plastic composites is especially relevant today. Particularly, their application in resource demanding construction projects such as that of large rotorblades.

In 2010, 39.4 GW of new wind turbine capacity were installed bringing the world wide total installed wind capacity to almost 200 GW. This was a cumulative increase in installation of 25%. In terms of annual installations, there was a modest increase of just 3%. Annual installed capacity has grown by an annual average of 27.4% over the past five years. The total value of new generation equipment installed in 2010 is estimated to be about €40 million. China moved to the first place (44.7 GW), followed by the United States (40.2 GW), Germany (27.2 GW), Spain (20.7 GW) and India (13.1 GW). These figures were reported in the world market update on the status of the International Wind Power Industry 2010 (Figure 2-1) from the consulting company BTM (BTM Consult ApS, 2010).

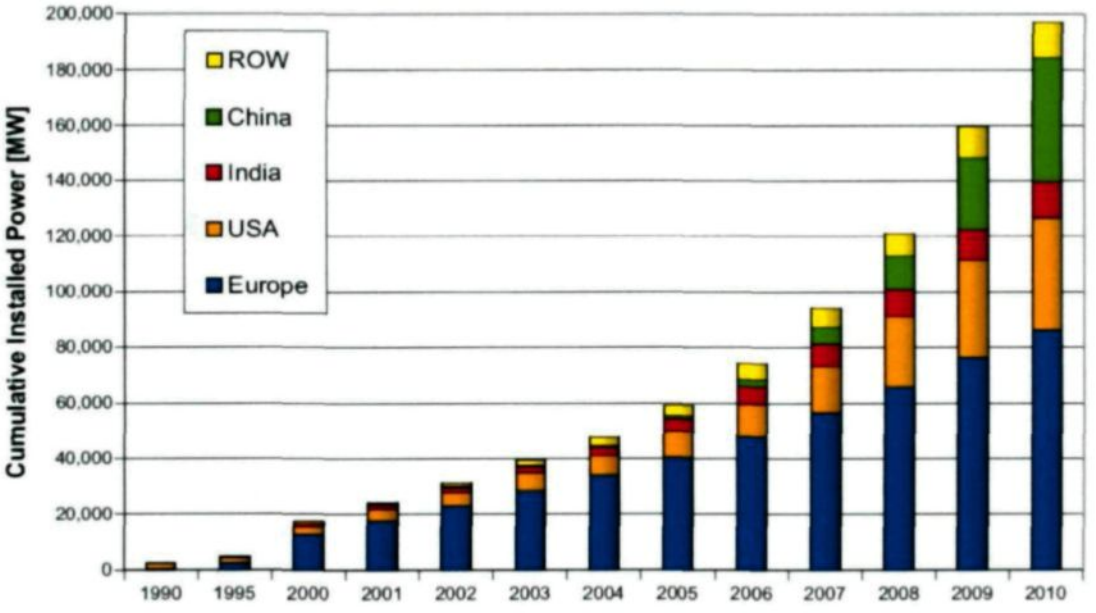

Figure 2-1 - International Wind Power Industry (BTM Consult ApS, 2010)

For wind energy a convertor is needed to turn the kinetic energy into an operational form of energy, such as electricity. The convertor is based on a rotor driven by the wind, thereby extracting the power of (w) (Brøndsted, Lilholt, & Lystruo, 2005):

$$P = \propto \rho A v^3 \qquad (2\text{-}1)$$

where $\propto$ is an aerodynamic efficiency constant, ρ $\left(\frac{kg}{m^3}\right)$ the density of air, A (m^2) the area of rotor-plane, and v $(\mathrm{m/s})$ the wind velocity (Brøndsted, Lilholt, & Lystruo, 2005). The rotor needs some form of aerodynamic device, such as a wing or rotorblade with an aerodynamic shape, to be able to rotate. The rotor is typically placed on a tower and this convertor is usually called a wind turbine (in the past, a wind mill).

The ratio between the speed of the blade tips and the speed of the wind is called the tip-speed ratio. High efficiency 3-blade-turbines have a tip-speed ratio of 6 to 7. Modern wind turbines are designed to spin at varying speeds. Use of aluminium and composite materials in their blades has contributed to low rotational inertia, which means that newer wind turbines can accelerate quickly if the winds pick up, keeping the tip-speed ratio nearly constant (Hau, 2005). In contrast, older style wind turbines were designed with heavier steel blades, which had higher inertia, and rotated at speeds governed by the AC frequency of the power lines. The high inertia buffered the changes in rotation speed and thus made power output more stable (Hau, 2005).

2.3.2 Rotorblades

Rotorblades probably present the most challenging materials, design, and engineering problems. Construction of solid airfoil designs requires inflexible materials such as metals or composites (Hau, 2005). Wood and canvas sails were used on early windmills due to their cost effectiveness, availability, and ease of manufacture and smaller blades can be made from light metals such as aluminium. However, these materials require frequent maintenance.

New wind turbine designs push power generation from the single megawatt range to upwards of 10 megawatts using increasingly larger blades. A larger area effectively increases the tip-speed ratio of a turbine at a given wind speed. Computer aided engineering software such as HyperSizer (originally developed for spacecraft design) can be used to improve blade designs (Collier & Ashwill, 2011) (Collier C. S., 2010).

The shape of a rotorblade in cross section is shown in Figure 2-2. The aerodynamic contours are formed by the (outer) relatively thin shells. They are supported structurally by a longitudinal beam or by webs, which carry a substantial part of the load on the blade. In the longitudinal direction, the rotorblades are tapered and twisted. The tapering is required in order to economize the weight of the material as the load of the cantilever structure increases form tip to root.

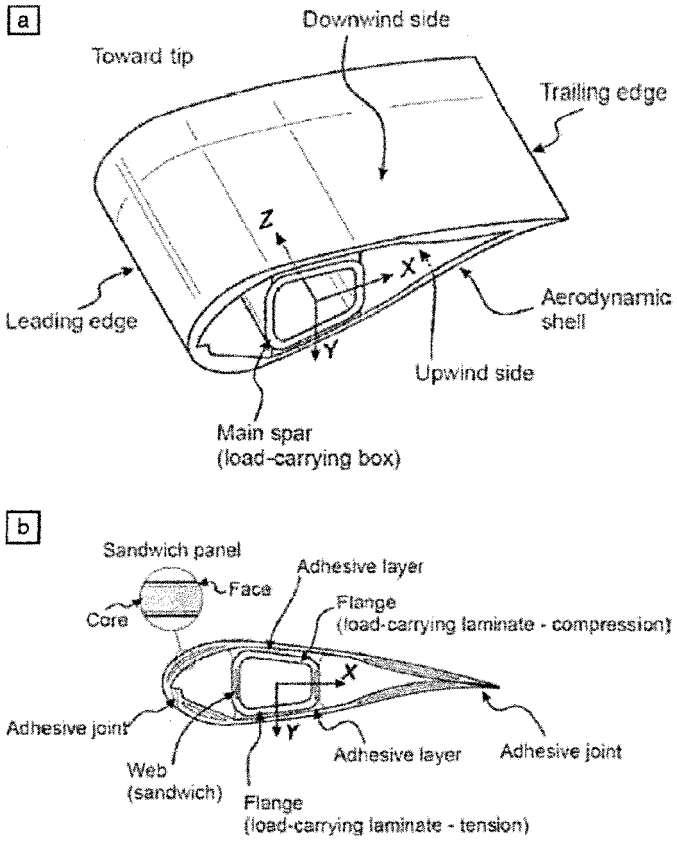

Figure 2-2 - Section of blade: (a) perspective view (b) cross-sectional view (Hogg, 2010)

2.3.3 Loads on rotorblades

The rotor and the rotorblades are exposed to external loads. These originate from the wind and from gravity. As the blades are exposed to the wind, the lifting forces on the aerodynamic profile of the blade cause the flap-wise bending on rotorblades. The loads are both static, causing a permanent bending on blades, and dynamic, causing a fatigue flap-wise bending. In addition, these static and fatigue loads spectra vary during rotation, as

seen by a given blade, when the blade points upwards and downwards. This is caused by the natural wind shear, which is the increase in average wind speed with increasing height over the terrain (Brøndsted, Lilholt, & Lystruo, 2005).

Normally, the maximum wind speed for operation of a wind turbine is about 25 m/s. Beyond this speed the rotor is brought to a standstill by turning the rotorblades out of the wind. This position causes the blade to bend due to the steady load on its surface. The natural variation in wind speed will cause a dynamic flap-wise fatigue load spectra.

The blades are also exposed to gravity, the effect of which is most when they are in the horizontal position. These loads cause bending in an edge-wise mode, and a given blade bends one way on the right-hand side and the opposite way on the left-hand side of the rotor plane. This explains why the edge-wise bending also causes fatigue of the blade material and structure during rotation.

Due to the limits of the linear blade velocity, the rotational speed is relatively low, typically between 10 and 20 rpm. Therefore, the centrifugal forces during the rotation of rotor and the longitudinal tensile loads in the blades are relatively low. The design lifetime of modern wind turbines is normally thought to be 20 years, and the corresponding number of rotations is of the order 10^8 to 10^9 (Brøndsted, Lilholt, & Lystruo, 2005).

2.3.4 Material requirements

Based on the operational parameters and conditions, the materials for the wind turbine blades must meet the requirements such as high stiffness, low density and long-fatigue life.

The material properties requirements can be used to perform a material selection, initially looking at all materials. In a simplified form, the diagram of stiffness versus density in Figure 2-3 shows the material selection procedure. The mechanical design of a rotorblade corresponds nominally to a beam, and the merit index for this case is:

$$M_b = E^{0.5}/\rho \qquad (2\text{-}2)$$

where E is the material stiffness and ρ is the material density. Lines of constant M_b are superimposed on the diagram, and materials that fulfil the criterion are on and to the upper-left of the line (Brøndsted, Lilholt, & Lystruo, 2005).

The two lines shown in Figure 2-3 are arbitrary and represent the materials that are equally acceptable in terms of stiffness and density for a cantilever beam. The lower line has a merit index $M_b = 0.003$ with units of E in GPa and ρ in kg/m^3. If the merit index is doubled the upper line is valid.

The second criterion is stiffness on an absolute scale. A stiff material results in less deflection for a cantilever beam. In Figure 2-3 the horizontal line represents that stiffness criterion. Deflection considerations depend on the rotorblade geometry and dimensions, as

well as the overall design of tower and rotor. The extreme condition regarding the design is when the rotorblade passes the tower and is in its vertical position. A sensible deflection requires a material stiffness of 10-20 GPa. The horizontal line in Figure 2-3 shows the stiffness of 15 GPa. Materials on and above this line meet the minimum requirements regarding the stiffness.

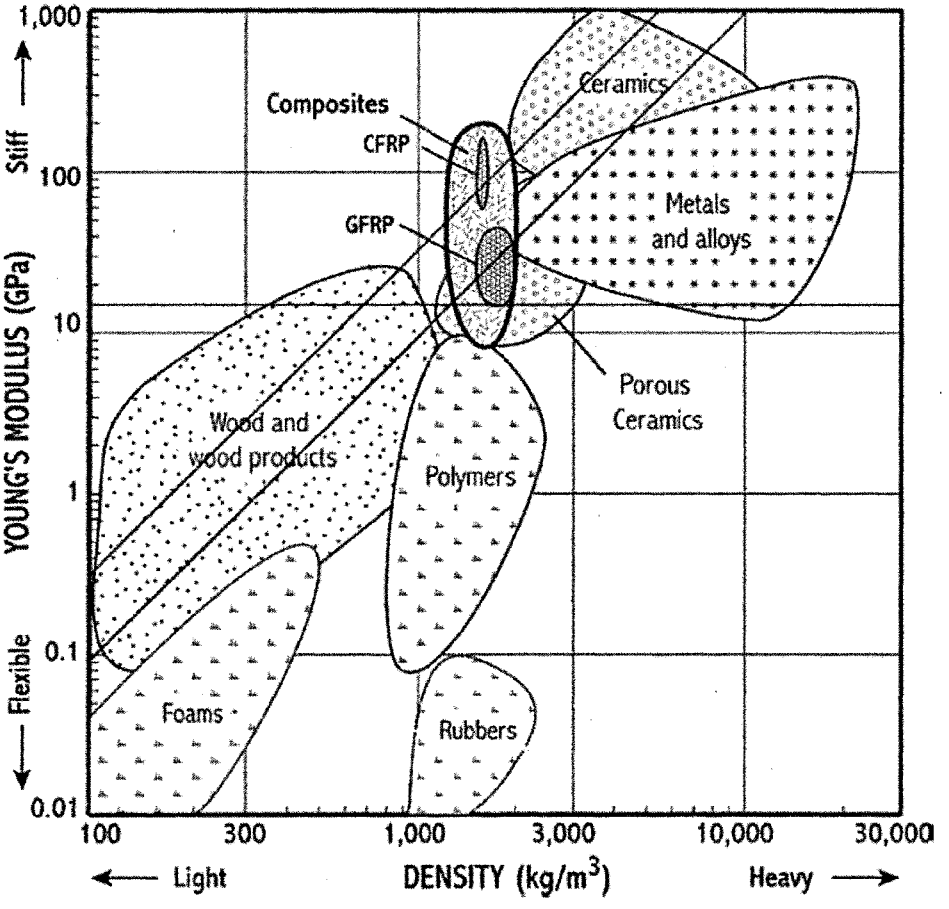

Figure 2-3 - Diagram showing stiffness versus density for all materials. The merit index for a beam $M_b = E^{0.5}/\rho$ is represented by sloping lines with M_b equal to 0.003 (lower line) and 0.006 (upper line). The criterion for absolute stiffness $E = 15\ GPa$ is indicated by the horizontal line (Lovatt & Shercliff, 2002)

2.4 Materials for rotorblades

The combined materials performance criteria identify wood and composites as candidates for rotorblades. Woods are particularly interesting because of their low density. However, their low stiffness makes it more difficult to control the maximum deflection on large rotorblades. Furthermore, wood is a natural material and thus environmentally friendly, but at the same time it is difficult to obtain wood in reproducible way with high quality.

Partly for these reasons, composites have been the most extensively used materials for rotorblades until now.

2.4.1 Fibres

Fibres play a significant role in the mechanical properties of composite materials. The strong and stiff fibres are themselves not useable for structural purposes. However, their good properties can be exploited only as an important component of composites.

Until now the glass fibres are the most widely used fibres. In recent years, carbon fibres have become of increasing interest because of the requirements presented by the very large rotorblades and also the decreasing price of carbon fibres. It should be noted that wood-plastic composites have not been used for manufacturing rotorblades thus far, even though they have similar, or sometimes even better, performance than other composites. Key data for some fibres are collected in Table 2-1.

Table 2-1 - Composite materials based on the fibres listed and a polymer matrix with properties $E_m = 3GPa$, $\sigma_m = 100\ MPa$, and $\rho_m = 1.2g/cm^3$ (Brondsted, Lilholt, & Lystruo, 2005)

	Fibres			Composites					
Type	Stiffness E_f GPa	Tensile Strength σ_f MPa	Density ρ_f g/cm^3	Volume fraction V_f	Orient. θ	Stiffness E_c GPa	Tensile Strength σ_c MPa	Density ρ_c g/cm^3	Merit $M_b = E^{0.5}/\rho$
Glass E	72	3500	2.54	0.5 0.3	0° Random	38 9.3	1800 420	1.87 1.60	3.3 1.9
Carbon	350	4000	1.77	0.5 0.3	0° Random	176 37	2050 470	1.49 1.37	8.9 4.4
Aramid	120	3600	1.45	0.5 0.3	0° Random	61 14.1	1850 430	1.33 1.27	5.9 2.9
Polyethylene	117	2600	0.97	0.5 0.3	0° Random	60 13.8	1350 330	1.09 1.13	7.1 3.3
Wood	80	1000	1.50	0.5 0.3	0° Random	41 10.1	550 170	1.35 1.29	4.7 2.5

2.4.2 Glass and carbon fibre composites

Glass is generally composed of SiO_2, Al_2O_3, and smaller amounts of other oxides. The atoms of Si and O form a lattice with no crystallographic order, and glass fibres are therefore amorphous with isotropic properties. Glass fibres are produced in several chemical compositions for specific purposes. The glass fibre called type E (electrical) is the most widely used for composites. Glass fibres have diameters normally in range of 10 to 20 μm and are produced from molten glass by pulling fibres from spinnerets into bundles of hundreds of thousands of individual fibres. Their surfaces are normally coated immediately with a polymer sizing, typically a silane compound, to protect the fibres against cracks and adhered water (Watt & Perov, 1985).

Glass fibres for composites have a good combination of properties such as moderate stiffness, high strength, and moderate density.

Carbon fibres are composed of nearly pure carbon, which forms a crystallographic lattice with hexagonal shape called graphite. The atoms are held together by strong covalent forces inside the hexagonal plane, where the atom spacing is 1.4 Å, the bonds between the hexagonal planes are weak, and the spacing is large, 3.4 Å. This crystallography implies a high degree of anisotropy, both in mechanical and thermal properties. In order to achieve the useful properties of the fibres, it is essential to arrange the hexagonal planes in such a way that the planes are oriented parallel to the fibre axis (Watt & Perov, 1985).

The carbon fibres are produced by two different methods. The first and most widely used method starts with polyacrylonitrile (PAN) fibres. These textile fibres are oxidized, stretched, and finally heat-treated with temperatures of 1500 to 2500°C. These process steps align and couple the original C-C backbone of PAN into the graphite hexagon-planes required for the fibres. The second method starts from natural tar, which contains the graphite units in a random mixture. Various processing steps lead to the production of fibres through spinnerets, which ensure alignment of the graphite planes and thus the required properties of the fibres. The first method achieves the necessary alignments of the graphite planes through coupling of C-C backbones, whereas the second method aligns pre-existing graphite planes. Both methods include rather expensive raw materials and numerous and expensive processing steps.

The composite materials with the above mentioned fibres have matrices of polymers, typically thermosets or thermoplastics. Both are rather soft and flexible with low stiffness of less than 4 GPa, and their main purpose is to bind the fibres together. The

toughness and especially failure strain is moderate for thermosets, 5-8% and large for thermoplastics, 50-100%. The matrix in a composite material induces the toughness via energy absorbing mechanisms related to the interface. The early composite materials for rotorblades were glass fibres combined with polyester. The manufacturing process was taken from the boat industry.

The thermoplastic composites for rotorblades have been under development in the past 15 years. The interest is centred on the potential recycling of thermoplastic polymers.

Many combinations and mixing ratios are possible to make composite materials. The fibres, the matrix and the interface established between these two components, generally govern the composite properties. The important parameters are fibre volume fraction and the spatial orientation of the fibres inside the matrix.

The stiffness of a composite material is calculated by the equation below (Jones, 1975):

$$E_c = \eta . V_f . E_f + V_m . E_m \qquad (2\text{-}3)$$

where E is the stiffness (elastic modulus), V is the volume fraction, ŋ is an orientation factor for the fibres. Index f indicates fibres and index m indicates matrix material. For a perfect composite with no porosity, $V_f + V_m = 1$. The orientation factor is equal to 1 for aligned parallel fibres loaded along the fibre direction. For a randomly oriented fibre in a composite material the orientation factor is 1/3.

The values listed in Table 2-1, illustrate the mechanical properties of the composites based on the various fibres mentioned above. The fibres are normally a dominant contributor to the composite properties.

The last column in Table 2-1 shows the elastic merit index for a cantilever beam that is used to design the rotorblades structure. As mentioned above the minimum acceptable value for stiffness is 15 GPa. It is clear from the composite stiffness that all aligned fibre composites have a relatively higher stiffness as compared to randomly oriented fibre composites.

2.5 Manufacturing rotorblades

Few different technologies have been used so far for manufacturing rotorblades. In the early days, small glass fibre reinforced blades were manufactured using the traditional wet hand-lay-up technique in open moulds, which has been used for decades for making boats.

When government-supported development programs for larger wind turbines started in the mid-1970s, the filament winding technique was investigated by several nations. Filament winding is a rational way of placing a huge amount of roving in a controlled manner around a rotating mandrel (Brøndsted, Lilholt, & Lystruo, 2005).

Later, the prepreg (pre-impregnated) technology was adapted from the aerospace and aircraft industry. The prepreg technique is based on the use of a semi-raw product,

where the fibre and fabrics are pre-impregnated with resin, which is not yet cured. At room temperature the resin is like a tacky solid and the tacky prepregs can be stacked on top of each other to build the desired laminate. By increasing the temperature the resin becomes liquid/viscous and the laminate can be consolidated under pressure and cured into the final component.

Resin infusion technology has also been used as a technique for manufacturing rotorblades. The principle consists of placing dry fibres in a mould, encapsulating and sealing off the fibre package, injecting the liquid resin into the fibre package, and curing the component. The most important issue for the process is to ensure that all fibres are thoroughly wetted by the resin. In other words, there should be no areas with dry fibres in the final product.

Manufacturing blades in the 40 to 50 meter range involves proven fibreglass composite fabrication techniques. Manufacturers such as Nordex and GE Wind use an infusion process. Other manufacturers use variations on this technique, some including carbon and wood with fibreglass in an epoxy matrix. Options also include prepreg fibreglass and vacuum-assisted resin transfer moulding. Each of these options use a glass-fibre reinforced polymer composite, constructed with differing complexity. Perhaps the largest issue with more simplistic, open-mould, wet systems, are the emissions associated with the volatile organics released (Griffin & Ashwill, 2003).

Epoxy-based composites have environmental, production, and cost advantages over other resin systems. Epoxies also allow shorter cure cycles, increased durability, and improved surface finish. Carbon fibre-reinforced load-bearing spars can reduce weight and increase stiffness. Using carbon fibres in 60 meter turbine blades is estimated to reduce total blade mass by 38% and decrease cost by 14%, when compared to 100% fibreglass (Griffin & Ashwill, 2003).

2.6 Mechanical behaviour of materials

In this project the elastic and hyperelastic behaviour of wood-plastic composites is investigated. Therefore, it is necessary to provide a brief review on these two types of behaviours of materials.

2.6.1 Elastic materials

An elastic material is a type of material that generates internal forces in order to restore the shape of material to its original state when it is deformed due to an external force. There are various elastic moduli, such as Young's modulus, the shear modulus, and the bulk modulus (Popov, 1976).

The elasticity of materials is described by a stress-strain curve that shows the relation between stress and strain when the material is subjected to external loads. For most metals or crystalline materials, the curve is linear for small deformations and thus, the stress-strain relationship can adequately be described by Hooke's law. However, for larger

stresses beyond the elastic limit, the relationship is no longer linear. For even higher stresses, materials exhibit plastic behaviour that means they deform irreversibly and do not return to their original shape after the stress is removed (Popov, 1976). For rubber-like materials, such as elastomers, the gradient of the stress-strain curve increases with stress, meaning that rubbers progressively become more difficult to stretch. However, for most metals, the gradient decreases at very high stresses and that means they progressively become easier to stretch.

Hooke's law: as mentioned above, for small deformations, most elastic materials exhibit linear elasticity. This idea was first formulated by Robert Hooke in 1675. Hooke's law can be stated as a relationship between force and displacement (Popov, 1976):

$$F = -kx \tag{2-4}$$

where k is a constant, known as the rate or spring constant. The relationship between stress, σ, and strain, ϵ, can be stated as follows:

$$\sigma = E\varepsilon \tag{2-5}$$

where E is known as elastic modulus or Young's modulus.

In general the 3D form of Hooke's law is given by:

$$\varepsilon_1 = \frac{1}{E}\left(\sigma_1 - \nu(\sigma_2 + \sigma_3)\right) \tag{2-6}$$

$$\varepsilon_2 = \frac{1}{E}\left(\sigma_2 - \nu(\sigma_1 + \sigma_3)\right) \quad (2\text{-}7)$$

$$\varepsilon_3 = \frac{1}{E}\left(\sigma_3 - \nu(\sigma_1 + \sigma_2)\right) \quad (2\text{-}8)$$

The rheological parameters of materials are determined in the industry according to international standards established generally on the basis of techniques and robust methods of estimation. Concerning solid polymers and the determination of Young's modulus in tensile tests, ISO 527-1 or ASTM D638 standards rely on protocols with scientific content: the determination of the slope of conventionally defined straight lines fitted to stress-strain curves in a given range of elongations. However, Blaise described an alternative approach allowing for a more accurate measurement of the instantaneous elastic modulus of polymers in a tensile test (Blaise, Andre, Delobelle, Meshaka, & Cunat, 2012). This approach is based on the use of an appropriate reduced model to describe the behaviour of the material. The model has a thermodynamical framework allowing it to reproduce the behaviour of an HDPE polymer until large strains, covering the elastoviscoplastic and hardening regimes.

2.6.2 Hyperelastic materials

A hyperelastic or Green elastic material is a type of constitutive model for ideally elastic material for which the stress-strain relationship derives from a strain energy function. For many materials, linear elastic models do not accurately describe the observed material behaviour. The most common example of this kind of material is rubber for which

stress-strain relationship can be defined as non-linearly elastic, isotropic, incompressible and generally independent of strain rate.

Ronald Rivlin and Melvin Mooney developed the first hyperelastic models, the Neo-Hookean and Mooney-Rivlin solids (Rivlin R. S., 1948). Many other hyperelastic models have since been developed such as Ogden model and Arruda-Boyce model (Ogden, 1972).

Mooney-Rivlin model: in continuum mechanics, a Mooney-Rivlin solid is a hyperelastic material model where the strain energy density function, W, is a linear combination of two invariants of the left Cauchy-Green deformation tensor, $\boldsymbol{B}$. The model was proposed by Melvin Mooney in 1940 and expressed in terms of invariants by Ronald Rivlin in 1948 (Carroll & Hayes, 1996).

For an incompressible Mooney-Rivlin material the strain energy density function is (Carroll & Hayes, 1996):

$$W = C_1(\bar{I}_1 - 3) + C_2(\bar{I}_2 - 3) \qquad (2\text{-}9)$$

where C_1 and C_2 are empirically determined material constants, and I_1 and I_2 are the first and the second invariants of the unimodular component of the left Cauchy-Green deformation tensor:

$$\bar{I}_1 = J^{-2/3} I_1 \; ; \; I_1 = \lambda_1^2 + \lambda_2^2 + \lambda_3^2 \; ; \; J = det(\boldsymbol{F}) \qquad (2\text{-}10)$$

$$\bar{I}_2 = J^{-4/3} I_2 \; ; \; I_2 = \lambda_1^2\lambda_2^2 + \lambda_2^2\lambda_3^2 + \lambda_3^2\lambda_1^2 \tag{2-11}$$

where $\boldsymbol{F}$ is the deformation gradient. For an incompressible material, $J = 1$.

The Mooney-Rivlin model is a special case of the generalized Rivlin model that has the form:

$$W = \sum_{p,q=0}^{N} C_{p,q}(\bar{I}_1 - 3)^p(\bar{I}_2 - 3)^q + \sum_{m=1}^{M} D_m(J-1)^{2m} \tag{2-12}$$

with $C_{00} = 0$ where C_{pq} are material constants related to the distortional response and D_m are material constants related to the volumetric response. For a compressible Mooney-Rivlin material: $N = 1$, $C_{01} = C_2$, $C_{11} = 0$, $C_{10} = C_1$, $M = 1$ and thus:

$$W = C_{01}(\bar{I}_2 - 3) + C_{10}(\bar{I}_1 - 3) + D_1(J-1)^2 \tag{2-13}$$

If $C_{01} = 0$, a neo-Hookean solid is obtained that is a special case of Mooney-Rivlin solid.

For consistency with linear elasticity in the limit of small strains, it is necessary that:

$$\kappa = 2.D_1 \; ; \; \mu = 2(C_{01} + C_{10}) \tag{2-14}$$

where κ is the bulk modulus and μ is the shear modulus.

The Cauchy stress in a compressible hyperelastic material with a stress free reference configuration is given by:

$$\boldsymbol{\sigma} = \frac{2}{J}\left[\frac{1}{J^{2/3}}\left(\frac{\partial W}{\partial \bar{I}_1} + \bar{I}_1 \frac{\partial W}{\partial \bar{I}_2}\right)\boldsymbol{B} - \frac{1}{J^{4/3}}\frac{\partial W}{\partial \bar{I}_2}\boldsymbol{B}.\boldsymbol{B}\right] + \left[\frac{\partial W}{\partial J} - \frac{2}{3J}\left(\bar{I}_1 \frac{\partial W}{\partial \bar{I}_1}\right) + 2\bar{I}_2 \frac{\partial W}{\partial \bar{I}_2}\right]\mathbf{1} \quad (2\text{-}15)$$

For a compressible Mooney-Rivlin material:

$$\frac{\partial W}{\partial \bar{I}_1} = C_1 \; ; \; \frac{\partial W}{\partial \bar{I}_2} = C_2 \; ; \; \frac{\partial W}{\partial J} = 2D_1(J-1) \quad (2\text{-}16)$$

Therefore, the Cauchy stress in a compressible Mooney-Rivlin material is given by:

$$\sigma = \frac{2}{J}\left[\frac{1}{J^{2/3}}(C_1 + \bar{I}_1 C_2)\boldsymbol{B} - \frac{1}{J^{4/3}}C_2\boldsymbol{B}.\boldsymbol{B}\right] + \left[2D_1(J-1) - \frac{2}{3J}(C_1\bar{I}_1 + 2C_2\bar{I}_2)\right]\mathbf{1} \quad (2\text{-}17)$$

It can be shown that the pressure is given by:

$$p = -\frac{\partial W}{\partial J} = -2D_1(J-1) \quad (2\text{-}18)$$

The stress can then be expressed by:

$$\boldsymbol{\sigma} = \frac{1}{J}\left[-p\mathbf{1} + \frac{2}{J^{2/3}}(C_1 + \bar{I}_1 C_2)\boldsymbol{B} - \frac{2}{J^{4/3}}C_2\boldsymbol{B}.\boldsymbol{B} - \frac{2}{3}(C_1\bar{I}_1 + 2C_2\bar{I}_2)\mathbf{1}\right] \quad (2\text{-}19)$$

The above equation is often written as:

$$\boldsymbol{\sigma} = \frac{1}{J}\left[-p\mathbf{1} + 2(C_1 + \bar{I}_1 C_2)\bar{\boldsymbol{B}} - 2C_2\bar{\boldsymbol{B}}.\bar{\boldsymbol{B}} - \frac{2}{3}(C_1\bar{I}_1 + 2C_2\bar{I}_2)\mathbf{1}\right] \quad (2\text{-}20)$$

where $\bar{\boldsymbol{B}} = J^{-2/3}\boldsymbol{B}$

For an incompressible Mooney-Rivlin material with $J = 1$

$$\sigma = 2(C_1 + I_1 C_2)\boldsymbol{B} - 2C_2\boldsymbol{B}.\boldsymbol{B} - \frac{2}{3}(C_1\bar{I}_1 + 2C_2\bar{I}_2)\mathbf{1} \qquad (2\text{-}21)$$

In terms of the principal stretches, the Cauchy stress differences for an incompressible hyperelastic material are given by:

$$\sigma_{11} - \sigma_{33} = \lambda_1\frac{\partial W}{\partial \lambda_1} - \lambda_3\frac{\partial W}{\partial \lambda_3}\ ;\ \sigma_{22} - \sigma_{33} = \lambda_2\frac{\partial W}{\partial \lambda_2} - \lambda_3\frac{\partial W}{\partial \lambda_3} \qquad (2\text{-}22)$$

For an incompressible Mooney-Rivlin material:

$$W = C_1(\lambda_1^2 + \lambda_2^2 + \lambda_3^2 - 3) + C_2(\lambda_1^2\lambda_2^2 + \lambda_2^2\lambda_3^2 + \lambda_3^2\lambda_1^2 - 3)\ ;\ \lambda_1\lambda_2\lambda_3 = 1 \qquad (2\text{-}23)$$

Therefore,

$$\lambda_1\frac{\partial W}{\partial \lambda_1} = 2C_1\lambda_1^2 + 2C_2\lambda_1^2(\lambda_2^2 + \lambda_3^2)\ ;\ \lambda_2\frac{\partial W}{\partial \lambda_2} = 2C_1\lambda_2^2 + 2C_2\lambda_2^2(\lambda_1^2 + \lambda_3^2)\ ;$$

$$\lambda_3\frac{\partial W}{\partial \lambda_3} = 2C_1\lambda_3^2 + 2C_2\lambda_3^2(\lambda_1^2 + \lambda_2^2) \qquad (2\text{-}24)$$

Since $\lambda_1\lambda_2\lambda_3 = 1$, then:

$$\lambda_1\frac{\partial W}{\partial \lambda_1} = 2C_1\lambda_1^2 + 2C_2\left(\frac{1}{\lambda_2^2} + \frac{1}{\lambda_3^2}\right)\ ;\ \lambda_2\frac{\partial W}{\partial \lambda_2} = 2C_1\lambda_2^2 + 2C_2\left(\frac{1}{\lambda_1^2} + \frac{1}{\lambda_3^2}\right)\ ;$$

$$\lambda_3\frac{\partial W}{\partial \lambda_3} = 2C_1\lambda_3^2 + 2C_2\left(\frac{1}{\lambda_2^2} + \frac{1}{\lambda_1^2}\right) \qquad (2\text{-}25)$$

Then the expressions for the Cauchy stress differences become:

$$\sigma_{11} - \sigma_{33} = 2C_1(\lambda_1^2 - \lambda_3^2) - 2C_2\left(\frac{1}{\lambda_1^2} - \frac{1}{\lambda_3^2}\right) \qquad (2\text{-}26)$$

$$\sigma_{22} - \sigma_{33} = 2C_1(\lambda_2^2 - \lambda_3^2) - 2C_2\left(\frac{1}{\lambda_2^2} - \frac{1}{\lambda_3^2}\right) \quad (2\text{-}27)$$

For the case of an incompressible Mooney-Rivlin material under uniaxial elongation, $\lambda_1 = \lambda$ and $\lambda_2 = \lambda_3 = \frac{1}{\sqrt{\lambda}}$. Then the Cauchy stress differences can be calculated as:

$$\sigma_{11} - \sigma_{33} = 2C_1\left(\lambda^2 - \frac{1}{\lambda}\right) - 2C_2\left(\frac{1}{\lambda^2} - \lambda\right) \quad (2\text{-}28)$$

$$\sigma_{22} - \sigma_{33} = 0 \quad (2\text{-}29)$$

In the case of simple tension, $\sigma_{22} = \sigma_{33} = 0$. Therefore:

$$\sigma_{11} = \left(2C_1 + \frac{2C_2}{\lambda}\right)\left(\lambda^2 - \frac{1}{\lambda}\right) \quad (2\text{-}30)$$

In the case of equibiaxial tension, the principal stretches are $\lambda_1 = \lambda_2 = \lambda$. If the material is incompressible then $\lambda_3 = {}^{1}/_{\lambda^2}$. The Cauchy stress differences may therefore be expressed as:

$$\sigma_{11} - \sigma_{33} = \sigma_{22} - \sigma_{33} = 2C_1\left(\lambda^2 - \frac{1}{\lambda^4}\right) - 2C_2\left(\frac{1}{\lambda^2} - \lambda^4\right) \quad (2\text{-}31)$$

Neo-Hookean model: the neo-Hookean model is a hyperelastic material model, similar to Hook's law that can be used for predicting nonlinear stress-strain behaviour of materials. The model was proposed by Ronal Rivlin in 1948. In contrast to linear elastic materials, the stress-strain curve of a neo-Hookean material is not linear. Instead, the

relationship between applied stress and strain is initially linear, but at a certain point the stress-strain curve will plateau. The neo-Hookean model does not account for the dissipative release of energy as heat while straining the material and perfect elasticity is assumed at all stages of deformation (Carroll & Hayes, 1996).

The neo-Hookean model is based on the statistical thermodynamic of cross-linked polymer chains. The strain energy density function for an incompressible neo-Hookean material is:

$$W = C_1(I_1 - 3) \tag{2-32}$$

where C_1 is a material constant, and I_1 is the first invariant of the left Cauchy-Green deformation tensor:

$$I_1 = \lambda_1^2 + \lambda_2^2 + \lambda_3^2 \tag{2-33}$$

where λ_i are the principal stretches. For three dimensional problems of the compressible neo-Hookean material the strain energy density function is given by:

$$W = C_1(\bar{I}_1 - 3) + D_1(J-1)^2 \; ; J = \det(\boldsymbol{F}) = \lambda_1\lambda_2\lambda_3 \tag{2-34}$$

where D_1 is a material constant, $\bar{I}_1 = J^{-2/3}I_1$ is the invariant of the deviatoric part of the left Cauchy-Green deformation tensor, and $\boldsymbol{F}$ is the deformation gradient. It can be shown that in 2D, the strain energy density function becomes:

$$W = C_1(\bar{I}_1 - 2) + D_1(J-1)^2 \tag{2-35}$$

where $\bar{I}_1 = I_1/J$.

Several alternative formulations exist for compressible neo-Hookean materials, for example:

$$W = C_1(\bar{I}_1 - 3 - 2\ln J) + D_1(J-1)^2 \tag{2-36}$$

For consistency with linear elasticity,

$$C_1 = \frac{\mu}{2}\ ;\ D_1 = \frac{\kappa}{2} \tag{2-37}$$

where μ is the shear modulus and κ is the bulk modulus.

For a compressible Rivlin neo-Hookean material the Cauchy stress is given by:

$$J\boldsymbol{\sigma} = -p\mathbf{1} + 2C_1 dev(\bar{\boldsymbol{B}}) = -p\mathbf{1} + \frac{2C_1}{J^{\frac{2}{3}}} dev(\boldsymbol{B}) \tag{2-38}$$

where $\boldsymbol{B}$ is the left Cauchy-Green deformation tensor, and

$$p := -2D_1 J(J-1)\ ;\ dev(\bar{\boldsymbol{B}}) = \bar{\boldsymbol{B}} - \frac{1}{3} I_1 \mathbf{1}\ ;\ \bar{\boldsymbol{B}} = J^{-2/3}\boldsymbol{B} \tag{2-39}$$

For infinitesimal strains ($\boldsymbol{\varepsilon}$):

$$J \approx 1 + tr(\boldsymbol{\varepsilon})\ ;\ \boldsymbol{B} \approx \mathbf{1} + 2\boldsymbol{\varepsilon} \tag{2-40}$$

and the Cauchy stress can be expressed as:

$$\boldsymbol{\sigma} \approx 4C_1\left(\boldsymbol{\varepsilon} - \frac{1}{3}tr(\boldsymbol{\varepsilon})\mathbf{1}\right) + 2D_1 tr(\boldsymbol{\varepsilon})\mathbf{1} \tag{2-41}$$

Comparison with Hooke's law shows that $\mu = 2C_1$ and $\kappa = 2D_1$.

For an incompressible neo-Hookean material with $J = 1$:

$$\boldsymbol{\sigma} = -p\mathbf{1} + 2C_1\boldsymbol{B} \tag{2-42}$$

For a compressible neo-Hookean hyperelastic material, the principal components of the Cauchy stress are given by:

$$\sigma_i = 2C_1 J^{-5/3}\left(\lambda_i^2 - \frac{I_1}{3}\right) + 2D_1(J-1)\,; i = 1,2,3 \tag{2-43}$$

Therefore, the differences between the principal stresses are:

$$\sigma_{11} - \sigma_{33} = \frac{2C_1}{J^{\frac{5}{3}}}(\lambda_1^2 - \lambda_3^2)\,;\ \sigma_{22} - \sigma_{33} = \frac{2C_1}{J^{\frac{5}{3}}}(\lambda_2^2 - \lambda_3^2) \tag{2-44}$$

In terms of principal stretches, the Cauchy stress differences for an incompressible hyperelastic material are given by`:

$$\sigma_{11} - \sigma_{33} = \lambda_1\frac{\partial W}{\partial \lambda_1} - \lambda_3\frac{\partial W}{\partial \lambda_3}\ ;\ \sigma_{22} - \sigma_{33} = \lambda_2\frac{\partial W}{\partial \lambda_2} - \lambda_3\frac{\partial W}{\partial \lambda_3} \tag{2-45}$$

For an incompressible neo-Hookean material:

$$W = C_1(\lambda_1^2 + \lambda_2^2 + \lambda_3^2)\,;\ \lambda_1\lambda_2\lambda_3 = 1 \tag{2-46}$$

Therefore,

$$\frac{\partial W}{\partial \lambda_1} = 2C_1\lambda_1 \; ; \; \frac{\partial W}{\partial \lambda_2} = 2C_1\lambda_2 \; ; \; \frac{\partial W}{\partial \lambda_3} = 2C_1\lambda_3 \tag{2-47}$$

which gives:

$$\sigma_{11} - \sigma_{33} = 2(\lambda_1^2 - \lambda_3^2)C_1 \; ; \; \sigma_{22} - \sigma_{33} = 2(\lambda_2^2 - \lambda_3^2)C_1 \tag{2-48}$$

For a compressible material undergoing uniaxial extension, the principal stretches are:

$$\lambda_1 = \lambda \; ; \; \lambda_2 = \lambda_3 = \sqrt{\frac{J}{\lambda}} \; ; \; I_1 = \lambda^2 + \frac{2J}{\lambda} \tag{2-49}$$

Therefore, the true stresses for a compressible neo-Hookean material are given by:

$$\sigma_{11} = \frac{4C_1}{3J^{\frac{5}{3}}}\left(\lambda^2 - \frac{J}{\lambda}\right) + 2D_1(J-1) \tag{2-50}$$

$$\sigma_{22} = \sigma_{33} = \frac{2C_1}{3J^{\frac{5}{3}}}\left(\frac{J}{\lambda} - \lambda^2\right) + 2D_1(J-1) \tag{2-51}$$

The stress differences are given by:

$$\sigma_{11} - \sigma_{33} = \frac{2C_1}{J^{5/3}}\left(\lambda^2 - \frac{J}{\lambda}\right) \; ; \; \sigma_{22} - \sigma_{33} = 0 \tag{2-52}$$

If the material is unconstrained, then: $\sigma_{22} = \sigma_{33} = 0$ and:

$$\sigma_{11} = \frac{2C_1}{J^{5/3}}\left(\lambda^2 - \frac{J}{\lambda}\right) \tag{2-53}$$

For incompressible neo-Hookean material under uniaxial extension, $\lambda_1 = \lambda$ and $\lambda_2 = \lambda_3 = 1/\sqrt{\lambda}$. Therefore,

$$\sigma_{11} - \sigma_{33} = 2C_1\left(\lambda^2 - \frac{1}{\lambda}\right) \; ; \; \sigma_{22} - \sigma_{33} = 0 \tag{2-54}$$

Assuming no tractions on the sides, $\sigma_{22} = \sigma_{33} = 0$, thus:

$$\sigma_{11} = 2C_1\left(\lambda^2 - \frac{1}{\lambda}\right) = 2C_1\left(\frac{3\varepsilon_{11} + 3\varepsilon_{11}^2 + \varepsilon_{11}^3}{1+\varepsilon_{11}}\right) \tag{2-55}$$

where $\varepsilon_{11} = \lambda - 1$ is the engineering strain.

In the case of compressible neo-Hookean material under equibiaxial extension:

$$\lambda_1 = \lambda_2 = \lambda \; ; \; \lambda_3 = \frac{J}{\lambda^2} \; ; \; I_1 = 2\lambda^2 + \frac{J^2}{\lambda^4} \tag{2-56}$$

Therefore,

$$\sigma_{11} = 2C_1\left[\frac{\lambda^2}{J^{5/3}} - \frac{1}{3J}\left(2\lambda^2 + \frac{J^2}{\lambda^4}\right)\right] + 2D_1(J-1) = \sigma_{22} \tag{2-57}$$

$$\sigma_{33} = 2C_1\left[\frac{J^{1/3}}{\lambda^4} - \frac{1}{3J}\left(2\lambda^2 + \frac{J^2}{\lambda^4}\right)\right] + 2D_1(J-1) \tag{2-58}$$

The stress differences are:

$$\sigma_{11} - \sigma_{22} = 0\,;\ \sigma_{11} - \sigma_{33} = \frac{2C_1}{J^{\frac{5}{3}}}\left(\lambda^2 - \frac{J^2}{\lambda^4}\right) \tag{2-59}$$

If the material is in a state of plane stress then $\sigma_{33} = 0$ and:

$$\sigma_{11} = \sigma_{22} = \frac{2C_1}{J^{\frac{5}{3}}}\left(\lambda^2 - \frac{J^2}{\lambda^4}\right) \tag{2-60}$$

For an incompressible material $J = 1$ and the differences between the principal Cauchy stresses take the form:

$$\sigma_{11} - \sigma_{22} = 0\,;\ \sigma_{11} - \sigma_{33} = 2C_1\left(\lambda^2 - \frac{1}{\lambda^4}\right) \tag{2-61}$$

Under plane stress conditions:

$$\sigma_{11} = 2C_1\left(\lambda^2 - \frac{1}{\lambda^4}\right) \tag{2-62}$$

2.7 Artificial Neural Networks

An Artificial Neural Network (ANN) is an information processing paradigm that is inspired by the way biological nervous systems, such as the brain, process information. The key element of this paradigm is the novel structure of the information processing system. It is composed of a large number of highly interconnected processing elements (neurones) working in unison to solve specific problems. ANNs, like people, learn by examples. An ANN is configured for a specific application, such as pattern recognition or data classification, through a learning process (Stergiou & Siganos, 1996).

Neural network simulations appear to be a recent development. However, this field was established before the advent of computers, and has survived at least one major setback and several eras.

Many important advances have been boosted by the use of inexpensive computer emulations. The first artificial neurons were produced in 1943 by the neurophysiologist Warren McCulloch and the logician Walter Pits. However, the technology available at that time did not allow them to do too much (Stergiou & Siganos, 1996).

Neural networks, with their remarkable ability to derive meaning from complicated or imprecise data, can be used to extract patterns and detect trends that are too complex to be noticed by either humans or other computer techniques. A trained neural network can be thought of as an expert in the category of information it has been given to analyse. This expert can then be used to provide projections given new situations of interest and answer "what if" questions. Other advantages include:

- Adaptive learning: an ability to learn how to do tasks based on the data given for training or initial experience.
- Self-Organisation: An ANN can create its own organisation or representation of the information it receives during learning time.
- Real Time Operation: ANN computations may be carried out in parallel, and special hardware devices are being designed and manufactured that take advantage of this capability.

- Fault Tolerance via Redundant Information Coding: Partial destruction of a network leads to the corresponding degradation of performance. However, some network capabilities may be retained even with major network damage.

The computing world has a lot to gain from neural networks. Their ability to learn makes them very flexible and powerful. Furthermore, there is no need to devise an algorithm in order to perform a specific task, for example there is no need to understand the internal mechanism of that task. They are also very suited for real time systems because of their fast processing due to their parallel architecture.

Neural networks also contribute to other areas of research such as neurology and psychology. They are widely used to model parts of living organisms and to investigate the internal mechanisms of the brain.

2.8 Conclusion

In this chapter a thorough review of the literature was presented. As noted, wood-plastic composites have not been used in the rotorblades industry despite several advantages, such as low-cost, the non-toxic nature, and recyclability of the wood.

Understanding the basic concepts relevant to the work and a detailed knowledge of the literature helps to study the behaviour of WPCs and investigate their potential application in the rotorblades industry.

CHAPTER 3

EXPERIMENTAL MODELLING

3.1 Introduction

In this chapter the experimental modelling of the project is presented in order to study the behaviour of wood-plastic composites at cold temperatures.

First, the material preparation with respect to WPC specimens is explained. Following the material preparation, the problem of selection of an appropriate experimental approach is challenged.

After selecting the suitable experimental approach, the details of the experimental setup with a brief description of all the parts are provided. In order to better understand the bubble inflation phenomenon and study the boundary conditions, the mathematical model of the deformation is presented.

Finally, the conditions under which the experiments are carried out and the results of the tests using different membranes at different temperatures are presented.

3.2 Material preparation

The wood-plastic composite specimens used in this project are manufactured at the plastic laboratory of UQAT. The polymer matrix of the composite is HDPE and its melting point is 135°C. The coupling agent is Fusabond 226DE Dupont. It is a maleic anhydride grafted polyethylene and its melting point is 120°C and has a melt index of 1.5 g/10 min (190°C, 2.16 kg). The amount of coupling agent used is 3% of the total weight of the composite. This amount was found to be optimal in order to improve the homogeneity of the matrix, ensuring better distribution of the fibres in the polymer matrix. In the composite, wood is in the form of sawdust that was previously dried. The sawdust was dried at a temperature of 105°C for 24 hours and then stored in polyethylene bags. The residual moisture content, which is considered to be less than 3% by mass, is calculated from the mass of sawdust seconds before and after drying at 120°C for 24 hours.

Particle size analysis of the sawdust is done using the FQA (Fibre Quality Analyser, Op Test Equipment). The analysis has been performed on more than 5000 particles. Wood flour and fibres are obtained by sieving the sawdust from the 25 mesh sieve ($\phi < 0.71\ mm$).

The composites are prepared in a twin-screw mixer contra at an angular speed of 90 RPM and the temperature of 170°C. The degradation temperature for wood fibres is around 240°C. HDPE and Fusabond are initially introduced and mixed for 2 minutes to ensure the complete fusion of the polymer mixture. In the second step, the sawdust is introduced and

kneaded for 5 minutes. Five different mass concentrations of fibres are produced: 20, 30, 40, 50, and 60%.

The samples are made in an aluminium mould using a hot press at a temperature of 150°C that is slightly above the melting temperature of the polymer. The thickness of all WPC specimens is 3.50 mm and their diameter is 79.2 mm.

The HDPE samples are prepared by cutting circular specimens with a diameter of 79.2 mm and the thickness of 1.60mm. The samples are cut from the same HDPE sheet that is used to manufacture the WPC specimens. The density of the samples is shown in Table 3-1. Figure 3-1 illustrates the WPC and HDPE samples prepared for the experiments.

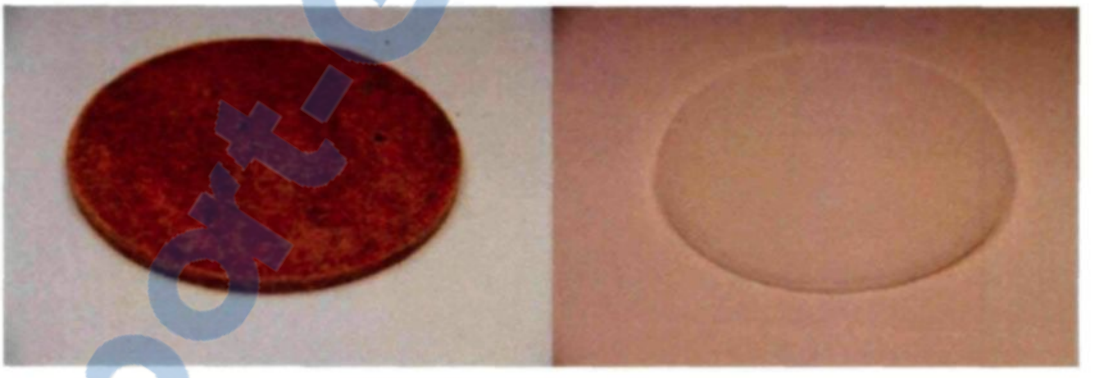

Figure 3-1 – WPC (left) and HDPE (right) specimens

Table 3-1 – The density of samples

Specimen	Density (kg/m^3)
HDPE	980
WPC20wt%	938
WPC30wt%	941
WPC40wt%	952
WPC50wt%	1051
WPC60wt%	1104

3.3 Selection of the experimental approach

As explained in the literature review, from the experimental point of view, there are several approaches to determine the mechanical properties of rubbers and thermoplastic materials. Treolar (Treolar, 1944) performed one-dimensional tests. The test consists of a simple extension, simple shear, and uniaxial compression.

There are three different types of two dimensional tests:

- Biaxial planar extension test (Meissner, Raible, & Stephenson, 1981): A test to stretch a rectangular thermoplastic membrane in two directions, the XY plane of the membrane, leaving the third direction free. This type of experiment is difficult to carry out due to the problems regarding the strain control on the flat membrane.
- Combined experiment of blowing and extension of a hollow cylinder (Alexander, 1971) (Benjeddou, Jankovich, & Hadhri, 1993): A test to use the stretch forces for extension, while at the same time blowing the cylinder using the airflow. Alexander (Alexander, 1971) used this method to study the behaviour of latex. In his work, Alexander showed the instability phenomena of latex during blowing.
- Blowing a biaxial axisymmetric membrane test (Treolar, 1944) (Rivlin & Saunders, 1951) (Joye, Poehlein, & Denson, 1973) (Verron, Marckmann, & Peseux, 2001) (Derdouri, Erchiqui, Bendada, Verron, & Peseux, 2000): A test to blow an initially flat circular membrane with the airflow. Erchiqui (Erchiqui, Derdouri, & Verron, 2001) and Verron (Verron, Marckmann, & Peseux, 2001)

used the flat circular membrane approach to study the behaviour of HIPS and ABS membranes at high temperatures.

In this project the last method, blowing a biaxial axisymmetric membrane, is selected. This selection is justified due to the accuracy of this method in large deformation experiments and simple boundary conditions in spherical coordinates. The bubble inflation technique that was introduced by Joye (Joye, Poehlein, & Denson, 1973) is the experimental approach that is relative to the last method.

3.4 Experimental setup

As mentioned above, in this project the third experimental approach is selected. The bubble inflation technique that was introduced by Joy (Joye, Poehlein, & Denson, 1973) is used in order to study the mechanical behaviour of wood-plastic composites.

The experimental setup is to model the free-flow of thin circular membranes under the effect of pressure. In this context, it is necessary to establish an experimental setup that is robust and provides accurate data for mechanical modelling. During each test the following measurements are carried out:

- The vertical displacement of the pole of the membrane, which is mostly referred to as bubble height.
- The air pressure during the experiment.
- The airflow for each experiment.

- The temperature inside the environmental test chamber.
- The duration of the test.

All of these measurements are carried out for a period of a few seconds during the blowing process. It must be emphasized that the quality of the experimental data plays a vital role concerning the problem of identification of mechanical parameters. Indeed, the experimental setup must meet several technical criteria such as, accuracy, data transfer speed, repeatability, and adaptability to the existing safety and handling standards.

3.5 Parts of setup

The experimental setup was designed and developed at the CIGELE laboratory meeting all the safety and handling standards. The experimental setup consists of four distinctive parts:

- The cylinder with the membrane on top that is connected to the pressured air line and measuring instruments.
- The environmental test chamber with a temperature range of -70°C to +180°C.
- The measuring unit, consisting of a pressure regulator, two pressure transducers, one flow meter, a thermocouple, and a laser distance sensor. This unit sends analogue signals to the data acquisition system.

- The data acquisition system connected to the measuring instruments and a computer. The data acquisition system converts the analogue signals from the measuring unit to digital data readable by a computer.

3.5.1 The cylinder

The cylinder has a uniform body with the internal diameter of $103 \pm 1\ mm$ and the thickness of $6.4 \pm 0.1\ mm$ and the depth of $100 \pm 1\ mm$. The cylinder has a cap with the external diameter of $127 \pm 1\ mm$, which is screwed on top of the main body. In the middle of the cap there is an opening with the diameter of $60 \pm 0.1\ mm$ for the membrane to sit on. Between the cap and the main body there is an aluminium circular plate with two rubber washers attached to both sides of the plate. When the cap is being screwed on to the main cylinder to mount a new membrane for a test, the force from screwing applies a pressure to the rubber washers and the aluminium o-ring, helping to seal all the openings around the membrane and to provide a sealed volume, so that there is no air leakage.

This system works as a buffer tank that penetrates the membrane with pressured air. A metal tube is welded to the bottom centre of the cylinder that is connected to the compressed air line.

The pressured air in the cylinder is distributed uniformly on the bottom surface of the membrane. The uniform distribution of air is provided by a metal diffuser that is placed

in the middle of the cylinder on top of the metal tube as a cap. The diffuser has a half sphere shape with holes on its surface to diffuse the airflow.

It is very important to make sure that the system is properly sealed and there is absolutely no air leaking out of the system. For this purpose two different tests are performed to check for air leakage.

- First test: a membrane was mounted on the system and the cylinder was filled with pressured air. The pressure was set to 80 psi and the cylinder was placed in a tank filled with water. Bubbles released in the water would reveal any small leakage in the system.
- Second test: this test is to keep the system under constant pressure for several minutes. Any small leakage in the system would be detected by changes in pressure with time. Ideally, the pressure must remain constant for a long period of time.

Figure 3-2 shows the schematic view of the cylinder. Figure 3-3 shows the cylinder with a membrane in both inflated and flat position.

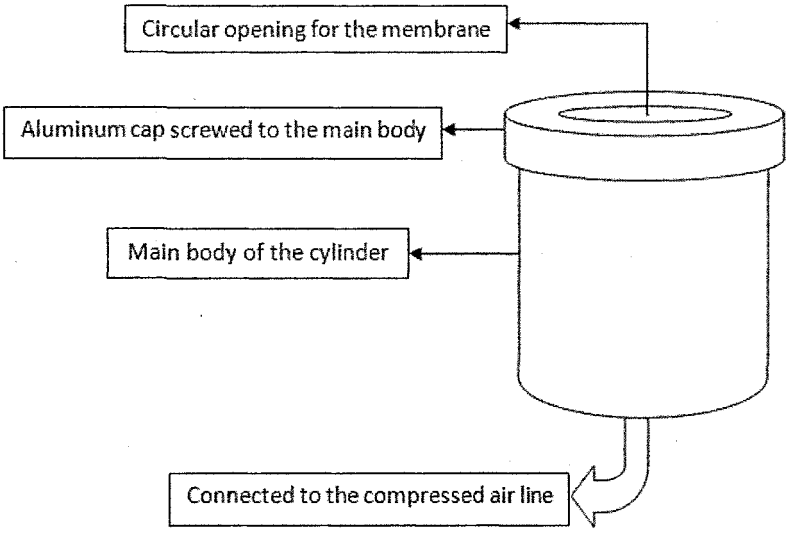

Figure 3-2 - Schematic view of the cylinder

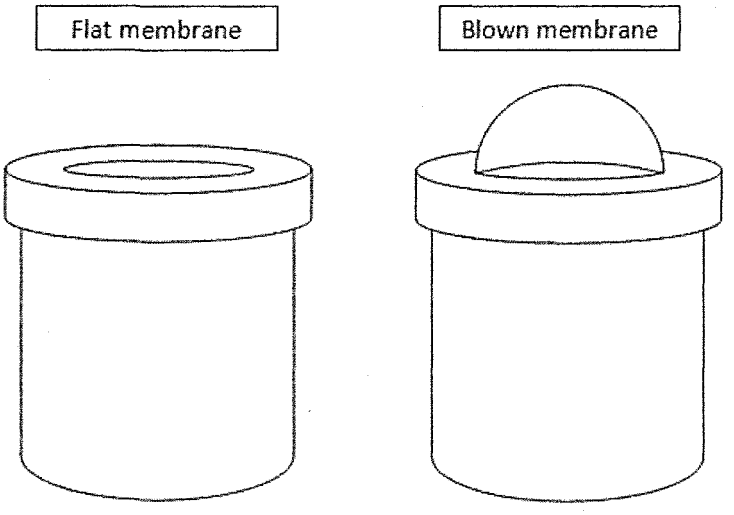

Figure 3-3 - The cylinder with flat and inflated membrane

3.5.2 The environmental test chamber

An Envirotronics E-series test chamber is used for the experiments. The chamber is capable of delivering a wide range of temperature and humidity. The chamber has a volume of 550 litres and airflow of up to 4000 CFM. The chamber has a cooling rate of $3°C/min$ and a heating rate of $5°C/min$. The minimum temperature is $-70°C$ and the maximum temperature is $+180°C$.

The cylinder is placed inside the chamber and it is screwed on to the bottom surface of the chamber to remove any potential vibrations. A hanger is attached to the side wall of the chamber for the laser distance sensor to measure the bubble height of the membrane under the air pressure.

During each test the door of the chamber is shut and sealed to maintain a uniform temperature distribution inside the chamber. There is a one inch diameter opening on the side wall of the chamber that is used for passing the compressed air line, thermocouple, and the cable for the laser distance sensor.

For each test, 40 minutes is allowed for the heating and cooling process until the chamber reaches the target temperature. The membrane is kept at the target temperature for the duration of 8 hours to make sure that it has reached a uniform temperature distribution condition throughout the whole material before blowing.

Figure 3-4 shows the Envirotronics E-series test chamber at CIGELE laboratory.

Figure 3-4 - Envirotronics test chamber at CIGELE laboratory

3.5.3 The measuring unit

Temperature measurement: to measure and record the temperature inside the chamber two references are used. The first one is the control unit of the Envirotronics test chamber that reports the temperature inside the chamber for the duration of the test. The desired temperature and humidity can be set by using the same control unit of the chamber.

The second temperature reference is the thermocouple that is placed close to the membrane and records the temperature using the data acquisition system. The thermocouple sends the electrical signals to the data acquisition system connected to the computer. The computer reads the electrical signals and converts them to the equivalent

values of temperature. The temperature values are recorded in a datasheet along with the data for the air pressure, airflow, bubble height, and the test duration.

Air pressure control: a single closed loop pressure regulator that converts a variable electrical signal into a variable pneumatic output is used to control the air pressure of the system. The pressure regulator is a complete closed loop control valve that incorporates two solenoid valves, a manifold, an integral pressure sensor, and an electrical circuit. One valve functions as inlet control and the other as exhaust. The inlet valve operates proportionally to the voltage supplied by the electrical circuit. The desired pressure for each test is sent to the electrical circuit using the computer and data acquisition system. An internal pressure transducer in the regulator measures the pressure output and provides a feedback signal to the electrical circuit. This feedback signal is compared to the command signal input. A difference between the two signals causes one of the valves to open. If the system requires additional pressure to achieve a satisfied condition the inlet valve opens proportionally to eliminate the difference signal. If the system pressure is too high the exhaust valve opens and relieves pressure until a satisfied state is achieved.

The regulator also provides an analogue output that is a conditioned signal from the internal pressure transducer for output to a panel meter and controller for data acquisition.

Air flow measurement: the flow meter is right after the pressure regulator in the measuring unit. The measuring unit consists of a pressure regulator, one flow sensor, two pressure sensors, a thermocouple, and a laser distance sensor.

The air enters the measuring unit through the pressure regulator and passes two pressure sensors and one flow meter to enter the cylinder. At the same time the thermocouple and the laser distance sensor report the values of temperature and deformation.

The flow meter measures the airflow and sends the analogue signals to the data acquisition system. The computer receives the analogue signals and converts them into digital ones using the data acquisition card. The flow values are recorded in the datasheet.

Air pressure measurement: the measurement of the air pressure is carried out by two different types of pressure transducers to increase the accuracy of the measurements.

The first pressure transducer is of Omega PX41 series that is a high accuracy and heavy-duty pressure transducer. The PX41 has the pressure range of 0-200 psi.

The second pressure transducer is of Omega PX209 series that is based on proprietary technology. The transducer uses a 4-active-arm bridge sensor with a micro-machined diffused silicon diaphragm and proprietary thin-film media, plus dielectric isolation barriers. This type of transducer uses a solid state media isolation, which makes it suitable for use with many industrial liquids and gases. The PX209 has higher pressure accuracy than PX41. The reason for using two pressure transducers is that the PX41 is a heavy-duty pressure transducer and the PX209 is of solid state type. Using the results of both types leads to a more accurate mechanical identification.

Deformation (bubble height) measurement: a position sensor, that performs the distance measurement without contact with the target, is used to monitor the height of the bubble at the centre of the membrane. The measurement range is between 5.00 and 35.00 cm. A laser beam, emitted by the sensor before the blowing adjusts the central position of the membrane. The position sensor receives the reflection of the laser beam and measures the distance during the blowing.

Figure 3-5 shows the measuring unit next to the data acquisition block and power supply at the CIGELE laboratory.

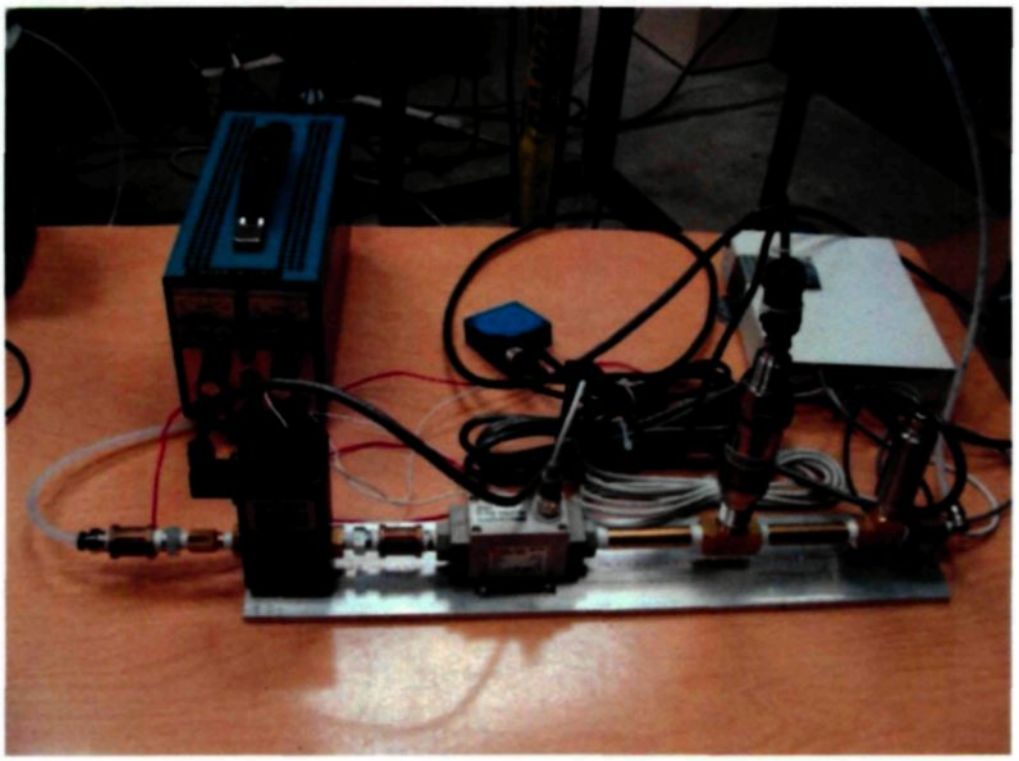

Figure 3-5 - The measuring unit at CIGELE laboratory

3.5.4 Data acquisition system

The data acquisition system of this setup consists of three main parts. The first part is the shielded input/output connector block with 100 pin connectors. All the instruments of the measuring unit are connected to this block. The block receives analogue signals as inputs from the flow meter, pressure transducers, thermocouple, and laser distance sensor. It also sends the electrical signals as output to the pressure regulator that sets the main pressure for the experiments. The input of the system varies between 0-5 or 0-10 volts depending on the measuring instrument and the output is 0-10 volts for the pressure regulator.

The input/output block is connected to the PCI data acquisition board as the second part of the data acquisition system. The board receives signals from the block and converts them to digital signals readable for the computer.

The third part of the data acquisition system is the computer software, LabVIEW, which is a virtual programming language from National Instruments. LabVIEW receives the data from the PCI board and provides the values of pressure, temperature, flow, and deformation. The data are shown as graphs in the user panel of the software and also saved into the datasheet so that they can be used to address the mechanical identification problem of the project.

Figure 3-6 shows the control panel in LabVIEW. Figure 3-7 shows the virtual programming of the setup in LabVIEW.

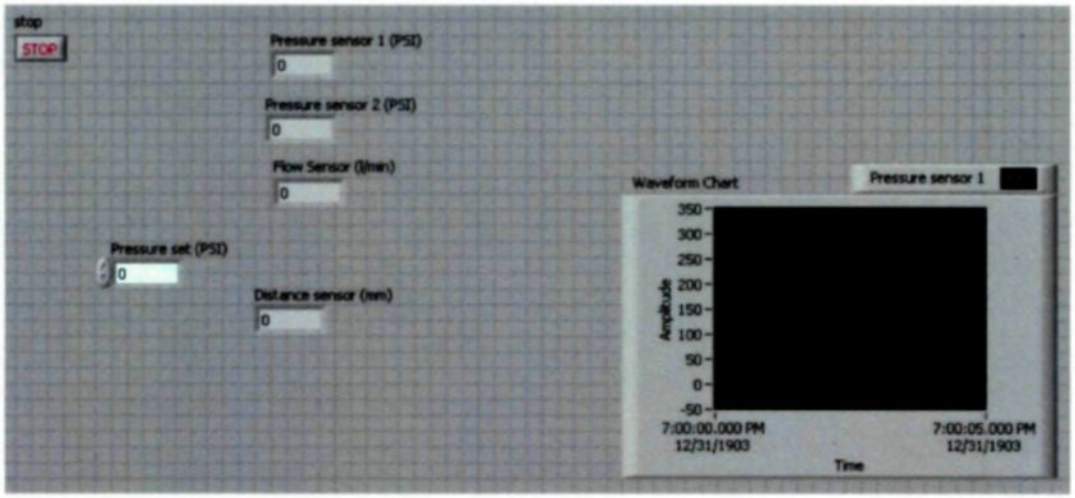

Figure 3-6 - Control panel of the experimental setup in LabVIEW

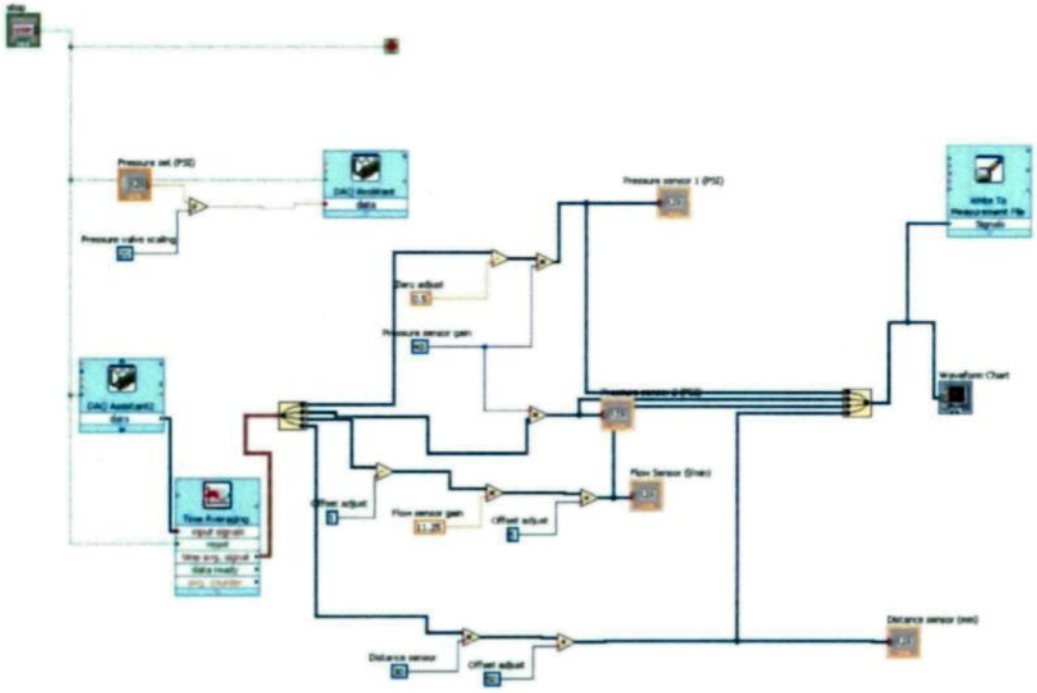

Figure 3-7 - Virtual programming of the experimental setup in LabVIEW

3.6 Mathematical modelling of the experiments

As discussed previously, the mechanical properties of polymeric materials under biaxial deformation can be obtained by bubble inflation technique (Derdouri, Erchiqui, Bendada, Verron, & Peseux, 2000) (Joye, Poehlein, & Denson, 1973). In this technique a flat circular membrane is inflated using the air pressure. During the inflation process the bubble height at the hemispheric pole and the pressure inside the bubble are measured. This technique is practical and accurate since it requires relatively simple devices.

The analytical treatment of the inflation process is complicated due to nonlinearities of the material behaviour. Numerical methods can be used to simulate and predict the inflation process of a flat circular membrane under the effect of air pressure by solving the nonlinear partial equations governing the bubble motion.

The first step of the mathematical modelling is to derive the equilibrium equations of a flat circular thermoplastic membrane under pressure. The inflation process of the membrane is considered as a steady state motion, and thus, the inertia term that contains time derivative is neglected in equilibrium equations. However, the constitutive equations remain time dependent.

A cylindrical coordinate system (r, z) as shown in Figure 3-8 is used to describe the axisymmetric inflation of a flat circular membrane. The variables r and z represent the

radial position and height of any point on the circular membrane in deformed configuration, respectively.

At time $t = 0$, the membrane is located at position $z = 0$, $r \in [0, R_0]$. R_0 is the initial radius of the membrane. A given material particle initially located at the position $(R, 0)$ is displaced to a position (r, z). On the initial condition of the membrane, R, the radial location from the axis of symmetry, can be considered as the independent dimension variable. The unknown functions of deformed configuration (r *and* z) in the equilibrium equations depend on R, the inflating pressure, and time through the constitutive model. Thus, in the equilibrium equations for the initial configuration, all derivatives are taken with respect to R.

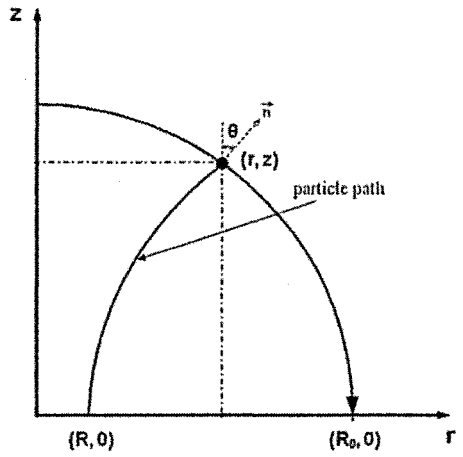

Figure 3-8 - Cross section of the membrane in cylindrical coordinate system

By making the assumption that the flat circular membrane remains axisymmetric during inflation, Feng (Feng, 1992) introduced three new variables: the stretch ratios λ_1 and

λ_2 in both meridional and circumferential directions, respectively, and the angle θ between the axis of symmetry and the vector normal to the midsurface of a deformed membrane. The stretch ratios in principle directions can be defined by the following equations in terms of deformed configuration (Bird, Armstrong, & Hassager, 1987):

$$\lambda_1 = \sqrt{(\frac{dr}{dR})^2 + (\frac{dz}{dR})^2}, \lambda_2 = \frac{r}{R}, \lambda_3 = \frac{h}{h_0} \tag{3-1}$$

where λ_3 represents the stretch ratio in the normal direction of the membrane and the derivative of z with respect to R can be defined as follows:

$$\frac{dz}{dR} = -\lambda_1 \sin\theta \tag{3-2}$$

The governing equations, which are reduced to three first order differential equations at each time step can be expressed in terms of λ_1, λ_2, and θ as follows (Feng, 1992):

$$\frac{dT_1}{dR} = \frac{R\lambda_2' + \lambda_2}{R\lambda_2}(T_2 - T_1) \tag{3-3}$$

$$\frac{d\lambda_2}{dR} = \frac{\lambda_1 \cos\theta - \lambda_2}{R} \tag{3-4}$$

$$\frac{d\theta}{dR} = \frac{\lambda_1}{T_1}\left(P - \frac{T_1}{R}\sin\theta\right) \tag{3-5}$$

where P is the experimentally measured pressure inside the bubble during the inflation. The prime denotes differentiation with respect to R. T_1 and T_2 represent the

tangential stress resultants in the surface per unit current length along the meridional and circumferential directions, respectively (Feng, 1992):

$$T_1 = h\sigma_1 = \lambda_3 h_0 \sigma_1 \tag{3-6}$$

$$T_2 = h\sigma_2 = \lambda_3 h_0 \sigma_2 \tag{3-7}$$

where h_0 and h are the thickness of the membrane in its un-deformed and deformed configurations at time t, respectively.

For Mooney-Rivlin model (Erchiqui & Kandil, 2006):

$$T_1 = 2\beta\left(\frac{\lambda_1}{\lambda_2} - \frac{1}{\lambda_1^3\lambda_2^3}\right)(1 + \alpha\lambda_2^2) \tag{3-8}$$

$$T_2 = 2\beta\left(\frac{\lambda_2}{\lambda_1} - \frac{1}{\lambda_1^3\lambda_2^3}\right)(1 + \alpha\lambda_1^2) \tag{3-9}$$

where α and β are the material constants.

During the bubble inflation experiment, it is assumed that the pressure inside the bubble is uniformly distributed at any given time and thus:

$$\frac{dP}{dR} = 0 \tag{3-10}$$

The boundary conditions are:

- The deformation is equibiaxial and axisymmetric at the pole $R = 0$: $\lambda_1 = \lambda_2$

- At the clamped rim of the membrane $R = R_0$: $\lambda_2 = 1$ and $z = 0$

Either pressure applied during the experiment or the stretch ratio λ_1 and λ_2 and z at the pole should be implemented as boundary conditions:

$$\begin{cases} P|_{r=0} = P^{exp} \\ P|_{r=R_0} = P^{exp} \end{cases} \tag{3-11}$$

$$\begin{cases} \lambda_1|_{r=0} = \lambda_2|_{r=0} = \lambda^{exp} \\ z|_{r=0} = z^{exp} \end{cases} \tag{3-12}$$

where $P^{exp}$is the measured pressure, λ^{exp} and z^{exp} are the measured value of the stretch ratio and the bubble height at the pole, respectively (the node in which $r = 0$).

Dennis and Schnabel (Dennis & Schnabel, 1983) used the above boundary conditions at each time step with the help of a variable-step-size finite difference method with deferred correction, in order to solve the following governing equations in terms of λ_1, λ_2, and θ:

$$\frac{dT_1}{dR} = \frac{R\lambda_2' + \lambda_2}{R\lambda_2}(T_2 - T_1) \tag{3-13}$$

$$\frac{d\lambda_2}{dR} = \frac{\lambda_1 \cos\theta - \lambda_2}{R} \tag{3-14}$$

$$\frac{d\theta}{dR} = \frac{\lambda_1}{T_1}\left(P - \frac{T_1}{R}\sin\theta\right) \tag{3-15}$$

When the equilibrium equations of the inflation process are solved for λ_1, λ_2, and θ, the unknowns of the problem, which are r and z can be determined using the following equations:

$$\lambda_1 = \sqrt{(\frac{dr}{dR})^2 + (\frac{dz}{dR})^2}\,, \lambda_2 = \frac{r}{R}\,, \lambda_3 = \frac{h}{h_0} \tag{3-16}$$

$$\frac{dz}{dR} = -\lambda_1 \sin\theta \tag{3-17}$$

For the purpose of modelling and simulation of the blowing phase of a polymeric membrane, assumptions of plane stresses and the incompressibility of the thermoplastic material are considered. Therefore, the components of the Cauchy stress tensor are:

$$\sigma_{13} = \sigma_{31} = \sigma_{23} = \sigma_{32} = \sigma_{33} = 0 \tag{3-18}$$

In this project, the neo-Hookean model is used to study the hyperelastic behaviour of WPCs:

$$W = C_1(I_1 - 3) \tag{3-19}$$

where C_1 is the material constant, and I_1 is the first invariant of the left Cauchy-Green deformation tensor:

$$I_1 = \lambda_1^2 + \lambda_2^2 + \lambda_3^2 \tag{3-20}$$

3.7 Conducting an experiment

For each test a WPC or HDPE membrane is placed between the cylinder cap and the main body. The cap is screwed tightly on the main body so that the system is completely sealed and there is no air leaking out. The cylinder with the membrane on top is placed in the environmental test chamber and the control unit of the chamber sets the target temperature of the test. After the target temperature is reached, the whole system will be maintained at the same temperature for a minimum duration of 8 hours to let the membrane reach a uniform temperature distribution.

After 8 hours the air enters the system through the measuring unit. The pressure regulator, using the computer and LabVIEW control panel, sets the target air pressure of the test. Throughout the test the measuring unit sends the changes in temperature, pressure, airflow, and deformation to the data acquisition system and the computer.

The laser distance sensor placed in the environmental test chamber on top of the membrane measures the changes in the deformation. One surface of the membrane is exposed to the air inside the chamber and the laser beam, and the other surface of the membrane is exposed to the pressured air in the cylinder.

The temperatures for the tests are: $-50, -25, 0, 25$, and $50°C$. LabVIEW is used to collect data from the sensors and data acquisition card. The card receives the information from the sensors in the form of voltage or amperage.

3.8 Results and discussion

This section presents the results of experiments with HDPE and wood-plastic composite membranes with 20, 30, 40, 50, and 60wt% of wood fibre, under the combined effect of temperature and pressure. The membranes are tested within the temperature range of −50°C to +50°C with 25°C increments. The membranes are tested under the maximum pressure of 18 psi. Each membrane was kept in the environmental test chamber for the duration of eight hours, in order to reach a uniform temperature distribution throughout the whole membrane. Each experiment is repeated three times, and the result presented for each membrane at each temperature, represents the average of three experiments. The error bars on the graphs represent the error in measurements and the deviation between the graphs.

Figure 3-9 shows the deformation of HDPE at different temperatures under the maximum pressure of 18 psi.

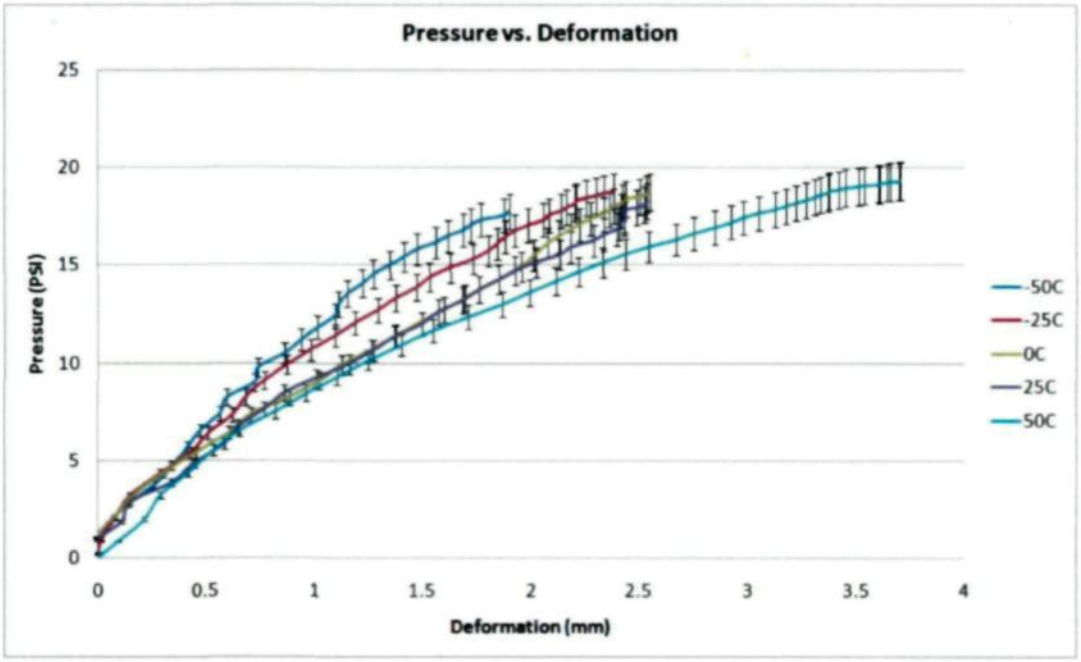

Figure 3-9 - Pressure vs. Deformation for HDPE

Figures 3-10 to 3-14 show the deformation of WPCs with 20, 30, 40, 50, and 60wt%of wood fibre using the bubble inflation technique at different temperatures under the maximum pressure of 18 psi.

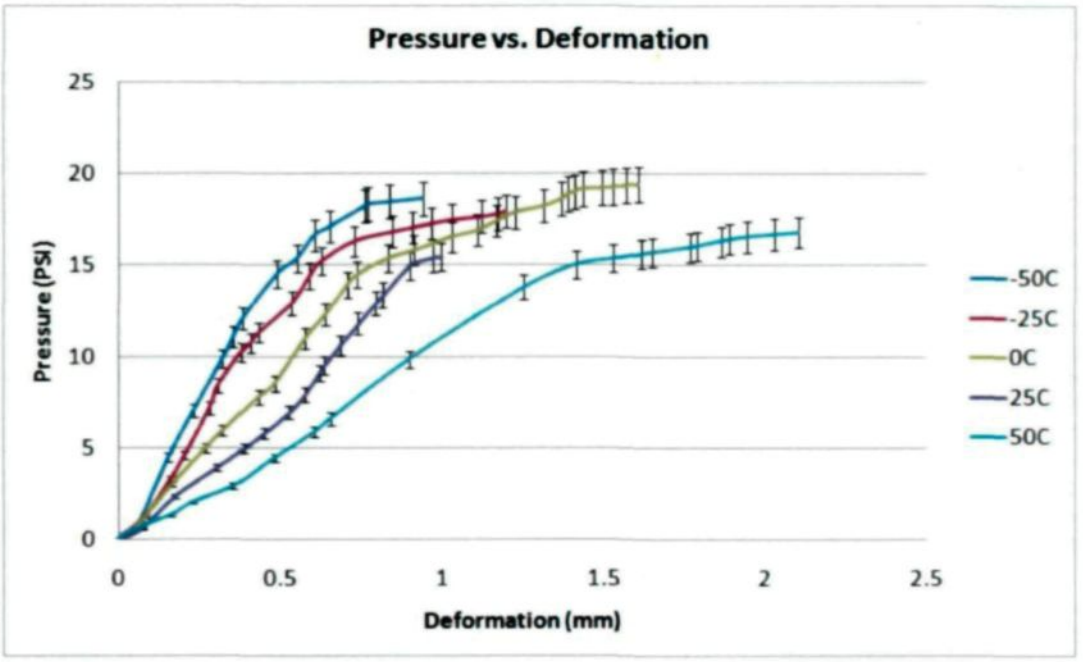

Figure 3-10 - Pressure vs. Deformation for WPC 20wt%

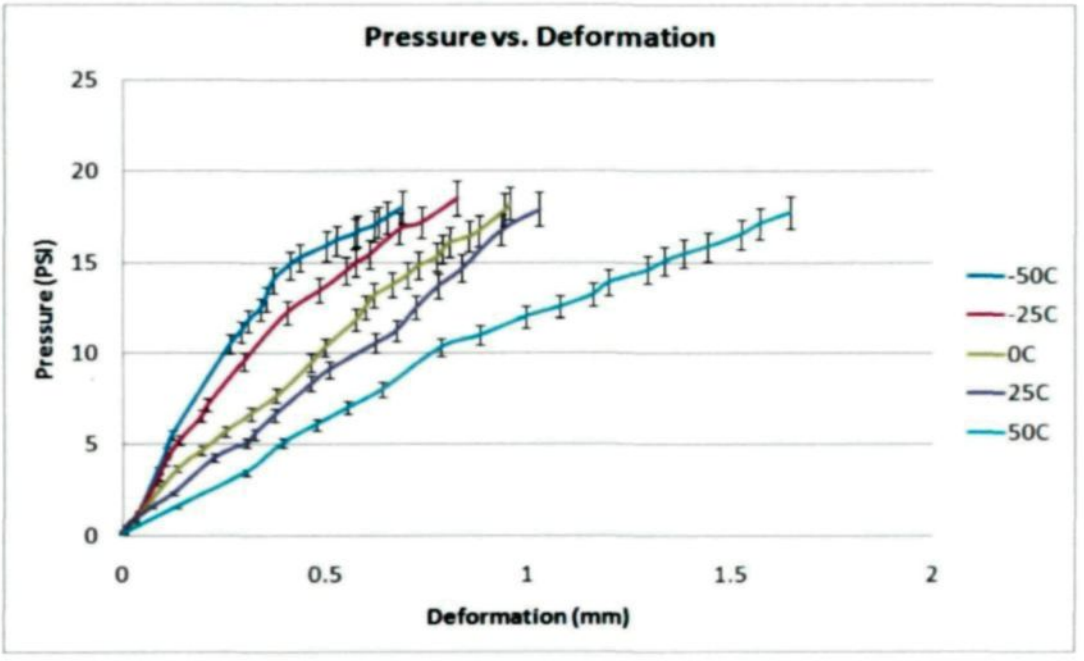

Figure 3-11 - Pressure vs. Deformation for WPC 30wt%

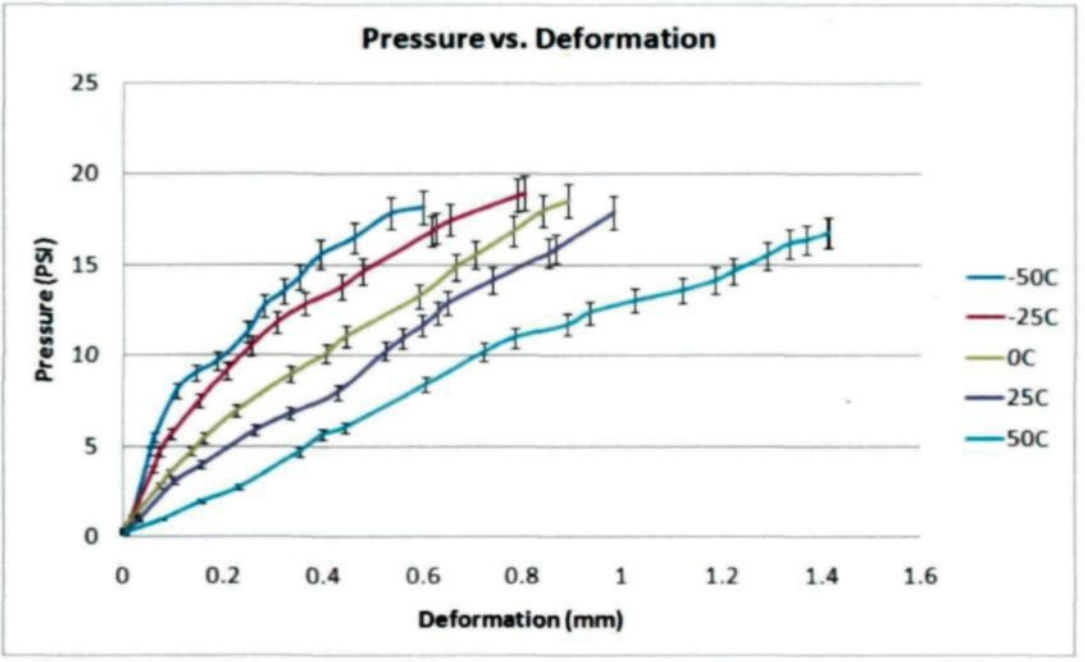

Figure 3-12 - Pressure vs. Deformation for WPC40wt%

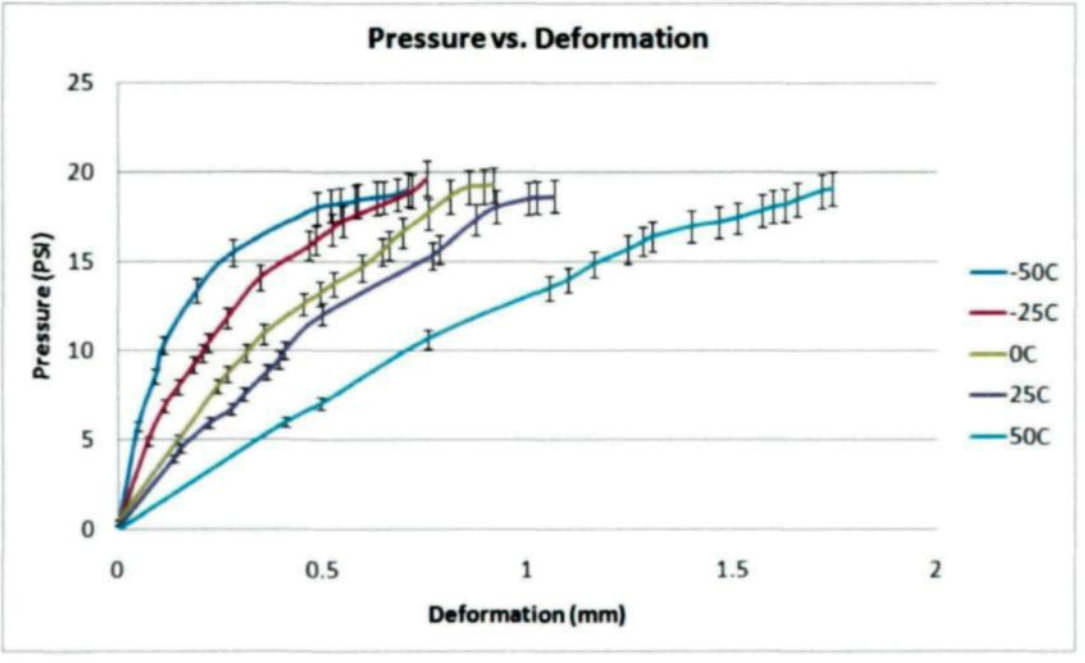

Figure 3-13 - Pressure vs. Deformation for WPC50wt%

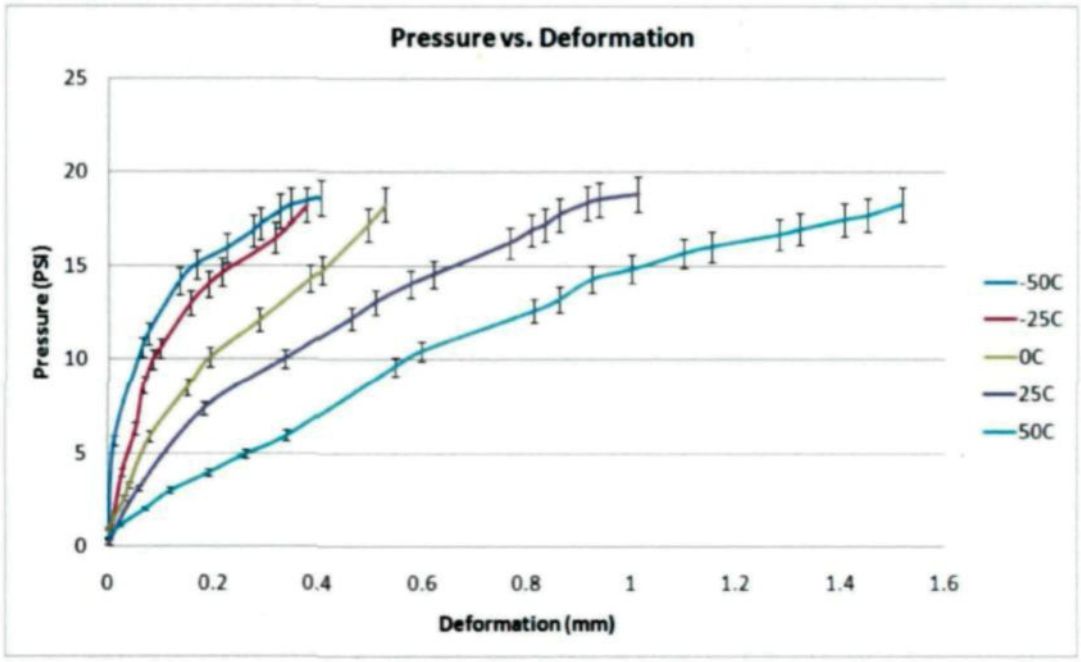

Figure 3-14 - Pressure vs. Deformation for WPC60wt%

It is observed that wood plastic composites and HDPE are elastic in response to pressure at cold temperatures. Erchiqui (Erchiqui, Ozdemir, Souli, Ezzaidi, & Dituba-Ngoma, 2011) studied the viscoelasticity of these materials at thermoforming temperatures. During the inflation the maximum height is in the centre of the membrane.

It is observed that the deformation of the membrane, under the same pressure, decreases with decreasing temperature. Therefore, it can be understood that the material has a higher stiffness in cold temperatures even though it may become more brittle.

For HDPE the maximum deformation at 50°C is measured as 3.7 mm. However, the maximum deformation at −50°C is only 1.9 mm. For WPC with 60wt% of wood fibre the maximum deformation at 50°C is measured as 1.52 mm and the maximum deformation at

−50°C is 0.40 mm. Figures 3-15 to 3-19 compare the deformation of different membranes at different temperatures.

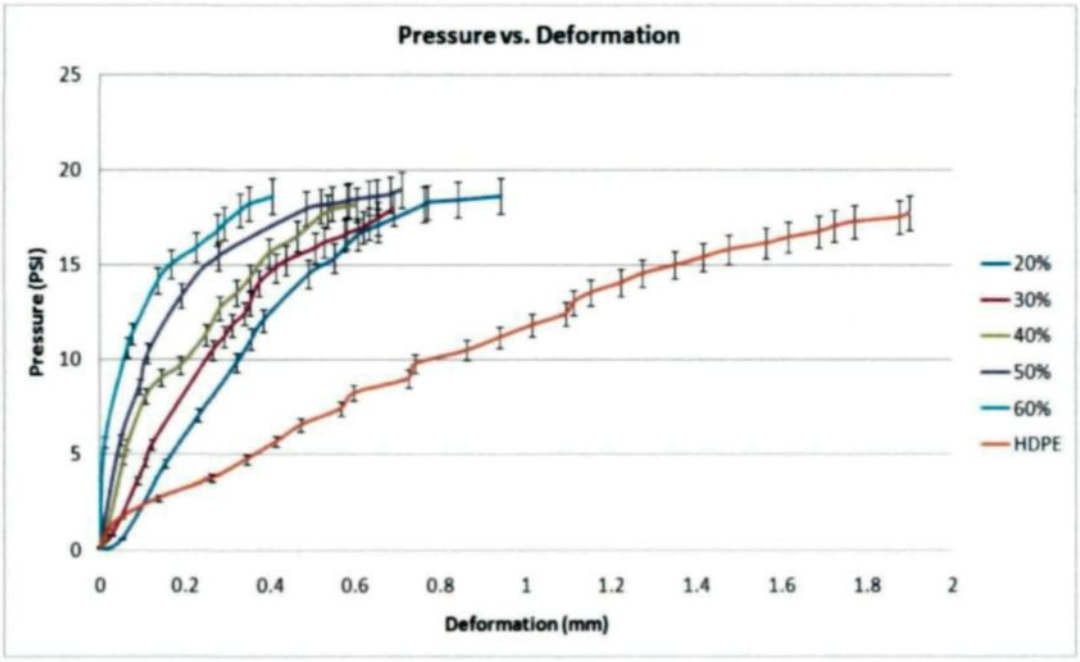

Figure 3-15 - Deformation of different membranes at -50°C

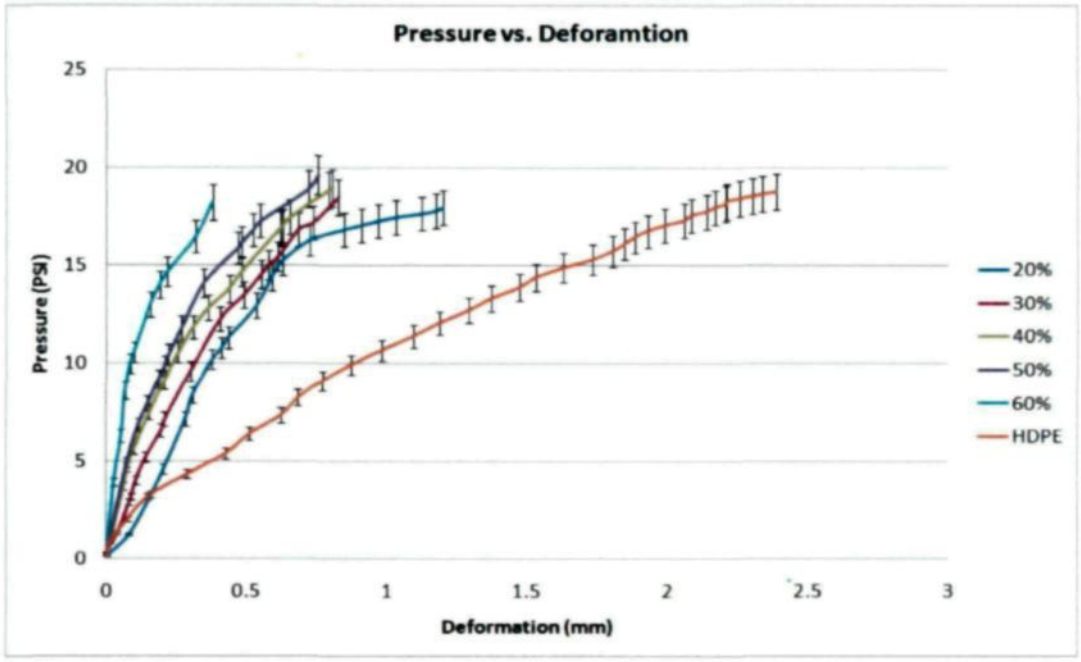

Figure 3-16 - Deformation of different membranes at -25°C

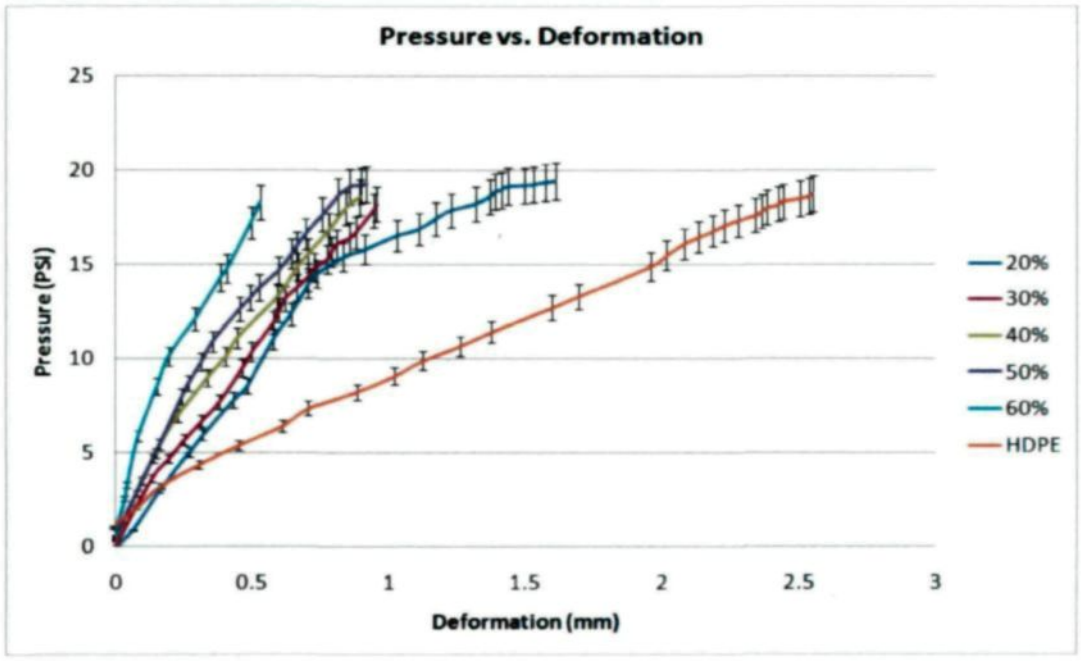

Figure 3-17 - Deformation of different membranes at 0°C

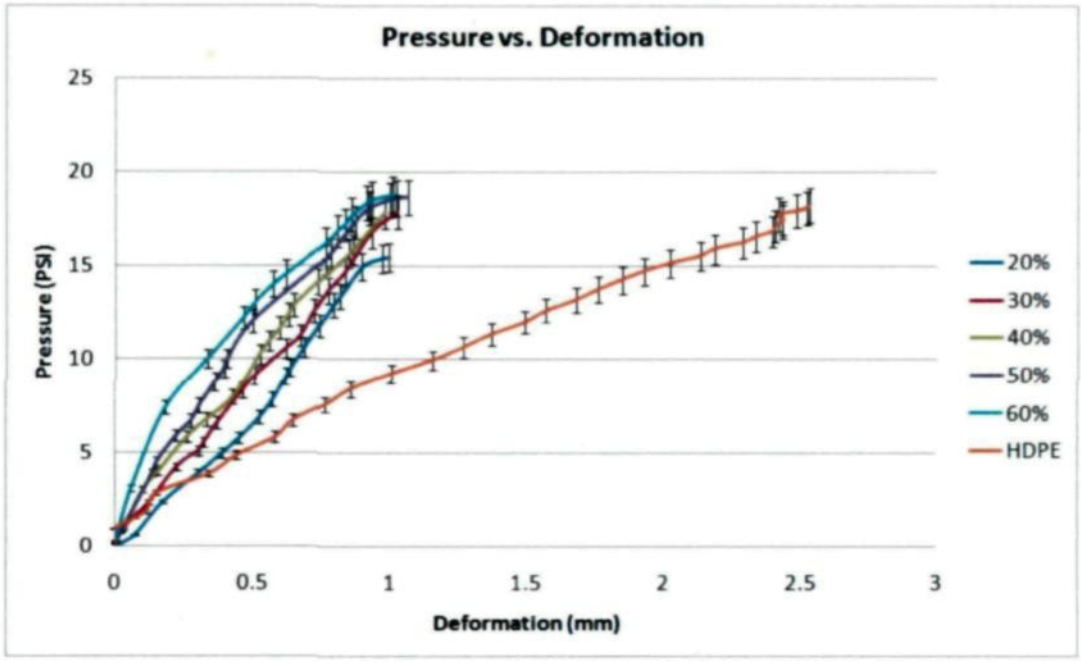

Figure 3-18 - Deformation of different membranes at 25°C

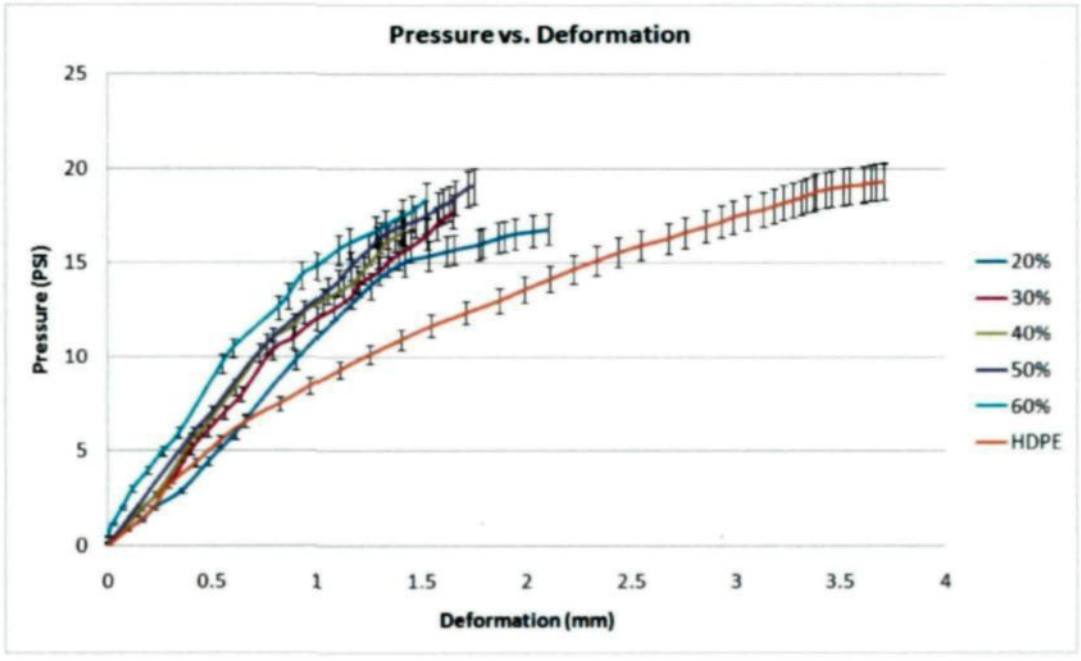

Figure 3-19 - Deformation of different membranes at 50°C

It is observed that the addition of wood fibre increases the material performance under pressure at different temperatures. However, as it can be seen from Figures 3-15 to 3-19, at colder temperatures the difference between the deformations of WPCs and HDPE is much higher as compared to high temperatures.

3.9 Conclusion

In this chapter the experimental aspects of the project were explained in detail. The following topics were covered:

- Material preparation
- Selection of an experimental approach
- Experimental setup
- Mathematical modelling of the bubble inflation
- Conducting an experiment
- Results

The results obtained from the experiments will be used in the material characterization in the following chapters in order to find the material constants for elastic and hyperelastic models.

CHAPTER 4

FINITE ELEMENT MODELLING

4.1 Introduction

In this chapter the computer modelling aspects of the project are explained. The aim of the computer modelling is to provide a learning library for the Artificial Neural Networks in order to obtain the optimum material constants.

The elastic and hyperelastic behaviour of the membranes are modelled using the finite element package, Abaqus. A membrane with the same boundary conditions as the experiments is designed in Abaqus and the pressure values from the experiments are used to measure the deformation of the membrane.

At the end of this chapter, the stress distribution in the membrane under the pressure, and the values of von Mises principal stresses are provided.

4.2 Preparation

After gathering the experimental results using the bubble inflation technique, the next step in material characterization is to perform a number of computer simulations. For the purpose of finite element modelling, three classes of materials have been selected:

HDPE and WPCs with 30 and 60wt% of wood fibre. These three classes of materials represent both extremes and the average class, concerning the percentage of wood fibre. The simulations are carried out at three different temperatures: $-50°C$, $0°C$, and $50°C$.

4.3 Simulation approach

In this project, Abaqus is used for the computer modelling and finite element analysis. Abaqus is used in the automotive, aerospace, and industrial products industries. The product is popular with academic and research institutions due to the wide material modelling capability, and the program's ability to be customized.

The aim of the project is to study the elastic and hyperelastic behaviour of HDPE and WPCs at cold temperatures. In order to fulfil this goal, Hooke's law and the neo-Hookean model have been selected for the elastic and hyperelastic modelling, respectively.

For the purpose of simulations, eight pressure values with respect to each experiment have been selected. The maximum bubble heights under each pressure, with different material constants, are measured in Abaqus. As a result, for each material constant, the bubble heights at eight different pressures form a pressure-vs-deformation graph. These graphs are shown in different colours in Figures 4-2 to 4-10 and 4-12 to 4-20. This approach is used for each class of material at different temperatures in order to generate the required data for the neural network.

4.4 Elastic simulation

As mentioned above, Abaqus is used in order to simulate the elastic behaviour of the membranes under the combined effect of temperature and pressure. The membrane with the exact diameter and thickness as samples used in the experiments is modelled in Abaqus using 4-node shell element. The model is simulated with the same pressure values and the boundary conditions as in the experiments. Figure 4-1 shows an example of the model in Abaqus under the effect of pressure.

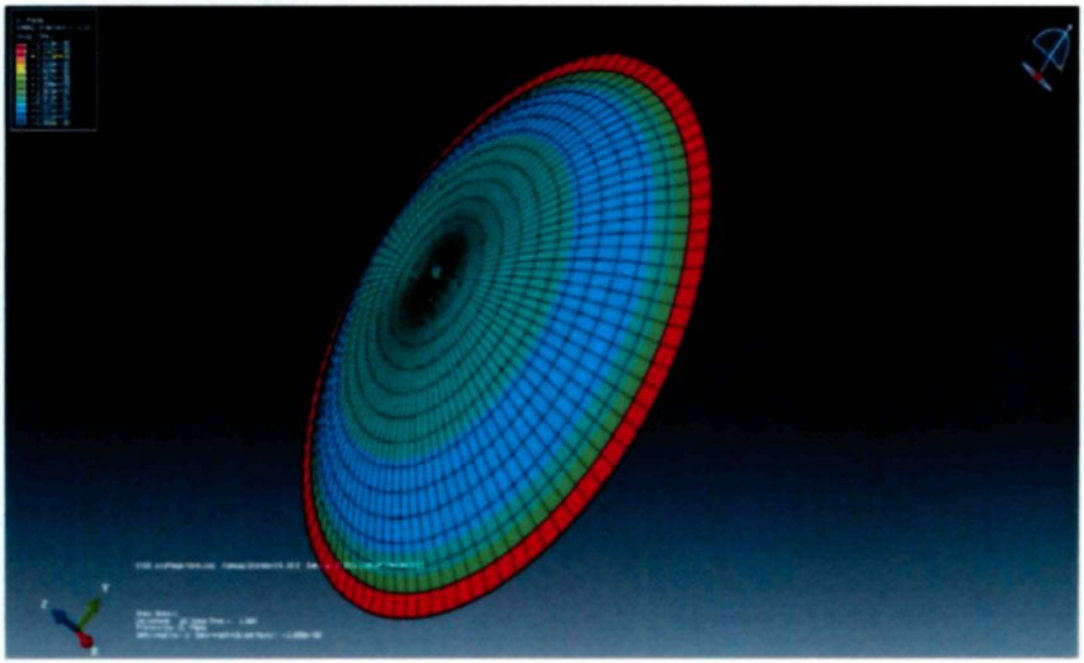

Figure 4-1 - Membrane with elastic behaviour under pressure (modelled in Abaqus)

For each class of material at each temperature, at least six simulations are carried out. Each simulation corresponds to a specific value for the Young's modulus. The

Poisson's ratio is fixed to be 0.3 for HDPE and WPCs assuming a complete elastic response.

Figures 4-2 to 4-10 show the results of elastic simulations with HDPE and WPC membranes with 30 and 60wt% of wood fibre. Each line on the graphs corresponds to the elastic behaviour of the material with a specific value for the material constant (E).

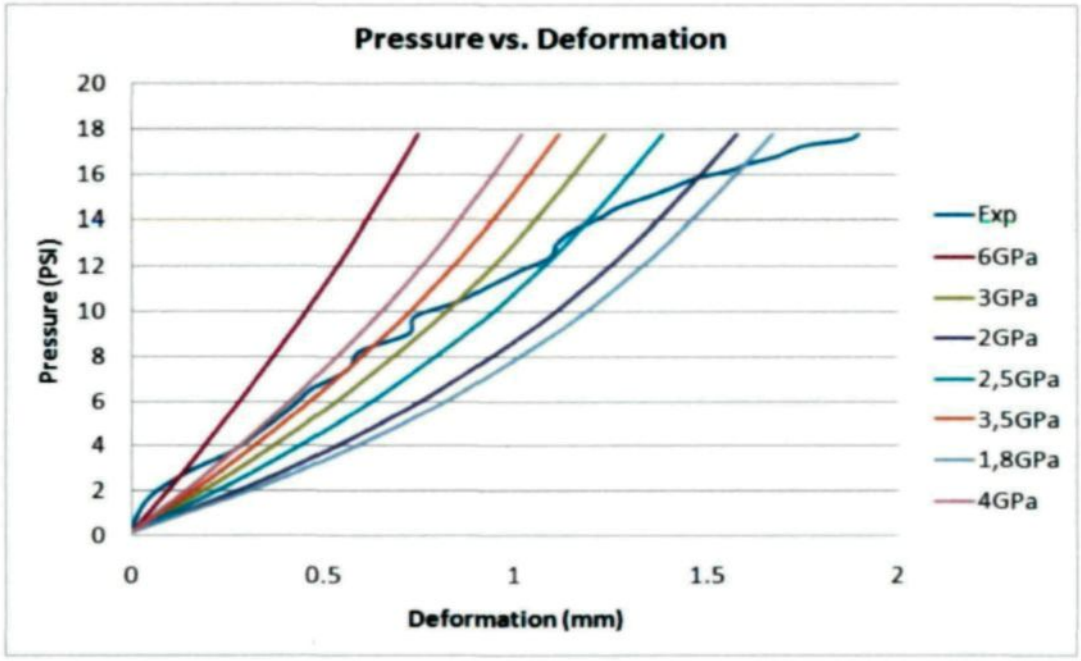

Figure 4-2 - Elastic simulations for HDPE at -50°C

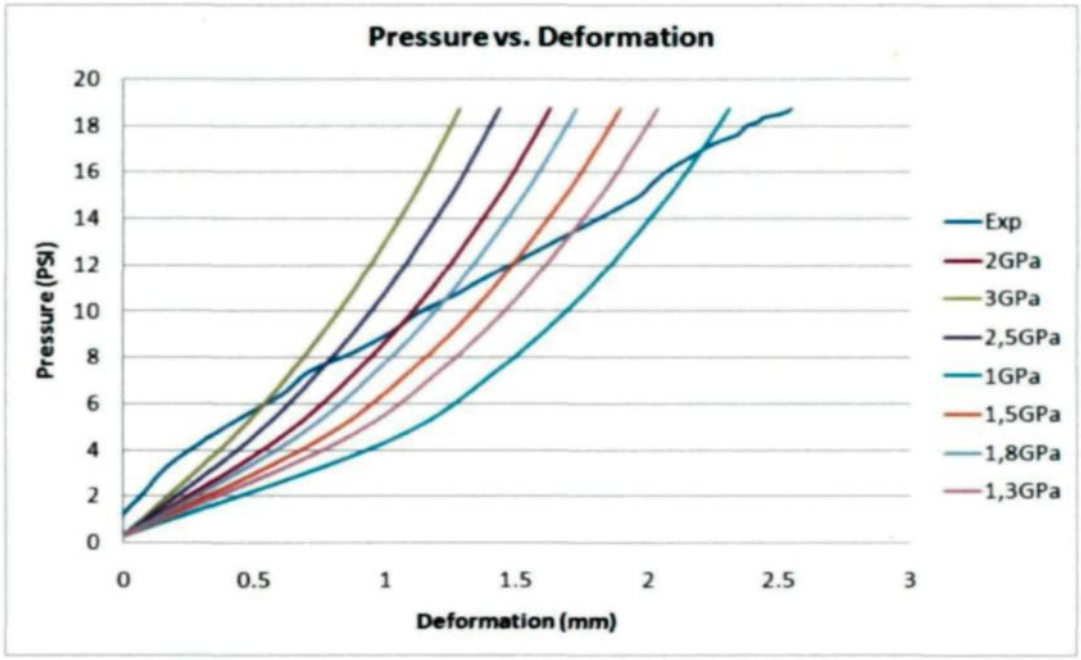

Figure 4-3 - Elastic simulations for HDPE at 0°C

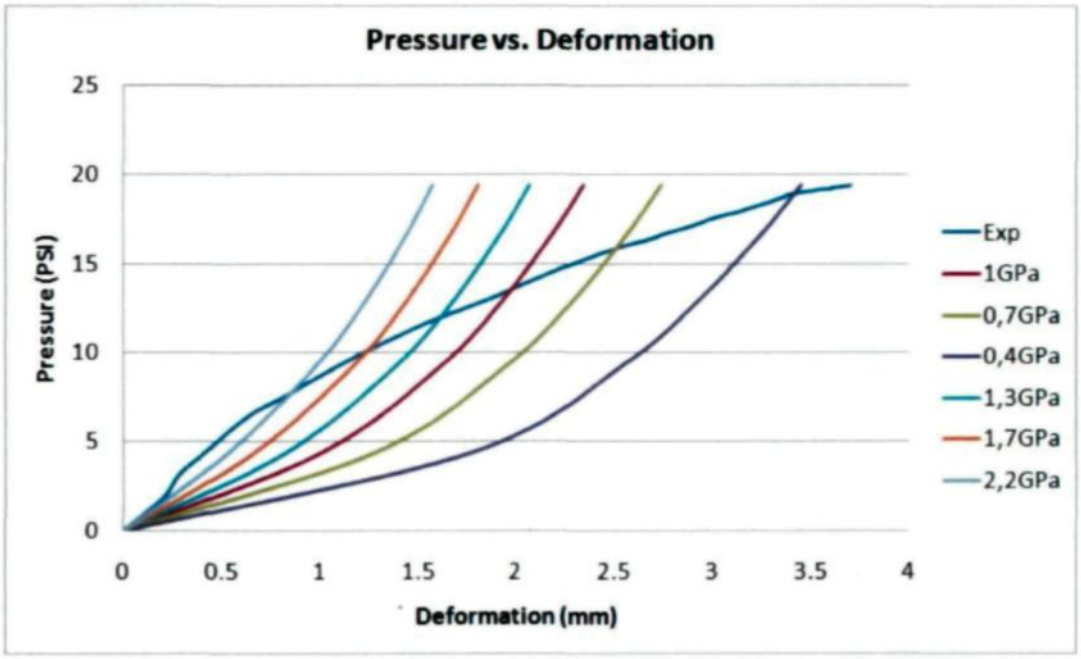

Figure 4-4 - Elastic simulations for HDPE at 50°C

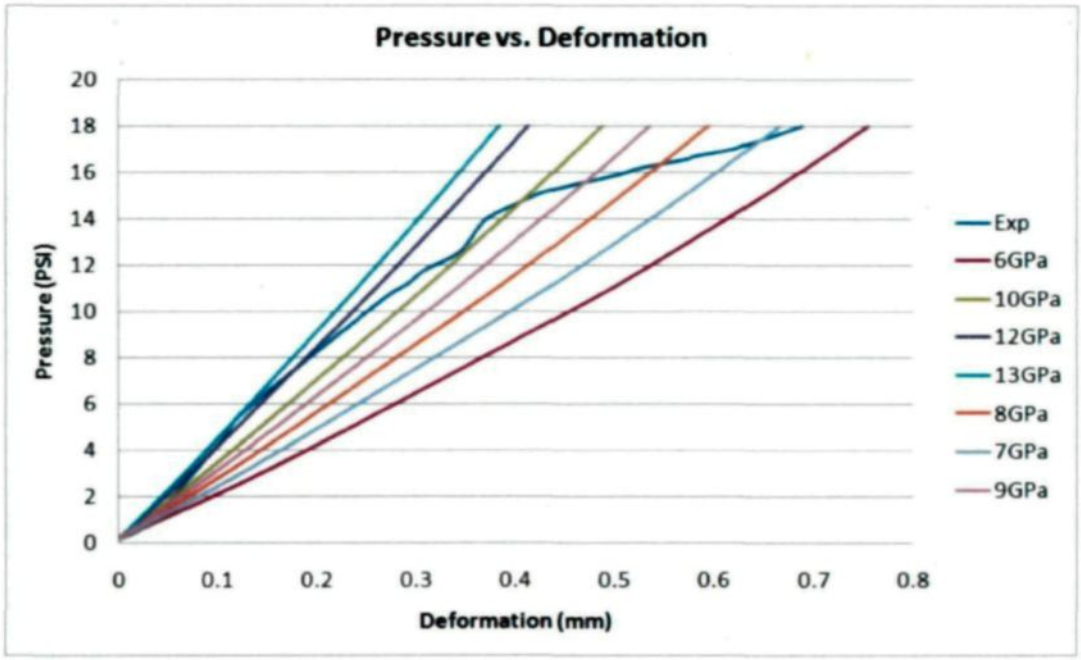

Figure 4-5 - Elastic simulations for WPC30wt% at -50°C

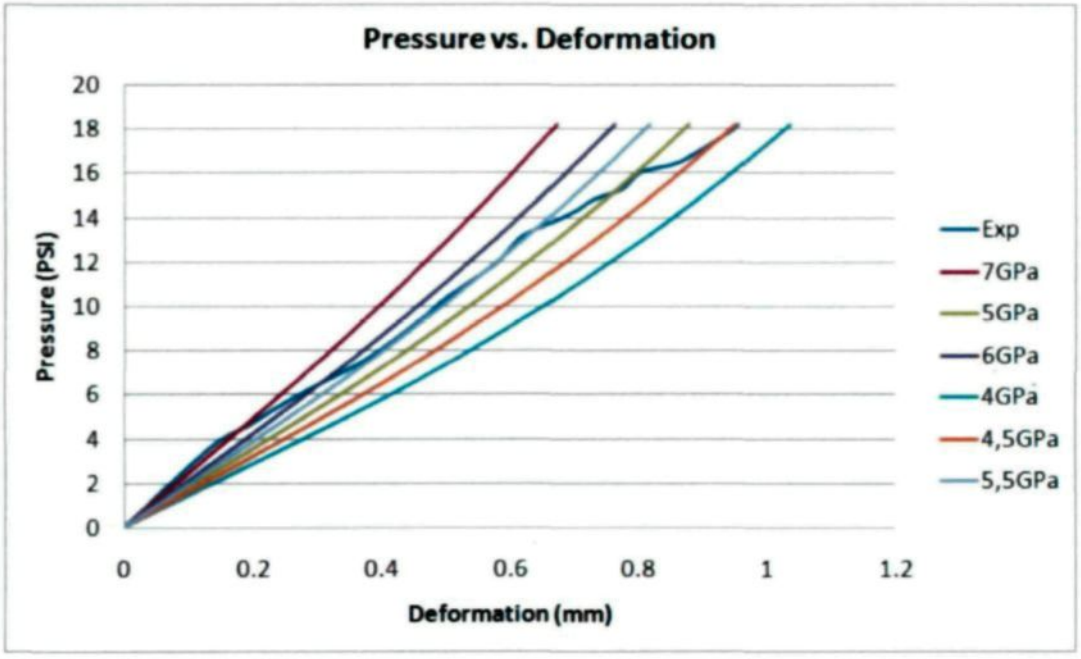

Figure 4-6 - Elastic simulations for WPC30wt% at 0°C

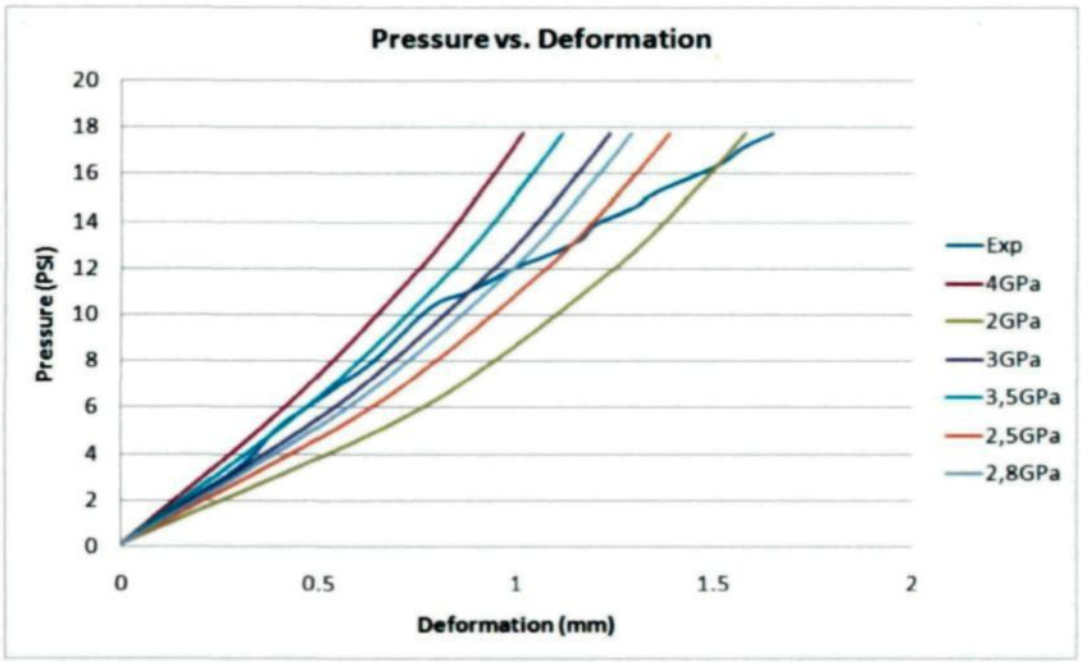

Figure 4-7 - Elastic simulations for WPC30wt% at 50°C

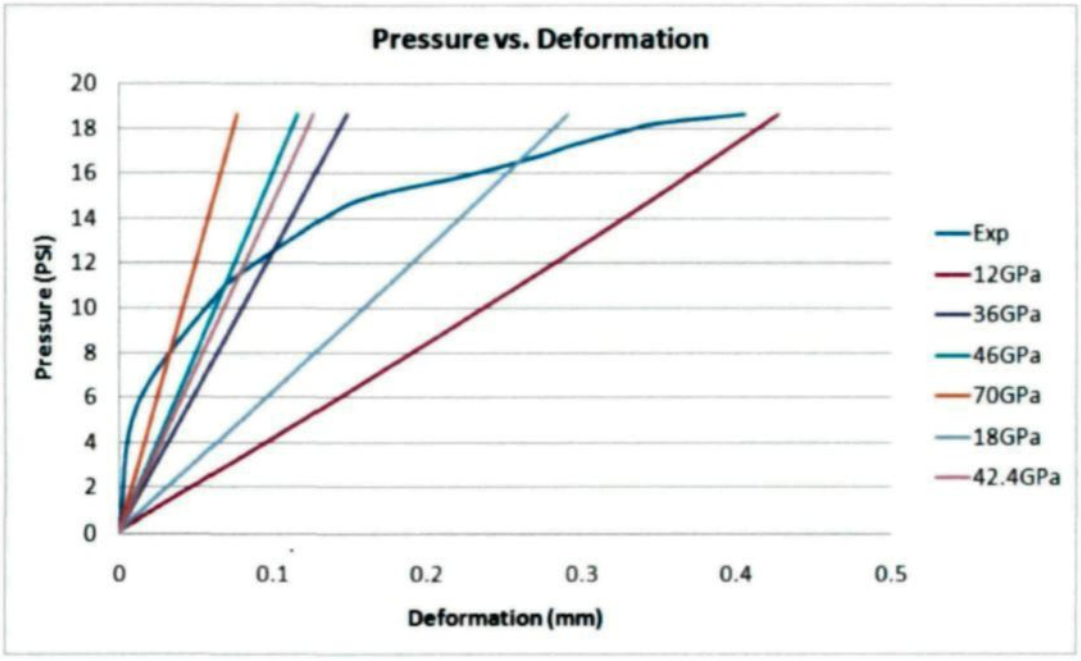

Figure 4-8 - Elastic simulations for WPC60wt% at -50°C

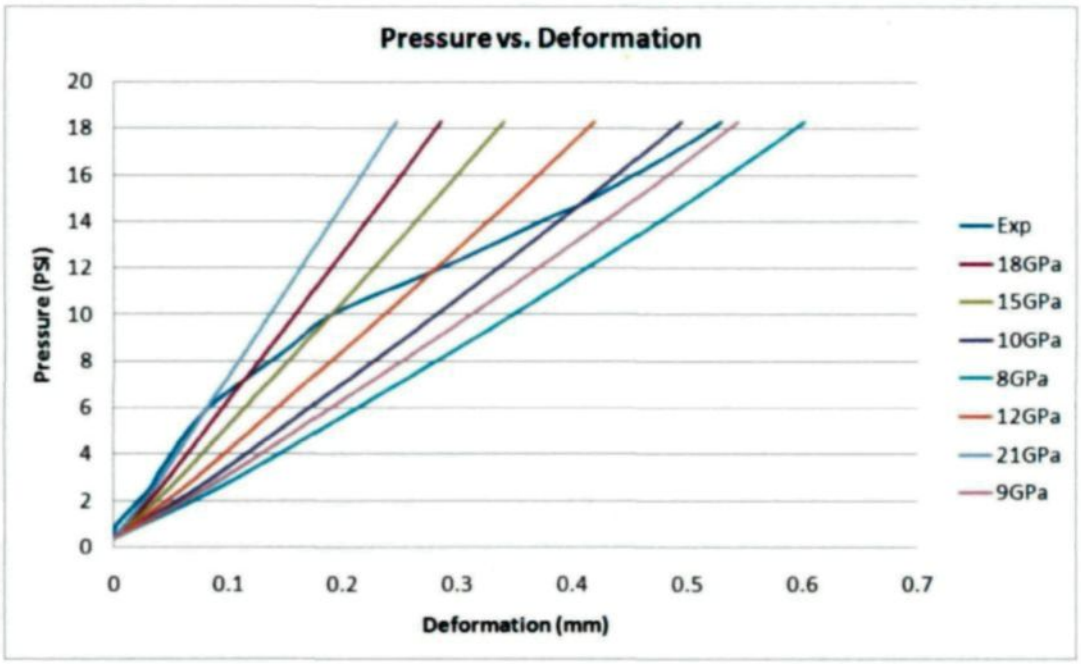

Figure 4-9 - Elastic simulations for WPC60wt% at 0°C

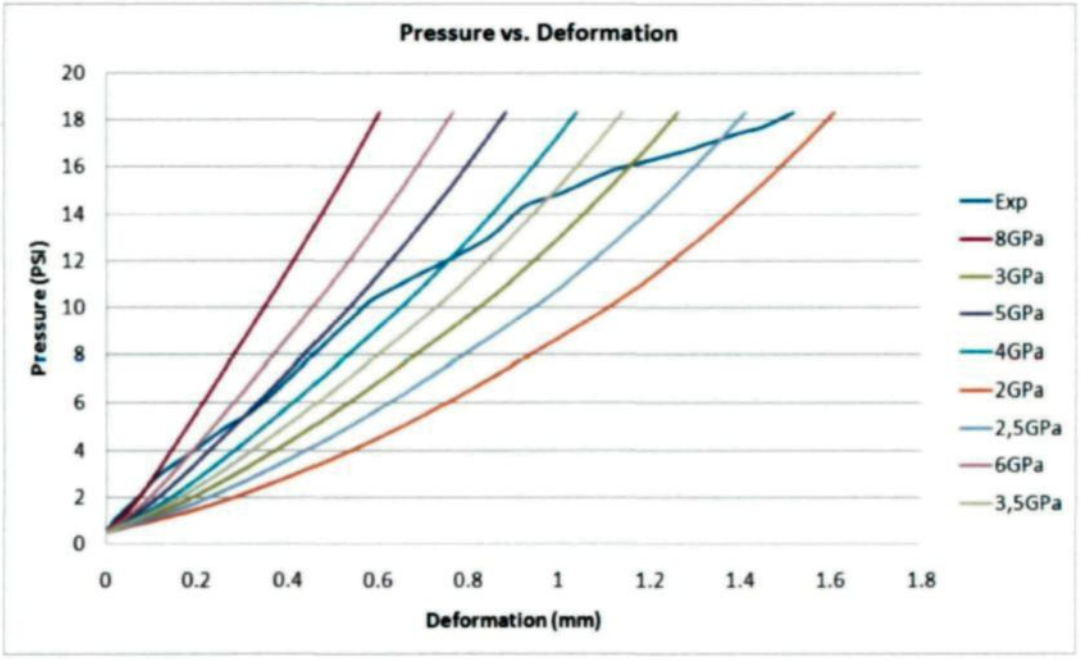

Figure 4-10 - Elastic simulations for WPC60wt% at 50°C

Each of the above graphs represents a specific type of membrane at a specific temperature. For example, for WPC60wt% at 50°C, the experimental results and the results from eight simulations are shown in Figure 4-10. Each of the eight elastic simulations corresponds to a specific value of the material constant.

The material constant in this case is Young's modulus (E) in

$$\sigma = E\varepsilon \tag{4-1}$$

where E is also known as elastic modulus.

4.5 Hyperelastic simulation

The neo-Hookean hyperelastic model is used to simulate the hyperelastic behaviour of the membranes in Abaqus. The design of the membrane and the boundary conditions are similar to the ones that were used for the elastic simulations and the experiments. Figure 4-11 shows the membrane under pressure using a hyperelastic model in Abaqus.

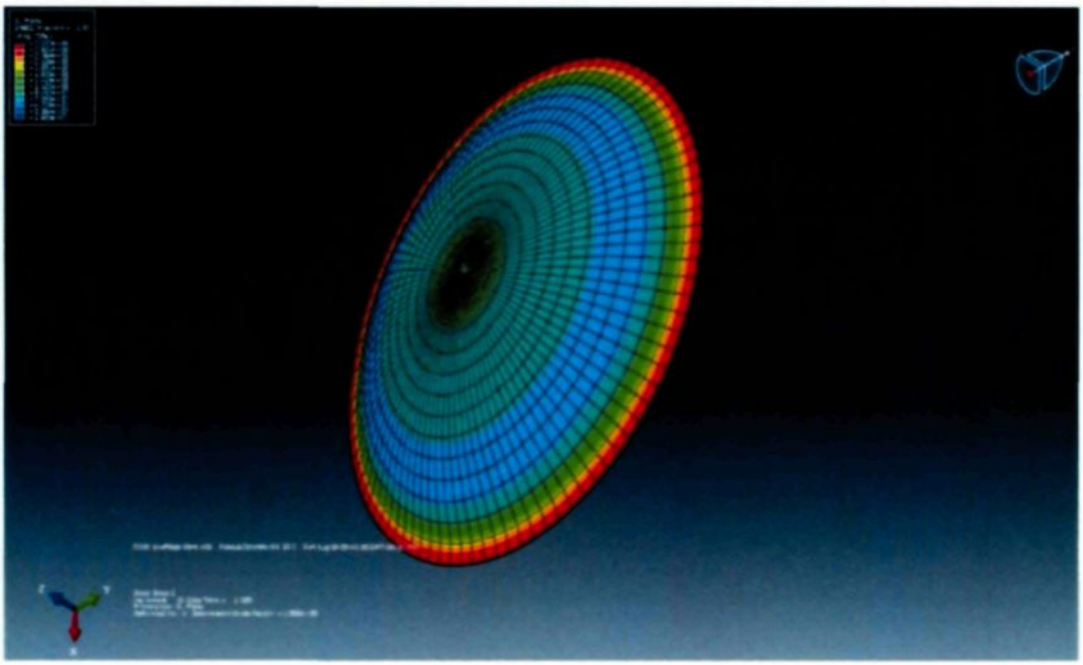

Figure 4-11 - Membrane with hyperelastic behaviour under pressure (modelled in Abaqus)

HDPE and WPC samples with 30 and 60wt% of wood fibre are selected for the simulations. The simulations are carried out based on the pressure values from the experiments at -50°C, 0°C, and $+50$°C. At least six simulations are carried out for each class of material at each temperature. Each simulation corresponds to a specific value of C_1 in the neo-Hookean model.

Figures 4-12 to 4-20 show the results of the simulations for the above mentioned materials. The pressure values are in psi and the deformation values are reported in millimetres.

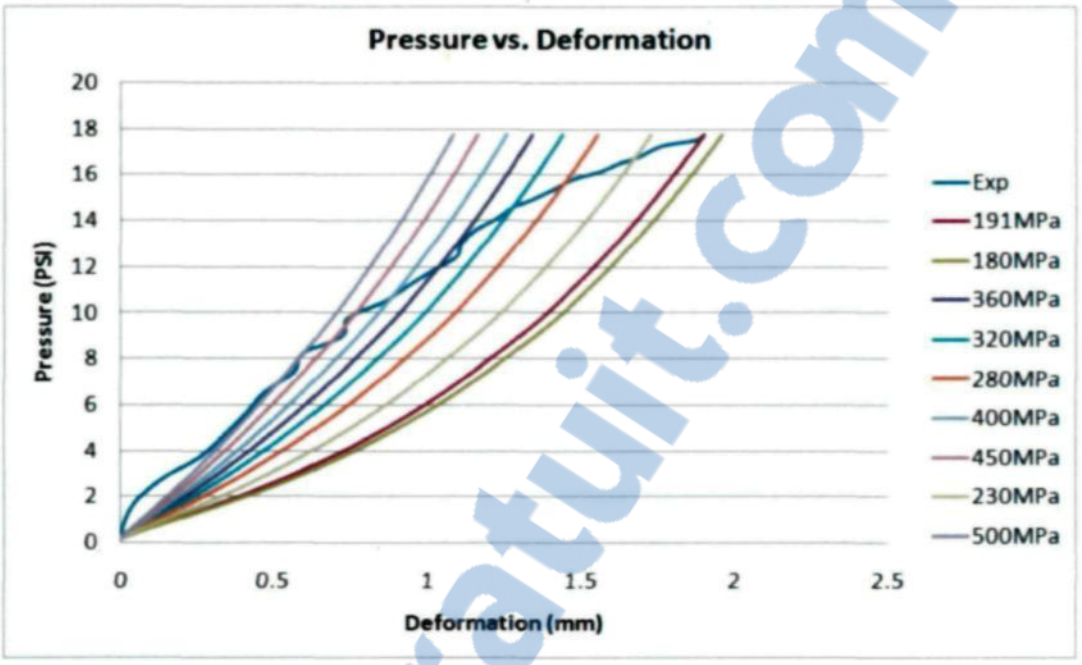

Figure 4-12 - Hyperelastic simulations for HDPE at -50°C

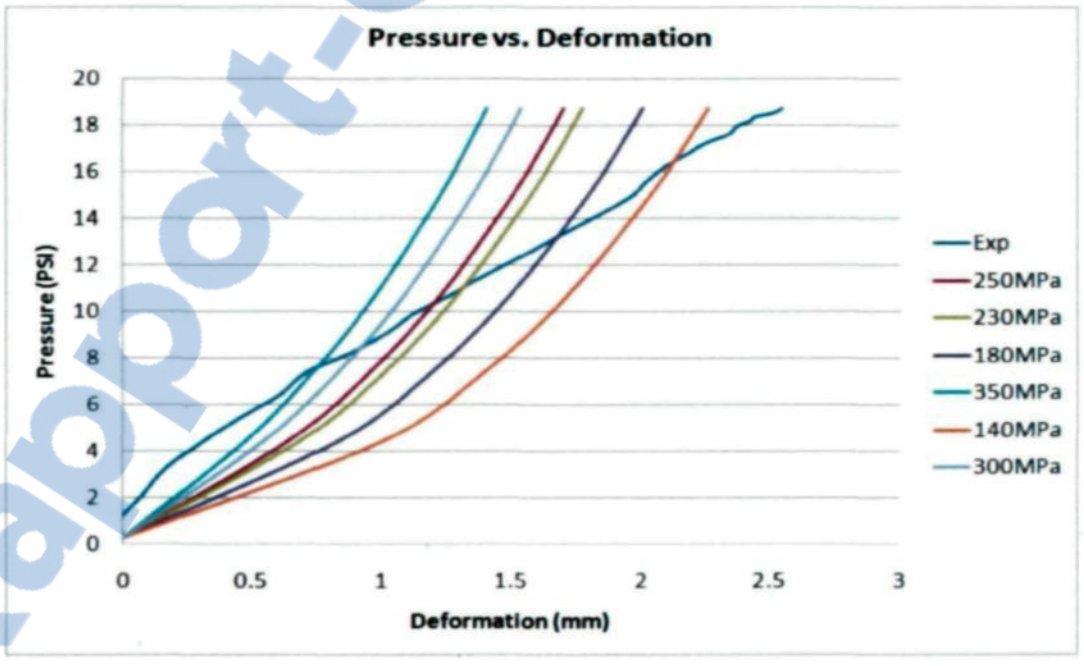

Figure 4-13 - Hyperelastic simulations for HDPE at 0°C

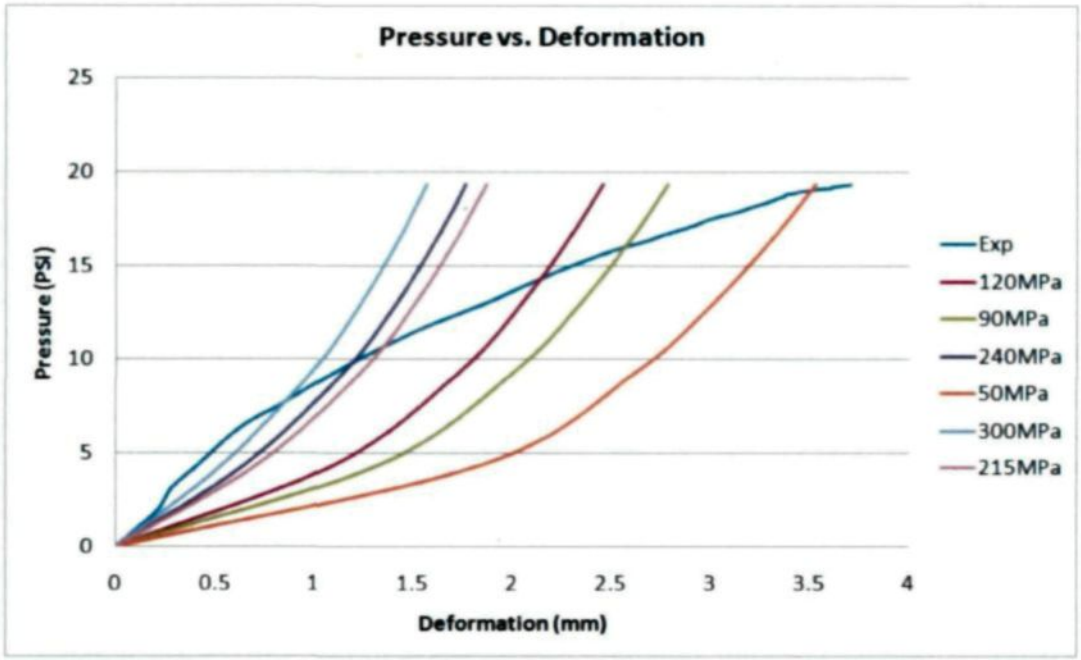

Figure 4-14 - Hyperelastic simulations for HDPE at 50°C

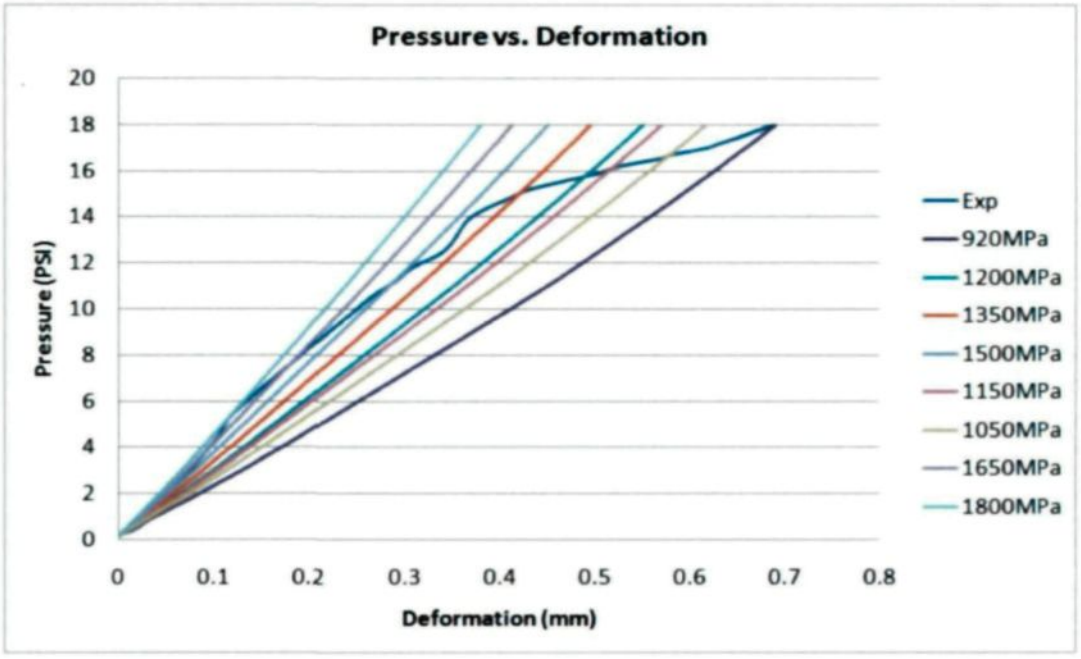

Figure 4-15 - Hyperelastic simulations for WPC30wt% at -50°C

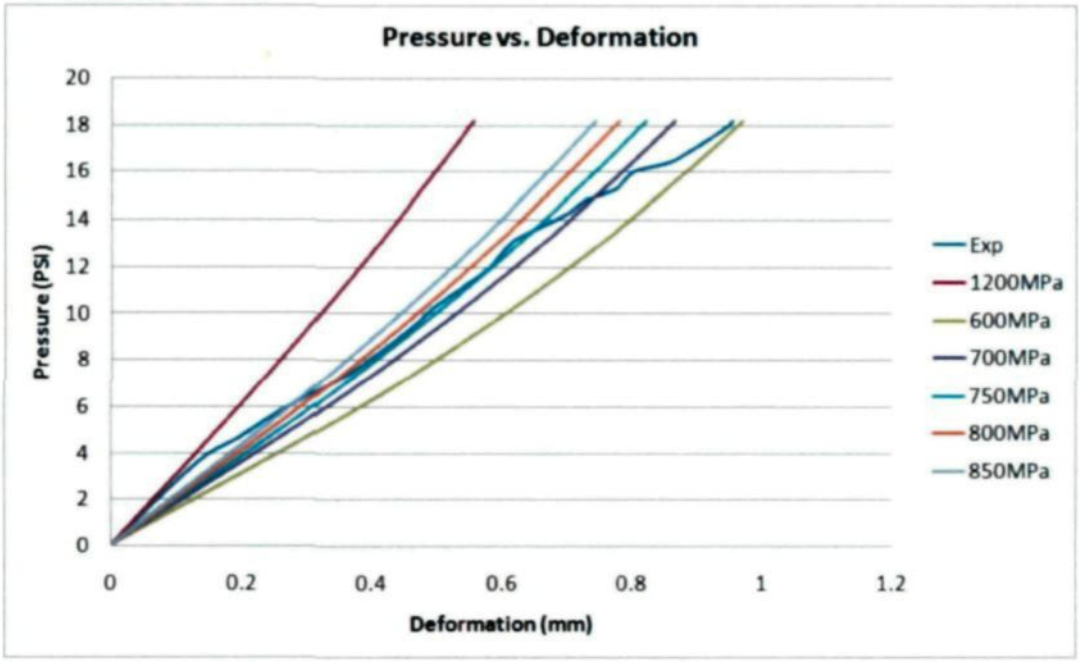

Figure 4-16 - Hyperelastic simulations for WPC30wt% at 0°C

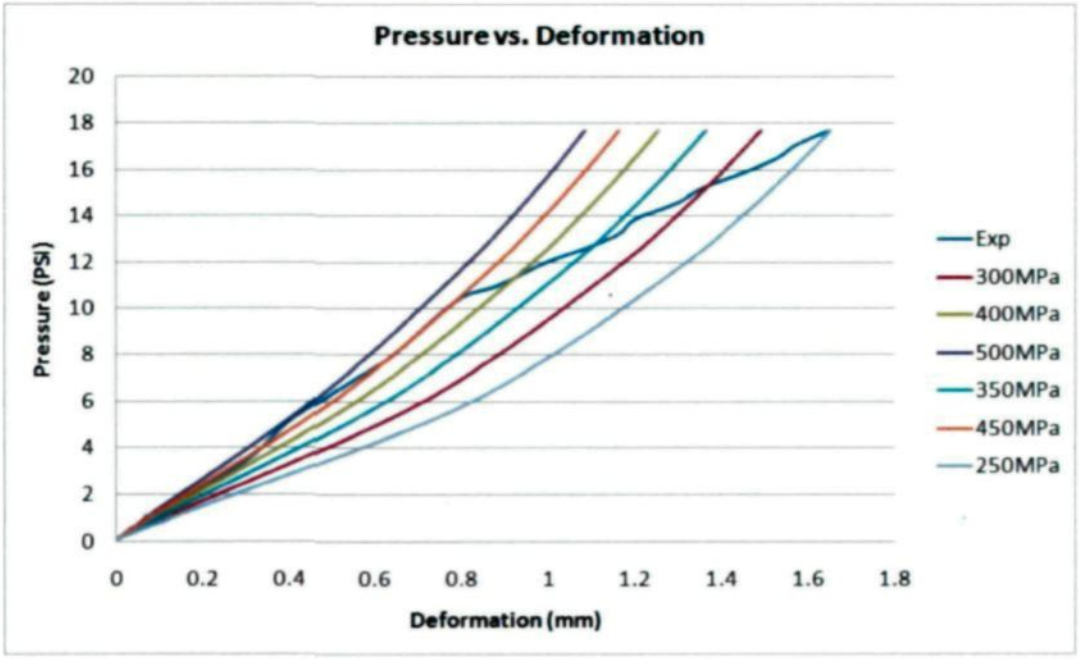

Figure 4-17 - Hyperelastic simulations for WPC30wt% at 50°C

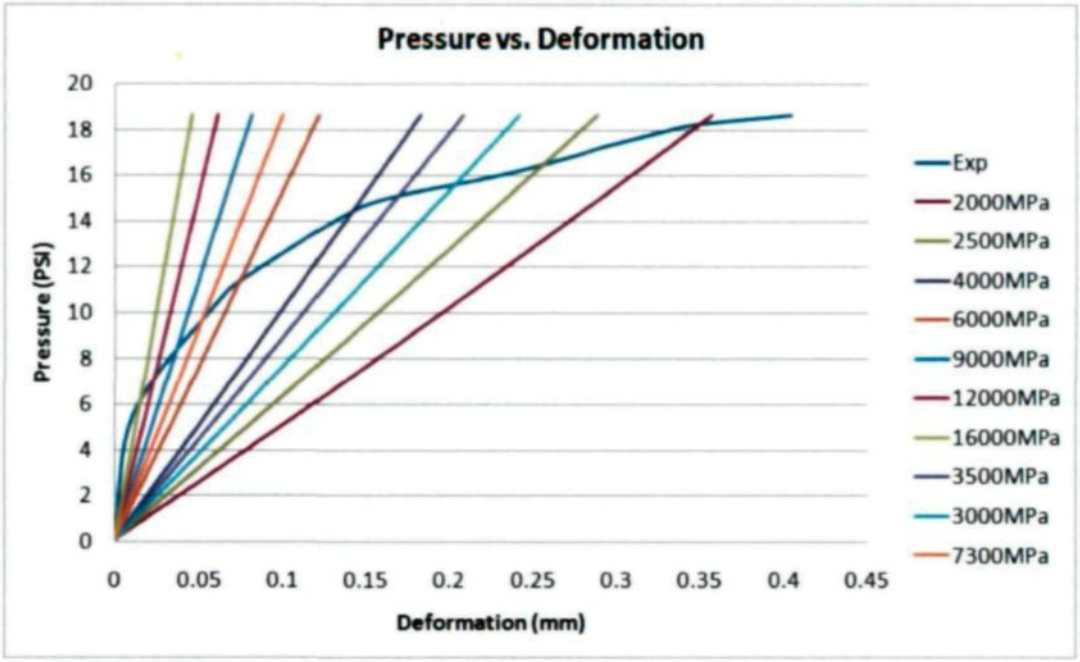

Figure 4-18 - Hyperelastic simulations for WPC60wt% at -50°C

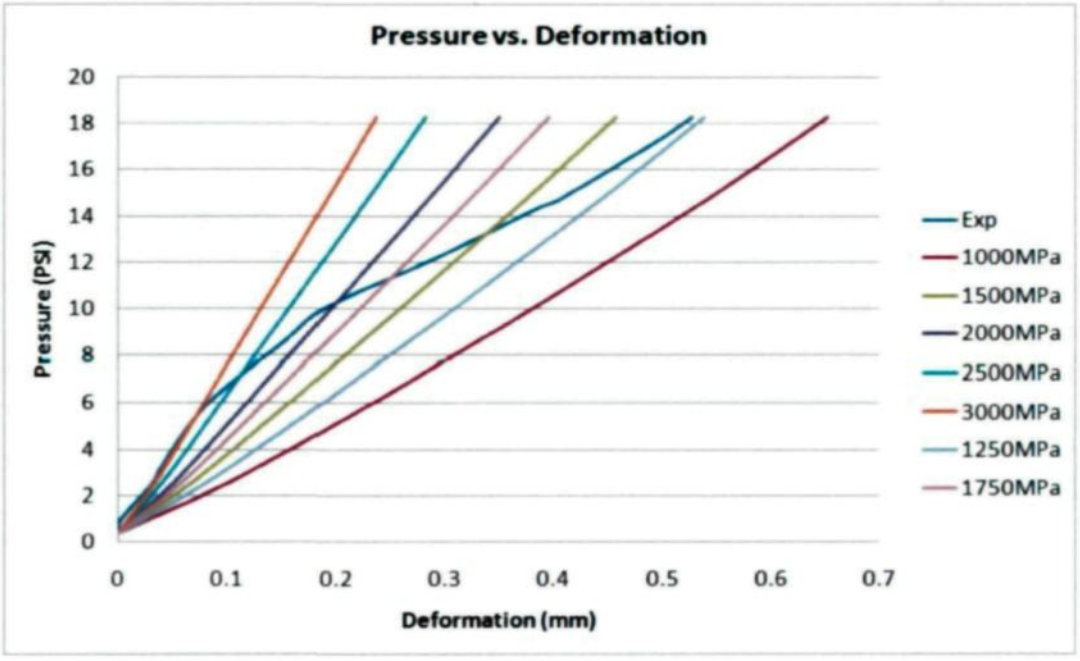

Figure 4-19 - Hyperelastic simulations for WPC60wt% at 0°C

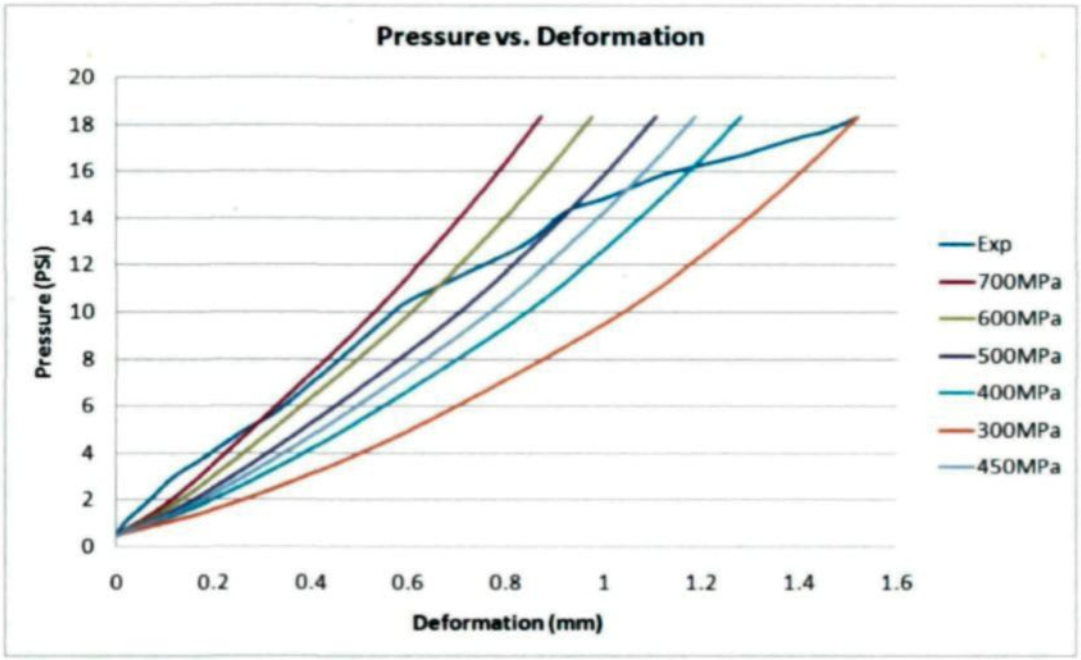

Figure 4-20 - Hyperelastic simulations for WPC60wt% at 50°C

Each of the above graphs represents a specific type of membrane at a specific temperature. For example, for WPC60wt% at 50°C, the experimental results and the results from six simulations are shown in Figure 4-20. Each of the eight hyperelastic simulations corresponds to a specific value of the material constant. The material constant in this case is the C_1 values in the neo-Hookean model.

Following the computer simulations using Abaqus, the next step is to obtain the optimum values for the material constants using the neural network in the next chapter.

4.6 Principal stresses

In order to better understand the stress distribution in the membranes under pressure, the maximum and minimum values of von Mises stresses are obtained in Abaqus. The stresses are reported for both elastic and hyperelastic models in Tables 4-1 to 4-3 for HDPE and WPC samples at three different temperatures. The maximum stress occurs on the edge of the membrane that is clamped to the experimental setup and the minimum stress is in the pole of the inflated membrane. The simplified von Mises equation is (Popov, 1976):

$$\sigma_v = \sqrt{\frac{1}{2}[(\sigma_{11} - \sigma_{22})^2 + (\sigma_{22} - \sigma_{33})^2 + (\sigma_{33} - \sigma_{11})^2 + 6(\sigma_{12}^2 + \sigma_{23}^2 + \sigma_{31}^2)]} \quad (4\text{-}2)$$

The stresses are calculated at the final step of the blowing, where the bubble has the maximum height.

Table 4-1 – Max and min values of von Mises stresses for inflated HDPE membrane at max babble height

	Elastic		Hyperelastic	
Temperature	Min (Pa)	Max (Pa)	Min (Pa)	Max (Pa)
−50°C	8.783E6	2.635E7	8.214E6	2.464E7
0°C	6.270E6	2.508E7	5.810E6	2.324E7
50°C	5.739E6	2.295E7	5.656E6	2.263E7

Table 4-2 - Max and min values of von Mises stresses for inflated WPC30% membrane at max babble height

	Elastic		Hyperelastic	
Temperature	Min (Pa)	Max (Pa)	Min (Pa)	Max (Pa)
−50°C	9.968E6	2.990E7	9.577E6	2.873E7
0°C	9.762E6	2.928E7	9.298E6	2.789E7
50°C	8.917E6	2.675E7	8.165E6	2.449E7

Table 4-3 - Max and min values of von Mises stresses for inflated WPC60% membrane at max babble height

	Elastic		Hyperelastic	
Temperature	Min (Pa)	Max (Pa)	Min (Pa)	Max (Pa)
−50°C	2.072E7	3.108E7	1.984E7	2.977E7
0°C	2.028E7	3.042E7	1.950E7	2.925E7
50°C	1.644E7	2.818E7	1.603E7	2.748E7

4.7 Conclusion

In this chapter, Abaqus was used in order to model the elastic and hyperelastic behaviour of the specimens. Three classes of material were selected: HDPE and WPCs with 30 and 60wt% of wood fibre and the simulations were carried out at three different temperatures: $-50°C, 0°C,$ and $50°C$.

For each class of material at each temperature a minimum number of six simulations were carried out. Each simulation corresponds to a specific value of material constant. The material constants are Young's modulus (E) and C_1 for elastic and hyperelastic models, respectively.

The results of this chapter will be used in the following chapter in order to obtain the optimum material constants using the Artificial Neural Networks.

CHAPTER 5

NEURAL NETWORKS APPLICATION

5.1 Introduction

This chapter starts with a detailed study of the neural networks. Furthermore, their application in this project is investigated in order to find the optimum material constants.

Finally, the material requirements for the rotorblades industry are compared with the ones obtained in this project and the final material selection is performed.

5.2 Neural networks versus conventional computers

Neural networks take a different approach to problem solving than that of conventional computers. Conventional computers use an algorithmic approach. Unless the specific steps that the computer needs to follow are known, the computer cannot solve the problem. This restricts the problem solving capability of conventional computers to problems that are already understood and have been solved.

Neural networks process information in a similar way to the human brain. The network is composed of a large number of highly interconnected processing elements working in parallel to solve a specific problem. Neural networks learn by example. They

cannot be programmed to perform a specific task. The examples must be selected carefully otherwise useful time is wasted or even worse the network might be functioning incorrectly. The disadvantage is that, because the network finds out how to solve the problem by itself, its operation can be unpredictable.

On the other hand, conventional computers use a cognitive approach to problem solving. The way the problem is solved must be known and stated in small unambiguous instructions. These instructions are then converted to a high-level program language and then into machine code that the computer can understand. These machines are entirely predictable and if anything goes wrong, it is due to a software or hardware fault (Stergiou & Siganos, 1996).

Neural networks and conventional algorithmic computers are not in competition, but complement each other. Some tasks are more suited to an algorithmic approach, such as arithmetic operations, and some are more suited to neural networks. However, a large number of tasks require systems that use a combination of the two approaches in order to perform at maximum efficiency.

5.3 Human and artificial neurons

Much is still unknown about how the brain trains itself to process information. In the human brain, a typical neuron collects signals from others through a host of fine structures called dendrites. The neuron sends out spikes of electrical activity through a

long, thin stand known as an axon, which splits into thousands of branches. At the end of each branch, a structure called a synapse converts the activity from the axon into electrical effects that inhibit or excite activity in the adjacent neurons. When a neuron receives excitatory input above a threshold level, it propagates electrical activity along its axon. Learning occurs by changing the effectiveness of the synapses, so that the influence of one neuron on another changes (Stergiou & Siganos, 1996). Figures 5-1 and 5-2 show components of a neuron and the synapse between two neurons.

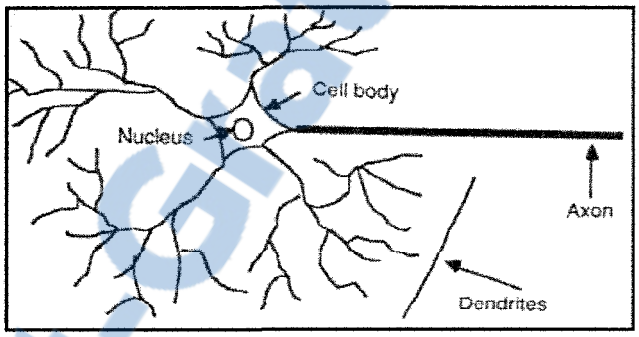

Figure 5-1 - Components of a neuron (Stergiou & Siganos, 1996)

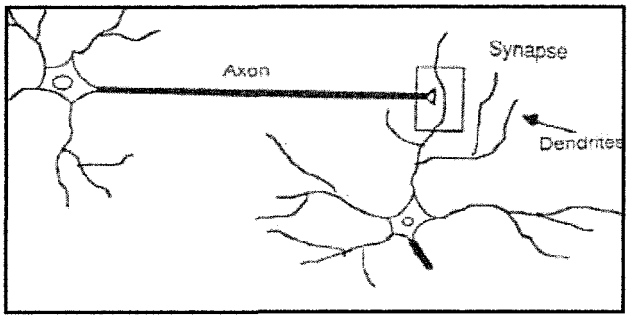

Figure 5-2 - The synapse (Stergiou & Siganos, 1996)

The neural networks are conducted by first trying to deduce the essential features of neurones and their interconnections. Then a computer program is used to simulate these features. However, since the knowledge of neurons is incomplete and the computing power is limited, the models are necessarily gross idealisations of real networks of neurons. Figure 5-3 illustrates a neuron model.

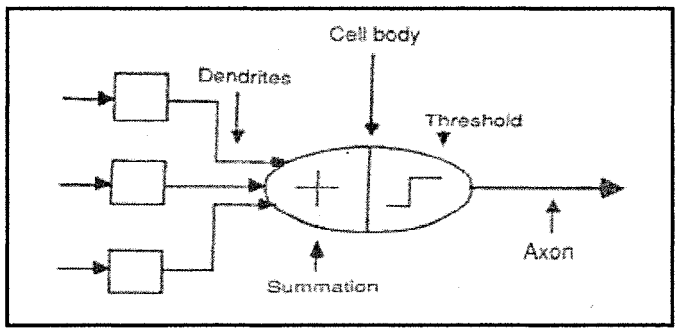

Figure 5-3 - The neuron model (Stergiou & Siganos, 1996)

5.4 Engineering approach

5.4.1 A simple neuron

An Artificial Neural Network is a device with many inputs and one output. The neuron has two operation modes; the training mode and the service mode. In the training mode, the neuron can be trained to fire for particular input patterns. In the service mode, when a taught input pattern is detected at the input, its associated output becomes the current output. When the input pattern does not exist in the taught list of input patterns, the firing rule is used to determine whether to fire or not (Stergiou & Siganos, 1996). Figure 5-4 shows a simple neuron.

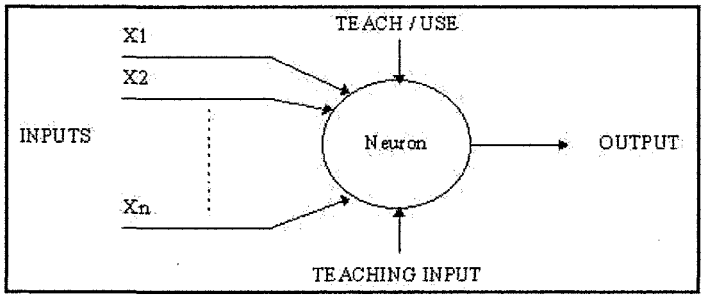

Figure 5-4 - A simple neuron (Stergiou & Siganos, 1996)

5.4.2 Firing rules

The firing rule is an important concept in neural networks and accounts for their high flexibility. A firing rule determines how one calculates whether a neuron should fire for a given input pattern. It relates to all the input patterns, and not only the ones on which the node was trained.

A simple firing rule can be implemented by using Hamming distance technique. The rule goes as follows: take a collection of training patterns for a node, some of which cause it to fire (the 1-taught set of patterns) and others which prevent it from doing so (the 0-taught set). Then, the patterns not in the collection cause the node to fire if, on comparison, they have more input elements in common with the nearest pattern in the 1-taught set than with the nearest pattern in the 0-taught set. If there is a tie, then the pattern remains in the undefined state (Aleksander & Morton, 1995).

For example, a 3-input neuron is taught to output 1 when the input (X1,X2, and X3) is 111 or 101 and to output 0 when the input is 000 or 001 as shown in Table 5-1. Then, before applying the firing rule, the truth table is:

Table 5-1 – A sample truth table

X1	0	0	0	0	1	1	1	1
X1	0	0	1	1	0	0	1	1
X3	0	1	0	1	0	1	0	1
Output	0	0	0/1	0/1	0/1	1	0/1	1

As an example of the way the firing rule is applied, pattern 010 can be used. It differs from 000 in 1 element, from 001 in 2 elements, from 101 in 3 elements and from 111 in 2 elements. Therefore, the nearest pattern is 000 that belongs in the 0-taught set. Thus the firing rule requires that the neuron should not fire when the input is 001. On the other hand, 011 is equally distant from two taught patterns that have different outputs and thus the output stays undefined. By applying the firing rule in every column Table 5-2 is obtained:

Table 5-2 - Truth table after applying firing rule

X1	0	0	0	0	1	1	1	1
X1	0	0	1	1	0	0	1	1
X3	0	1	0	1	0	1	0	1
Output	0	0	0	0/1	0/1	1	1	1

The difference between the two truth tables is called the generalisation of the neurons. Therefore, the firing rule gives the neuron a sense of similarity and enables it to respond sensibly to patterns not seen during training.

A more sophisticated neuron is the McCulloch and Pitts model (MCP) (Aleksander & Morton, 1995). The difference from the previous model is that the inputs are weighted. The effect that each input has on decision making is dependent on the weight of the particular input. The weight of an input is a number, which when multiplied with the input, gives the weighted input. The weighted inputs are then added together and if they exceed a pre-set threshold value, the neuron fires. In any other case the neuron does not fire. Figure 5-5 illustrates an MCP neuron.

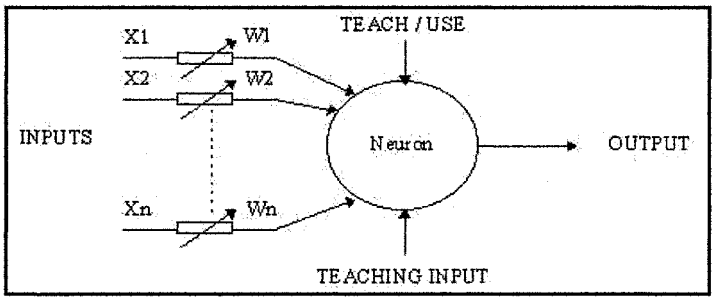

Figure 5-5 - An MCP neuron (Aleksander & Morton, 1995)

In mathematical terms, the neuron fires if and only if:

$$X_1W_1 + X_2W_2 + X_3W_3 + \cdots > T \qquad (5\text{-}1)$$

The addition of input weights and of the threshold makes this neuron a very flexible and powerful one. The MCP neuron has the ability to adapt to a particular situation by changing its weights and/or threshold. Various algorithms exist that cause the neuron to adapt. The most common ones are Delta rule and the back error propagation. The former is used in feed-forward networks and the latter in feedback networks (Aleksander & Morton, 1995).

5.5 Architecture of neural networks

5.5.1 Feed-forward networks

Feed-forward ANNs allow signals to travel one way only from input to output. There is no feedback loops and the output of any layer does not affect that same layer. Feed-forward ANNs tend to be straight forward networks that associate inputs with outputs. They are extensively used in pattern recognition. This type of organisation is also referred to as bottom-up or top-down (Figure 5-6).

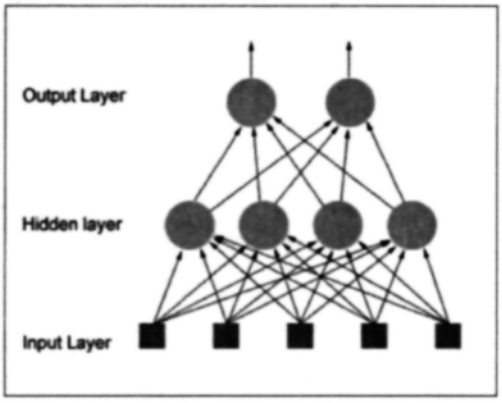

Figure 5-6 - Simple feed-forward network (Aleksander & Morton, 1995)

5.5.2 Feedback networks

Feedback networks can have signals travelling in both directions by using loops in the network (Figure 5-7). Feedback networks are known to be very powerful and can get extremely complicated. Feedback networks are dynamic and until they reach an equilibrium point their state is continuously changing. They remain at the equilibrium point until the input changes and a new equilibrium needs to be found. Feedback architectures are also referred to as interactive or recurrent, although the latter term is often used to denote feedback connections in single-layer organisations (Stergiou & Siganos, 1996).

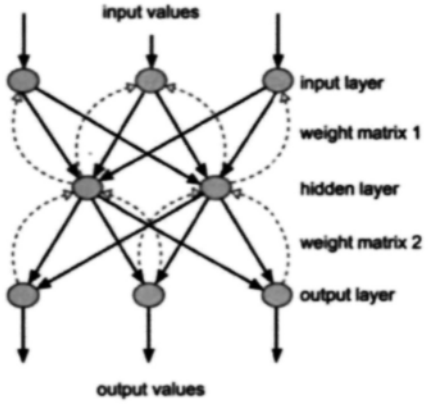

Figure 5-7 - Feedback network

5.5.3 Network layers

The most common type of artificial neural network consists of three layers: a layer of input units that is connected to a layer of hidden units, which is connected to a layer of output units.

The activity of the input units represents the raw information that is fed into the network. The activity of each hidden unit is determined by the activity of the input units and weights on the connections between the input and hidden units. The behaviour of the output units depends on the activity of the hidden units and the weights between the hidden and output units.

This type of network is interesting since the hidden units are free to construct their own representations of the unit. The weights between the input and hidden units determine when each hidden unit is active. Therefore, by modifying these weights a hidden unit can choose what it represents (Stergiou & Siganos, 1996).

5.5.4 Perceptrons

The most influential work on neural networks in the 60's was carried out under the heading of perceptrons, a term used by Frank Rosenblatt (Stergiou & Siganos, 1996). The perceptron is an MCP model with some additional, fixed, pre-processing. Units called association units are to extract specific, localised features from the input images. Perceptrons mimic the basic idea behind the mammalian visual system. They were mainly used in pattern recognition even though their capabilities extended a lot further.

5.6 The learning process

The memorisation of patterns and the subsequent response of the network can be categorised into two general paradigms: associative mapping and regularity detection.

In associative mapping, the network learns to produce a particular pattern from a set of input units whenever another particular pattern is applied as a set of input units. The associative mapping can generally be broken down into two mechanisms (Aleksander & Morton, 1995):

- **Auto-association:** in this mechanism an input pattern is associated with itself and the states of input and output units coincide. This is generally used to provide pattern completion, for example to produce a pattern when a portion of it is presented.
- **Hetero-association:** this mechanism is related to two recall mechanisms; nearest-neighbour recall, and interpolative recall. In nearest-neighbour recall the produced output pattern corresponds to the input pattern stored, which is closest to the pattern presented. In interpolative recall the produced output pattern is a similarity dependent interpolation of the patterns stored, corresponding to the pattern presented.

In regulatory detection, units learn to respond to particular properties of the input pattern; whereas, in associative mapping the network stores the relationships among patterns. In regulatory detection the response of each unit has a particular meaning. This type of learning mechanism is essential for feature discovery and knowledge representation (Stergiou & Siganos, 1996).

A neural network processes the knowledge, which is contained in the values of the connection weights. Modifying the knowledge stored in the networks as a function of experience implies a learning rule for changing the value of the weights.

Information is stored in the weight matrix, W, of a neural network. Learning process determines the value of the weights. Based on the learning process, there are two categories of neural networks (Stergiou & Siganos, 1996):

- Fixed networks: the weights cannot be changed and the weights are fixed in order to solve a specific problem.
- Adaptive networks: the weights can be changed by the network itself.

All learning methods used for adaptive neural networks can be classified into two major categories: supervised learning and unsupervised learning (Aleksander & Morton, 1995).

Supervised learning incorporates an external teacher, so that each output unit is told what its desired response to input signals should be. Global information may be required during the learning process. Paradigms of supervised learning include error-correction learning, reinforcement learning, and stochastic learning.

Concerning supervised learning, an important issue is the problem of error convergence. The aim is to determine a set of weights that minimises the error. One well-

known method is the least mean squares (LMS) convergence that is common to many learning paradigms.

Unsupervised learning uses no external teacher and is only based on local information. It is also referred to as self-organisation, since it self-organises data presented to the network and detects their emergent collective properties.

5.6.1 Transfer function

The behaviour of an ANN depends on both, the weights and the input-output function, which is specified for the units. This function typically falls into one of three categories (Stergiou & Siganos, 1996):

- Linear units: the output activity is proportional to the total weighted output.
- Threshold units: the output is set at one of two levels, depending on whether the total input is greater than or less than some threshold values.
- Sigmoid units: the output varies continuously but not linearly as the input changes. Sigmoid units bear a greater resemblance to real neurons than do linear or threshold units.

To make a neural network that performs a specific task, the way that the units are connected must be chosen and the appropriate weights on the connections must be set. The connections determine whether it is possible for one unit to influence another. The weights specify the strength of the influence.

The following procedure can be used to teach a three-layer network to perform a particular task (Stergiou & Siganos, 1996):

- The network is presented with training examples that consist of a pattern of activities for the input units together with the desired pattern of activities for the output units.
- The output is compared with the desired output in order to determine how close they are.
- The weight of each connection is changed so that the network produces a better approximation of the desired output.

5.6.2 The back propagation algorithm

In order to train a neural network to perform a specific task, the weights of each unit must be adjusted in such a way that the error between the desired output and the actual output is reduced. This process requires that the neural network compute the error derivative of the weights (EW). In fact, it must calculate the error changes as each weight is increased or decreased slightly. The back propagation algorithm is the most widely used for determining the error derivative of the weights (Aleksander & Morton, 1995).

The algorithm computes each EW by first computing the EA, the rate at which the error changes as the activity level of a unit is changed. For output units, the EA is simply the difference between the actual and the desired output. To compute the EA for a hidden unit in the layer just before the output layer, first all the weights between that hidden unit

and the output units to which it is connected must be identified. Then, those weights are multiplied by the EAs of those output units and are added to the products. This sum equals the EA for the chosen hidden unit. After calculating all the EAs in the hidden layer just before the output layer, the EAs for other layers are calculated in the same way moving from layer to layer in a direction opposite to the way activities propagate through the network. Once the EA has been computed for a unit, it is straight forward to compute the EW for each incoming connection of the unit. The EW is the product of the EA and the activity through the incoming connection.

5.7 Artificial Neural Networks application

In this project, in order to address the problem of material identification, a supervised learning neural network is used. The architecture selected is the Multilayer Perceptron with back-propagation of error. A sigmoid function is used as the transfer function of the neurons in the hidden layer.

This choice is justified by the properties of this function to adapt to more general problems. The ID function is used as the transfer function of the neurons in the output layer.

Although the neural networks toolbox is available in Matlab, for the purpose of this project, the neural network code was developed in order to obtain more accurate results.

The optimum material constants for elastic and hyperelastic models are obtained using the neural network. The results from the simulations are used to generate the required matrices to train the neural network.

For each class of material at each temperature a 8×6 matrix is used to train the neural network. The matrices consist of deformation values obtained in Abaqus using six different values for material constants. In other words, each column of a matrix refers to deformation values that were generated by simulations for each material constant. A 1×6 matrix is also prepared that contains the values of material constants. The material constants in this project correspond to Young's modulus and C_1 for elastic and hyperelastic models, respectively.

After introducing the experimental results to the neural network, the output matrix represents the optimum material constant. The hidden layers of the network are formed by two successive layers and each layer compromises 30 neurons.

Figures 5-8 to 5-25 show the experimental results (dotted line) and the optimum graph (solid line) that corresponds to the optimum material constant for elastic and hyperelastic models.

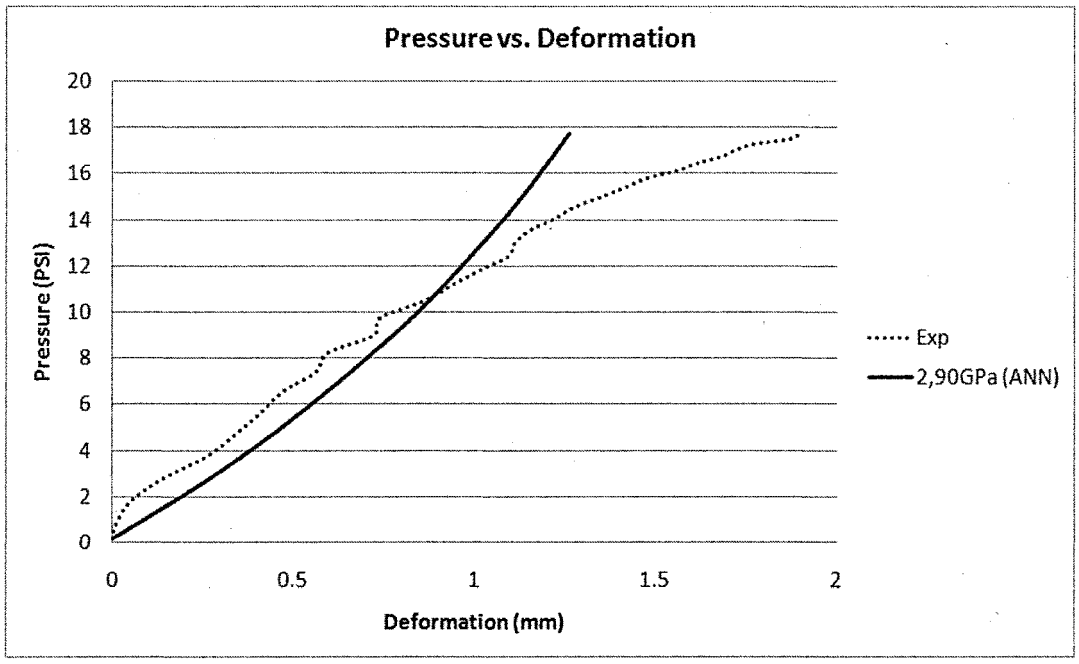

Figure 5-8 - Experimental and ANN results for the elastic model of HDPE at -50°C

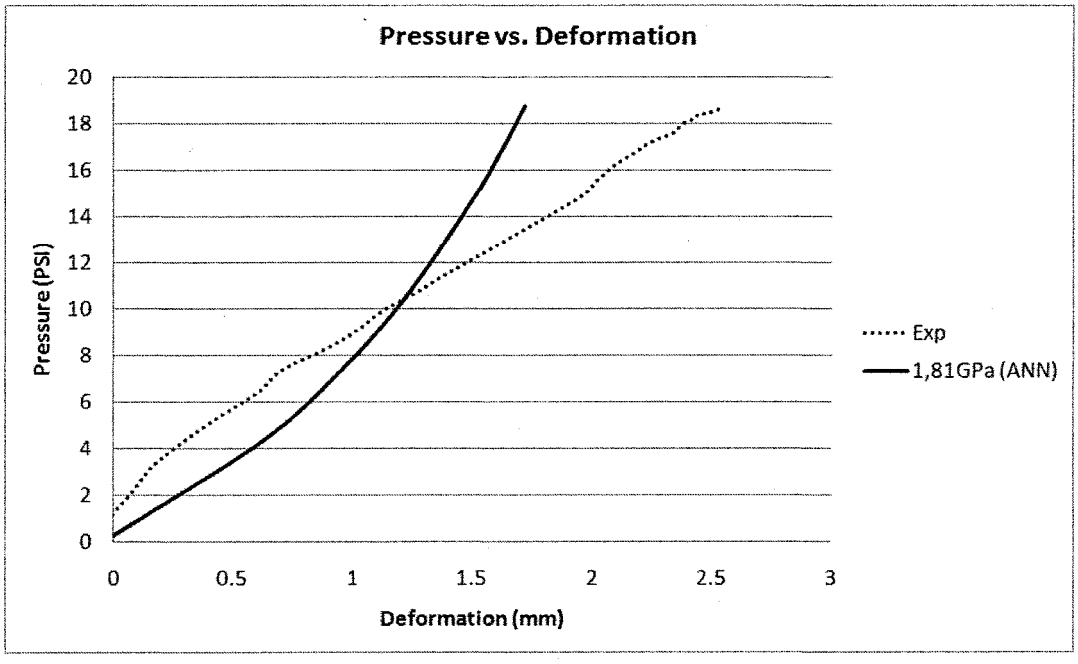

Figure 5-9 - Experimental and ANN results for the elastic model of HDPE at 0°C

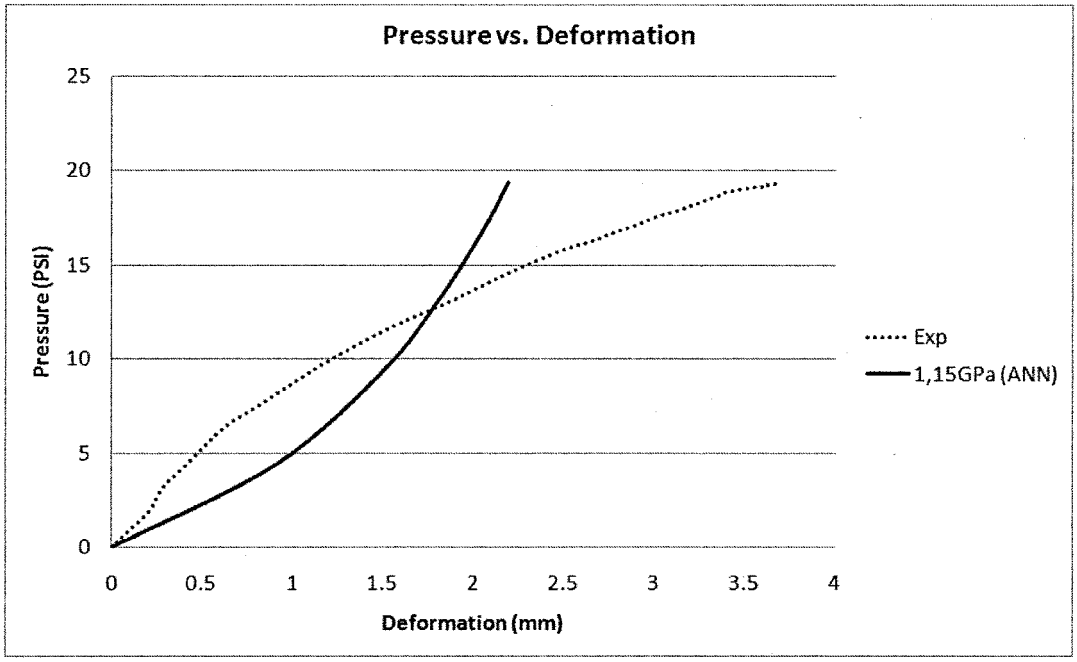

Figure 5-10 - Experimental and ANN results for the elastic model of HDPE at 50°C

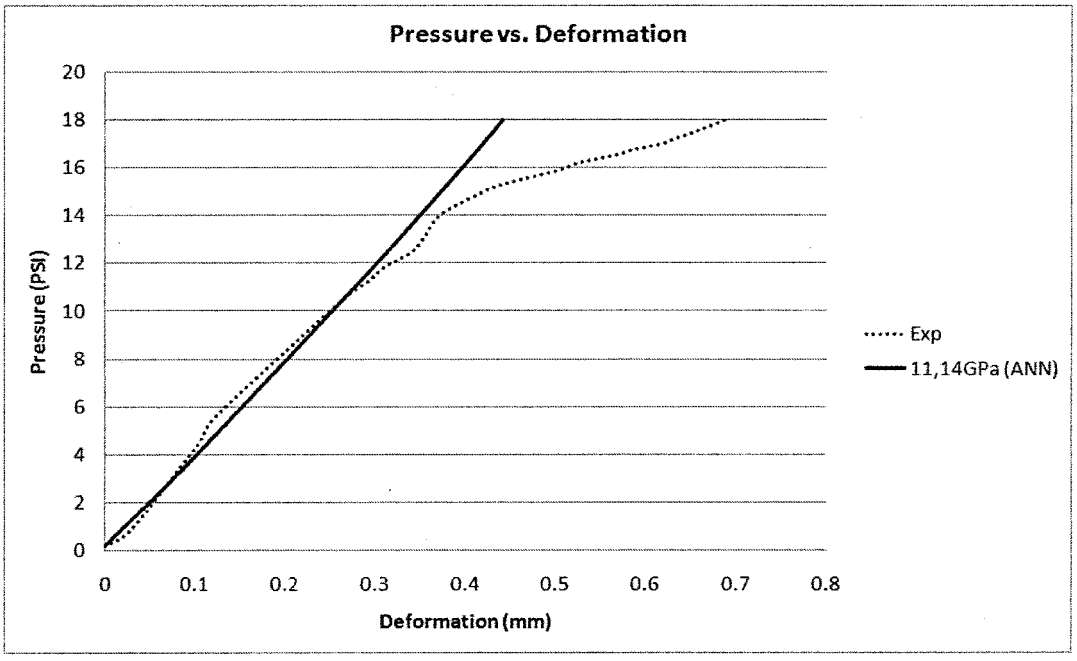

Figure 5-11 - Experimental and ANN results for the elastic model of WPC30wt% at -50°C

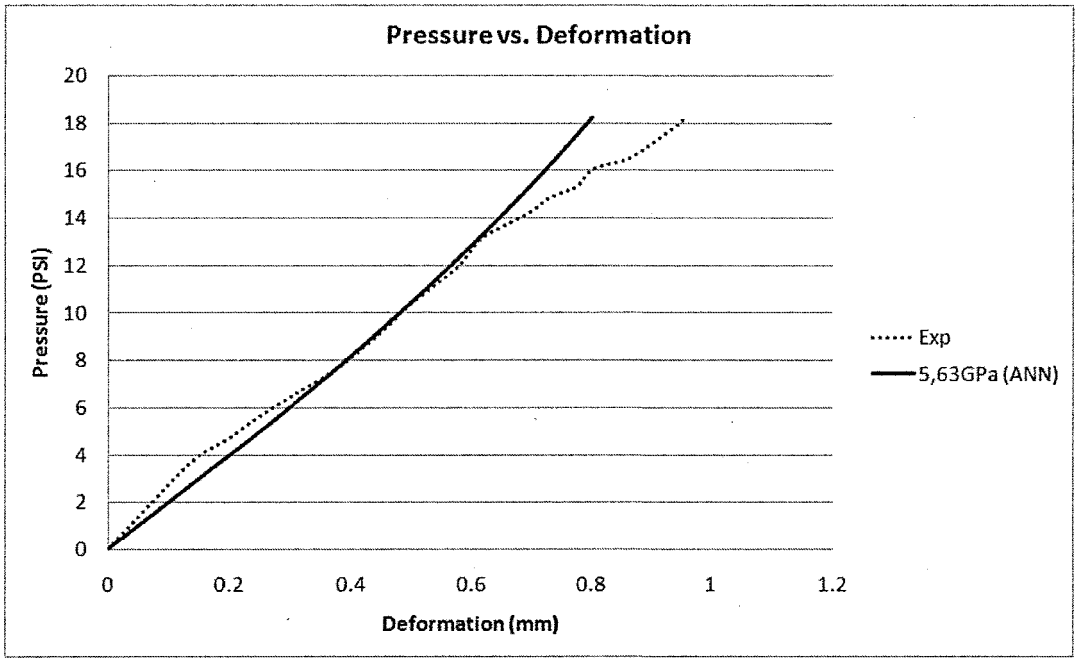

Figure 5-12 - Experimental and ANN results for the elastic model of WPC30wt% at 0°C

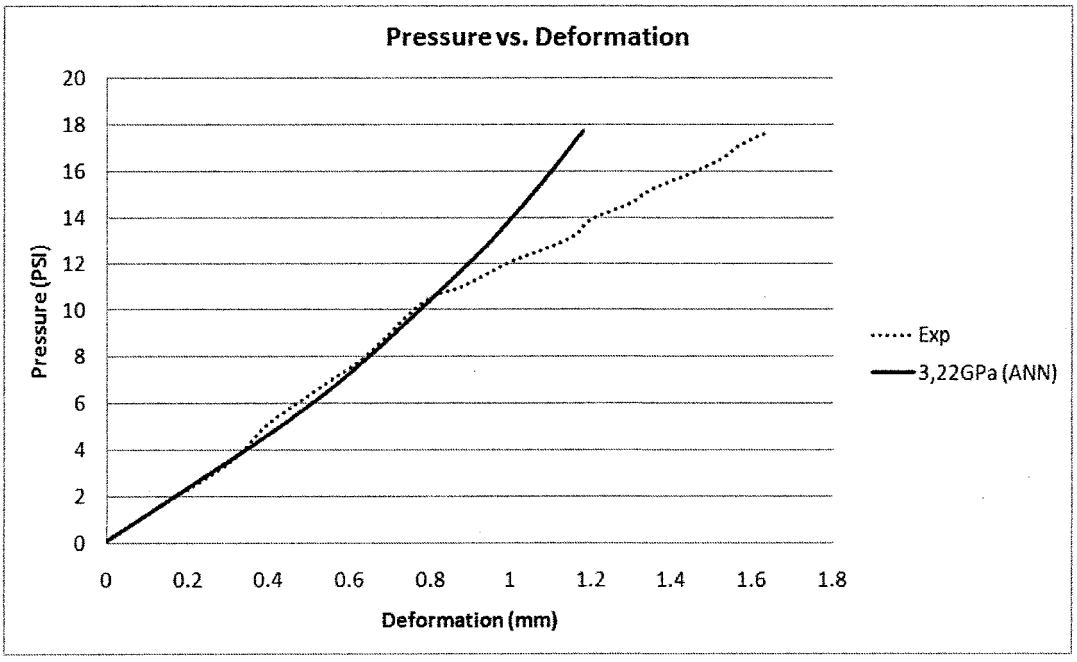

Figure 5-13 - Experimental and ANN results for the elastic model of WPC30wt% at 50°C

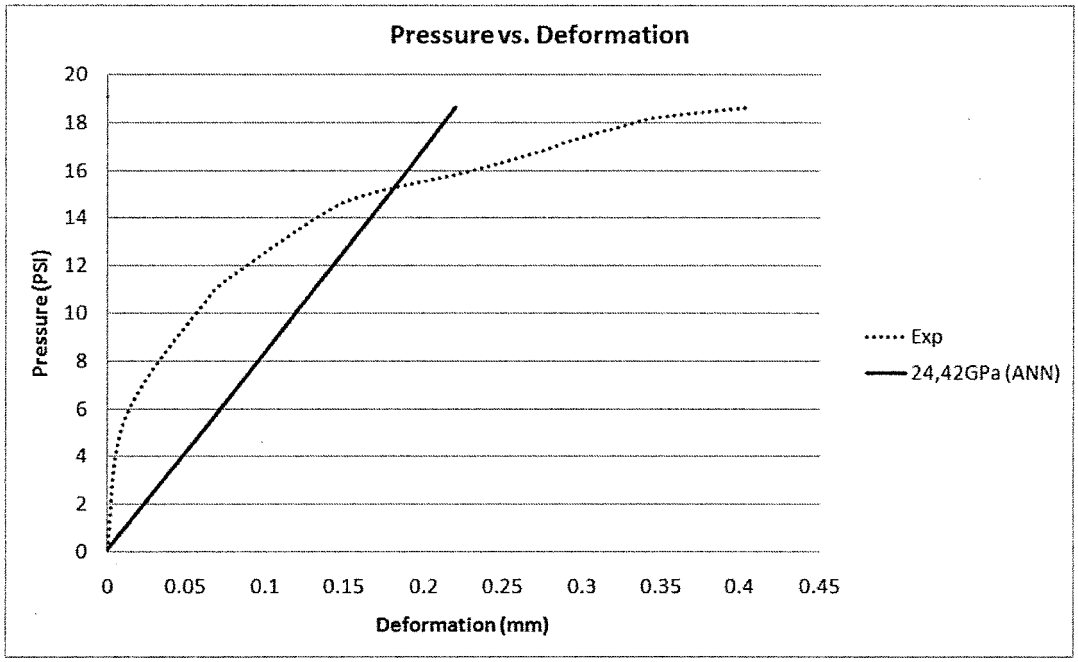

Figure 5-14 - Experimental and ANN results for the elastic model of WPC60wt% at -50°C

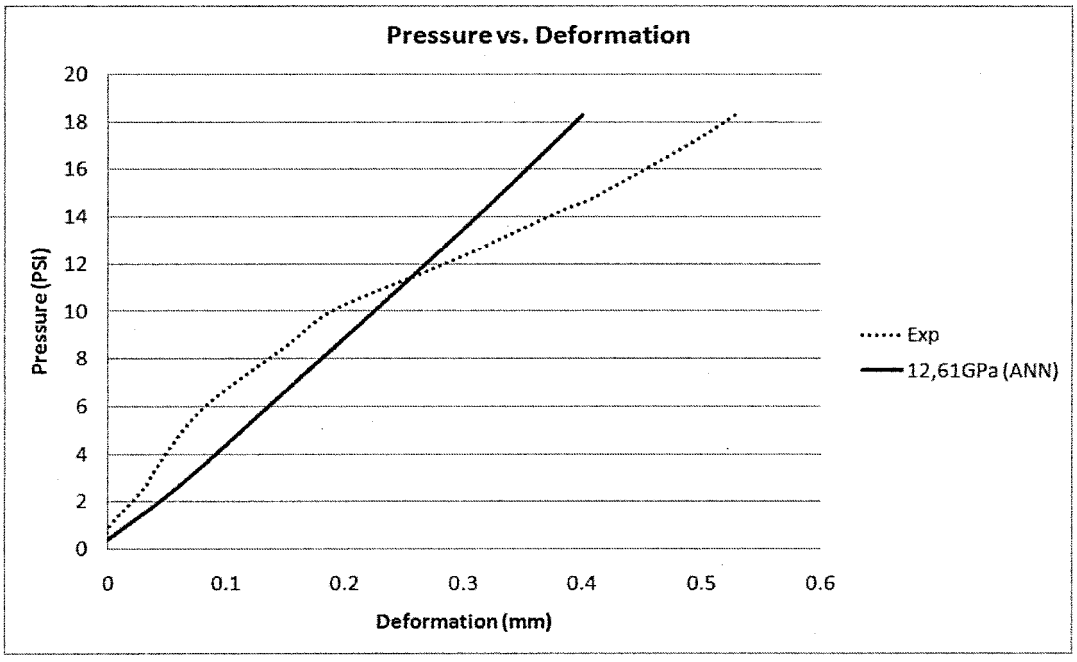

Figure 5-15 - Experimental and ANN results for the elastic model of WPC60wt% at 0°C

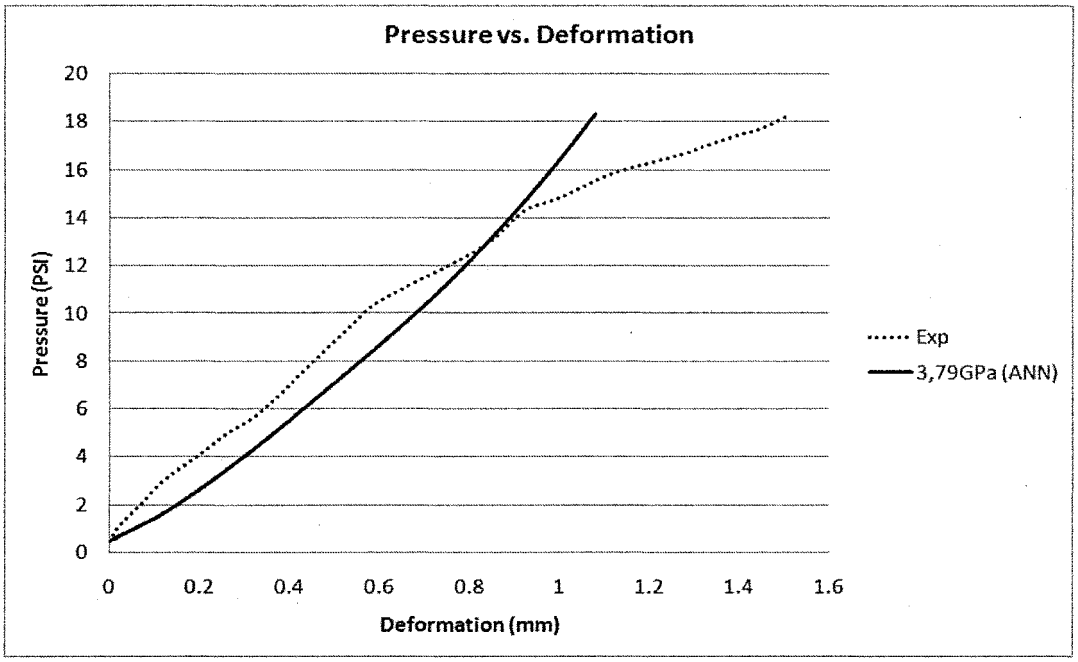

Figure 5-16 - Experimental and ANN results for the elastic model of WPC60wt% at 50°C

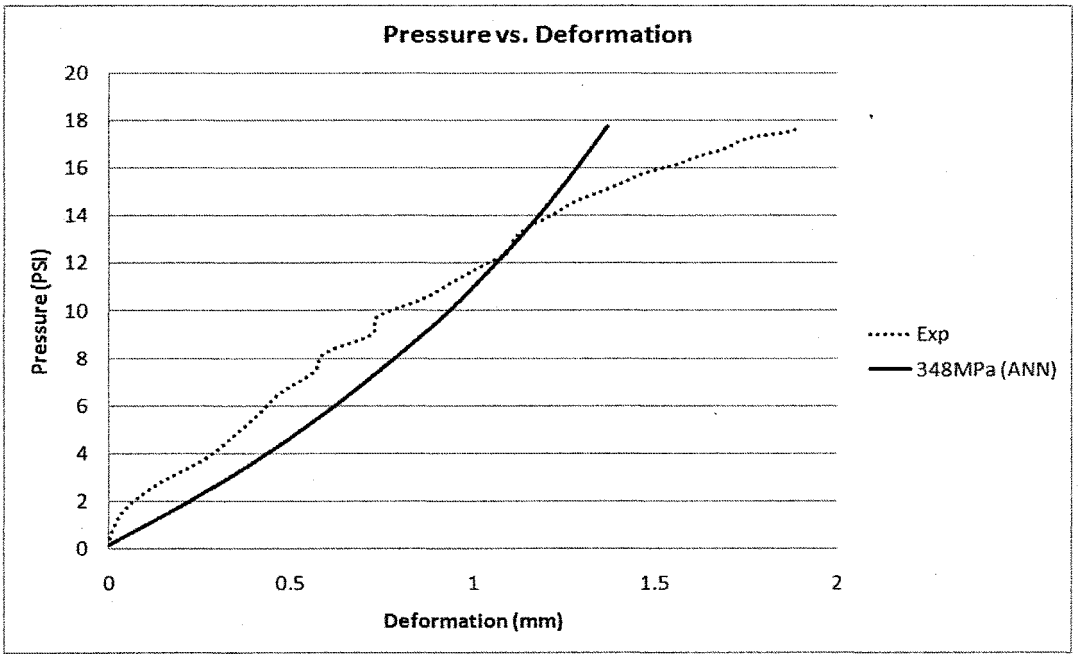

Figure 5-17 - Experimental and ANN results for the hyperelastic model of HDPE at -50°C

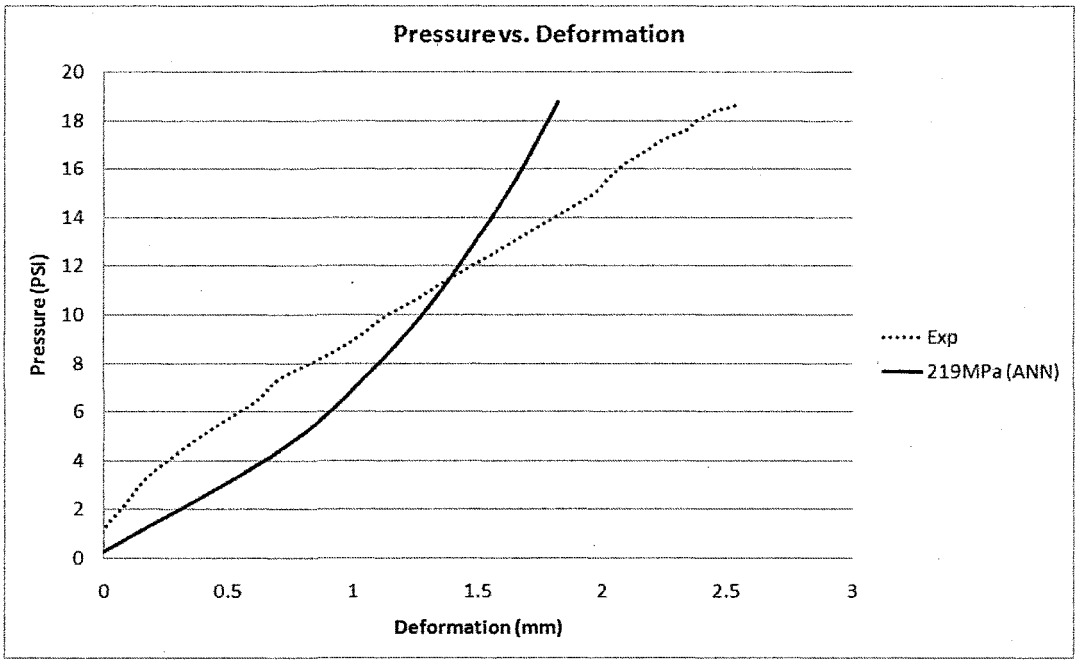

Figure 5-18 - Experimental and ANN results for the hyperelastic model of HDPE at 0°C

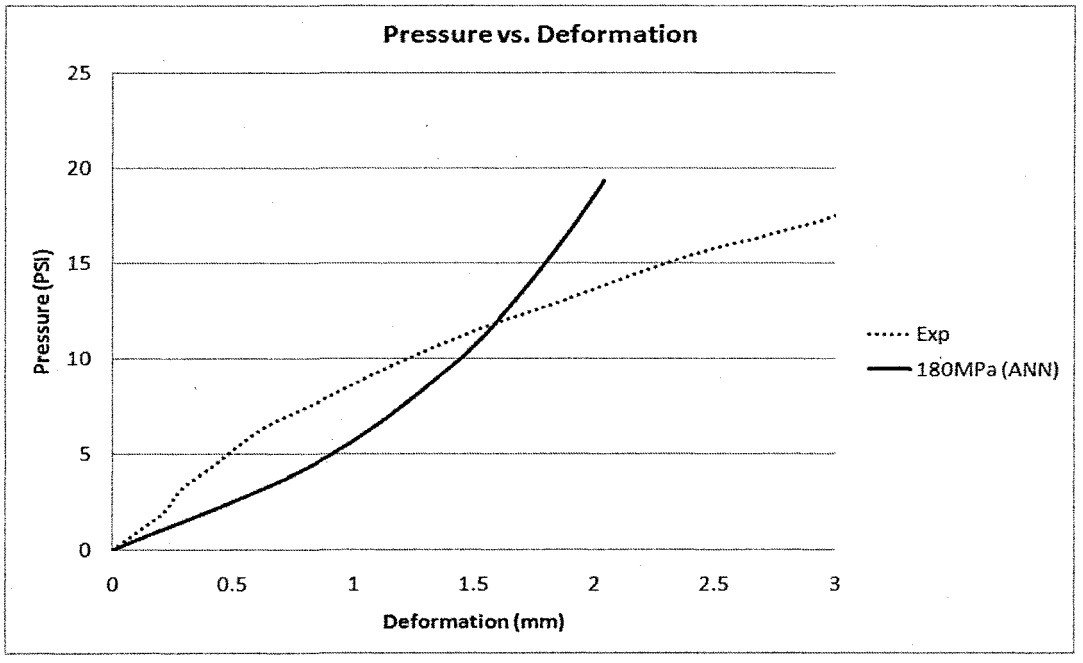

Figure 5-19 - Experimental and ANN results for the hyperelastic model of HDPE at 50°C

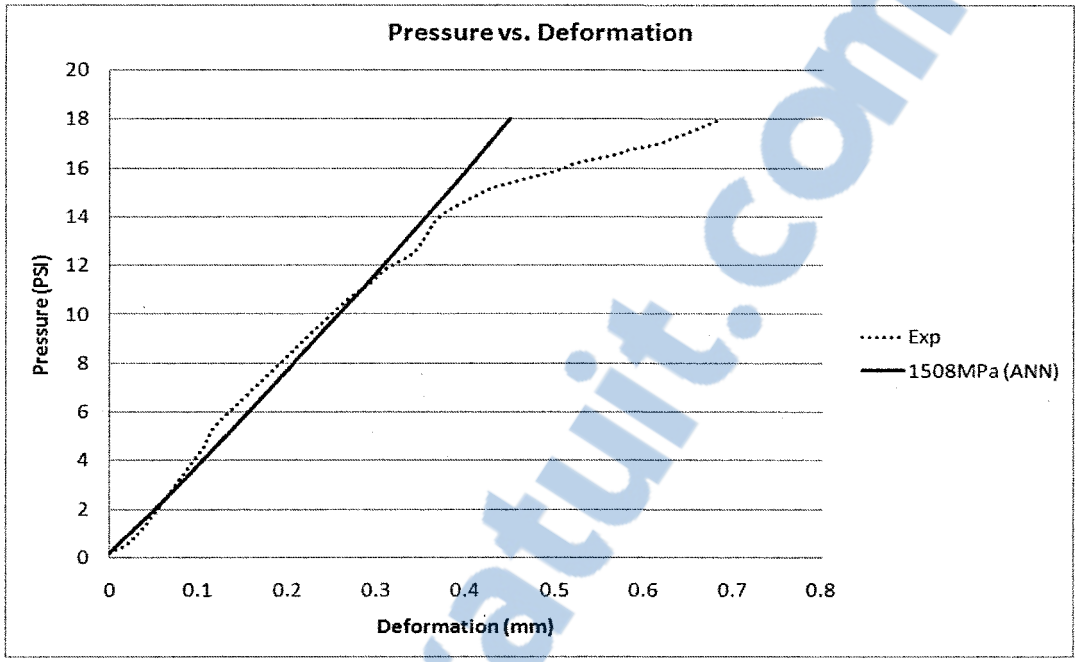

Figure 5-20 - Experimental and ANN results for the hyperelastic model of WPC30wt% at -50°C

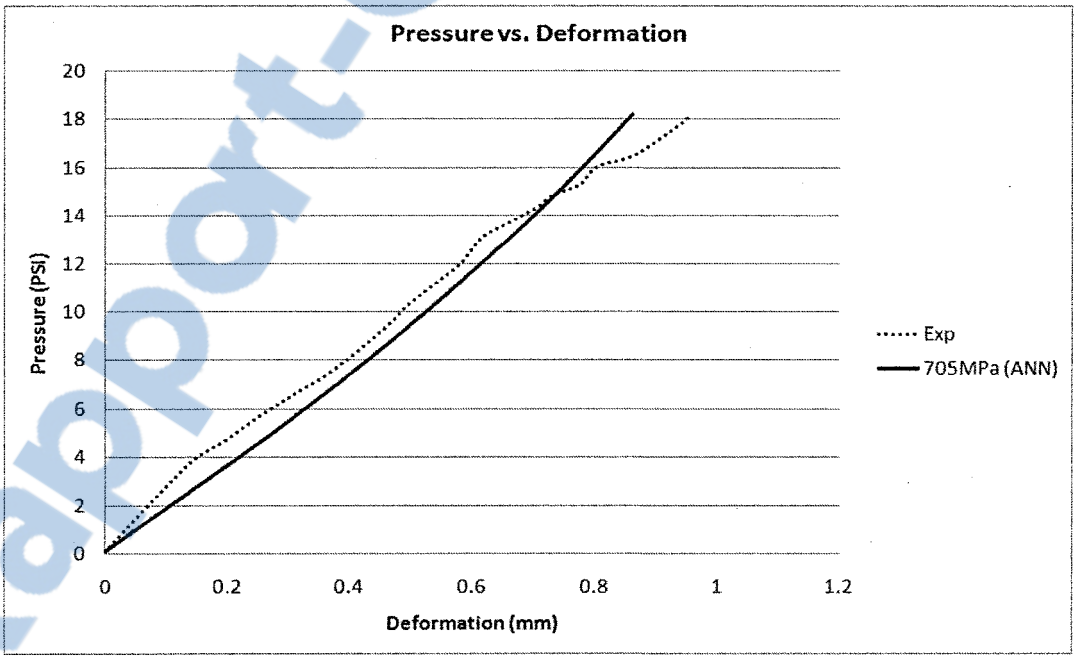

Figure 5-21 - Experimental and ANN results for the hyperelastic model of WPC30wt% at 0°C

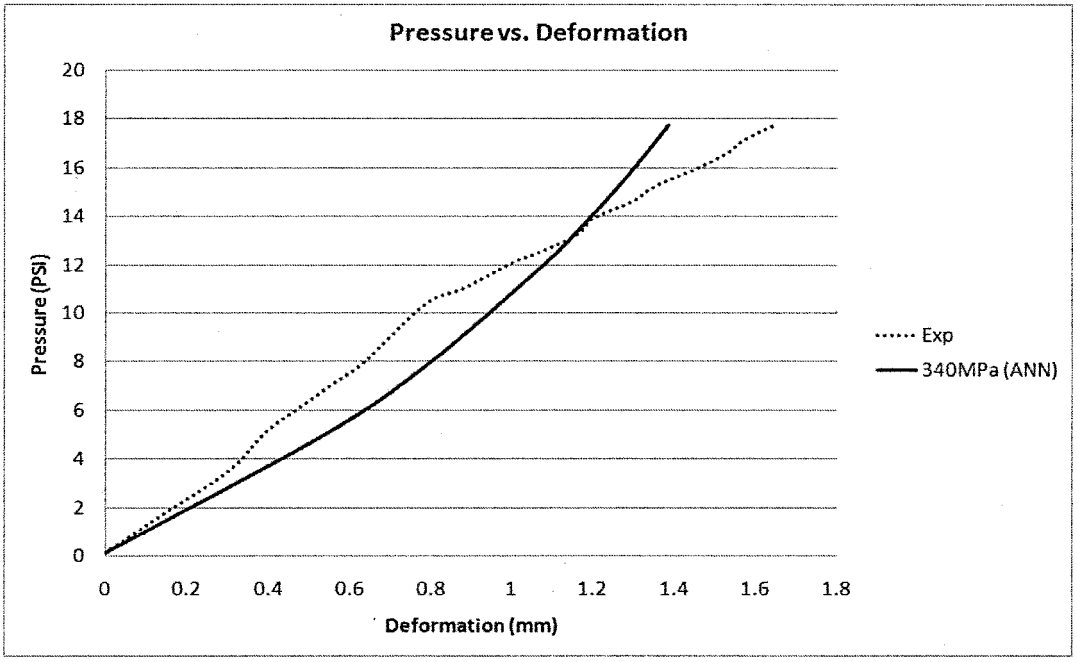

Figure 5-22 - Experimental and ANN results for the hyperelastic model of WPC30wt% at 50°C

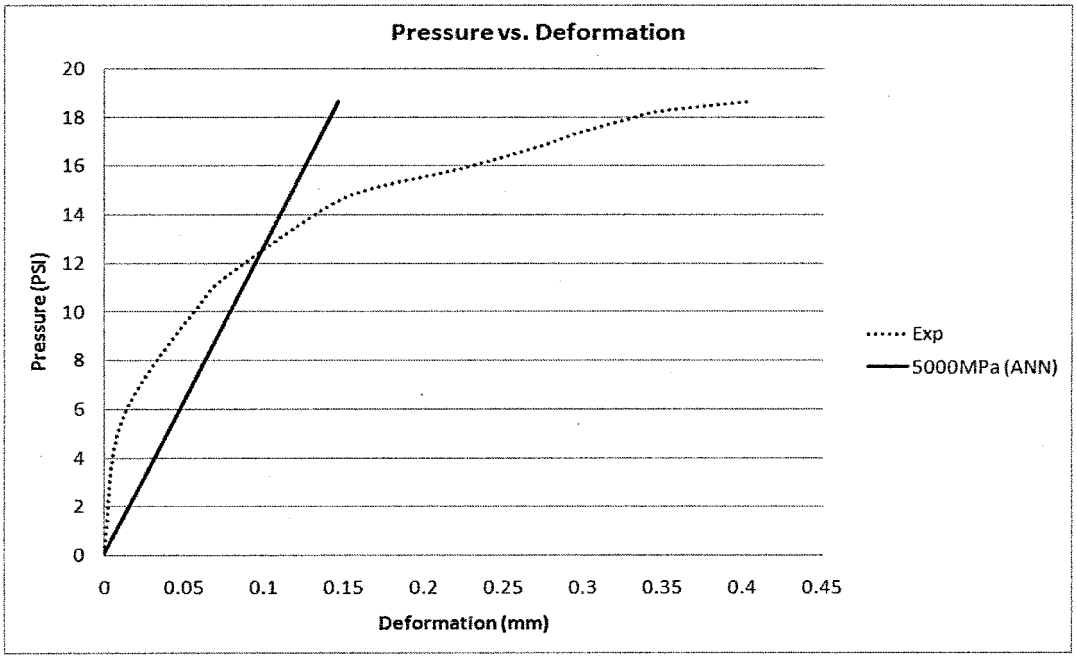

Figure 5-23 - Experimental and ANN results for the hyperelastic model of WPC60wt% at -50°C

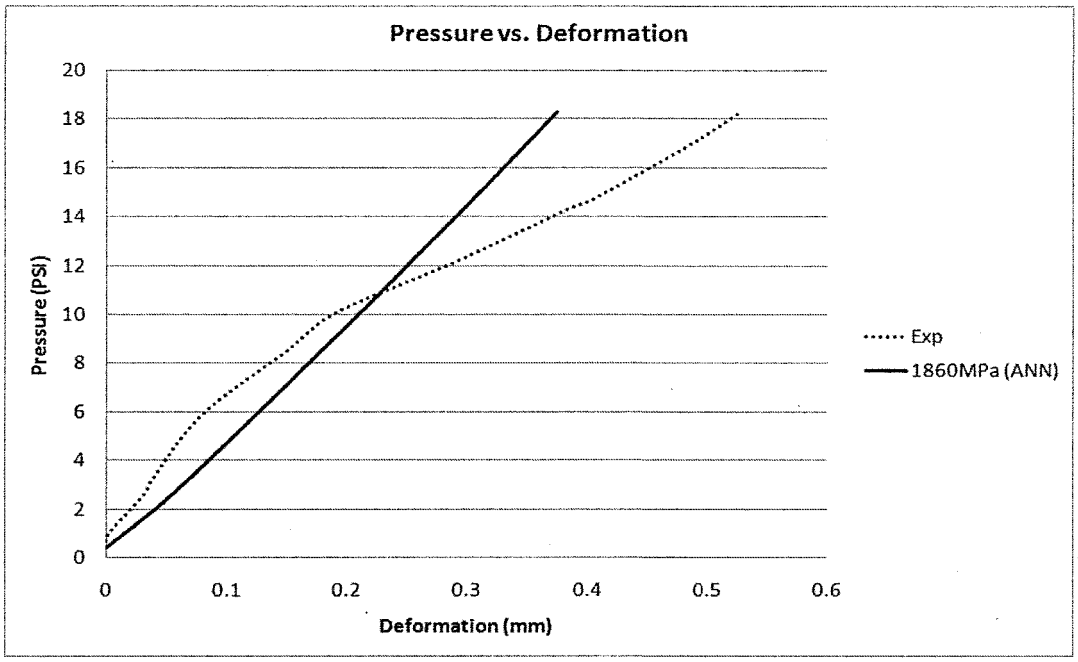

Figure 5-24 - Experimental and ANN results for the hyperelastic model of WPC60wt% at 0°C

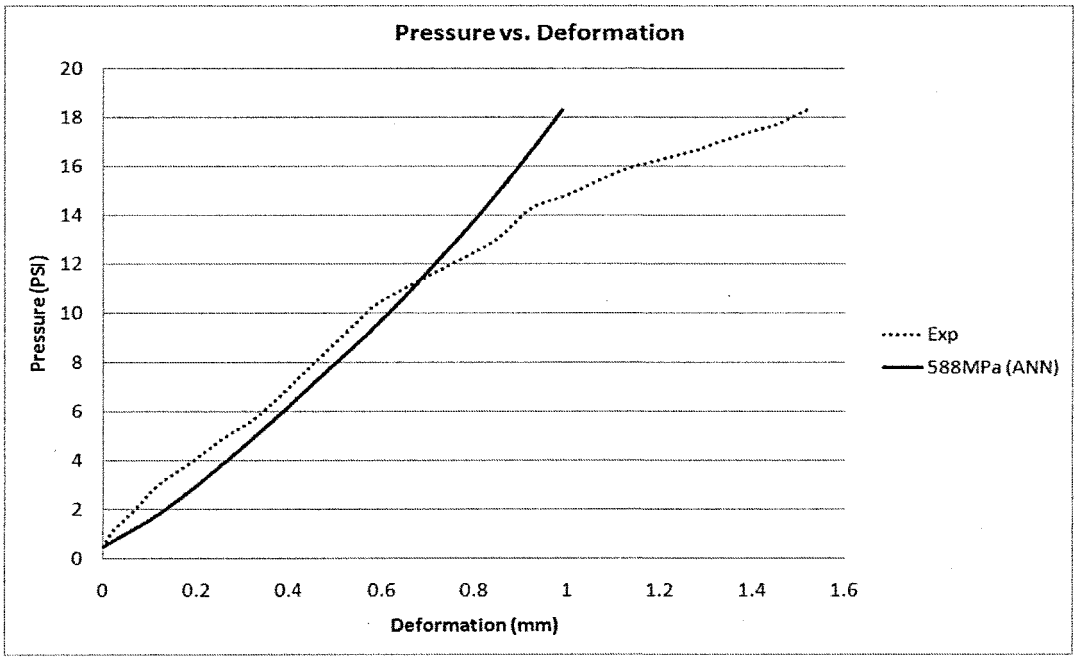

Figure 5-25 - Experimental and ANN results for the hyperelastic model of WPC60wt% at 50°C

Table 5-3 shows the summary of the results obtained from the neural network. These values correspond to Young's modulus in elastic modelling.

Table 5-3 – Material constants obtained from the neural network for elastic modelling (Young's modulus)

	−50°C	0°C	+50°C
HDPE	2.90GPa	1.81GPa	1.15GPa
WPC30%	11.14GPa	5.63GPa	3.22GPa
WPC60%	24.42GPa	12.61GPa	3.79GPa

Table 5-4 shows the values of C_1 obtained from the neural network for the neo-Hookean hyperelastic model.

Table 5-4 - Material constants obtained from the neural network for neo-Hookean hyperelastic model (C_1)

	−50°C	0°C	+50°C
HDPE	348MPa	219MPa	180MPa
WPC30%	1508MPa	705MPa	340MPa
WPC60%	5000MPa	1860MPa	588MPa

The error calculations prove that using the hyperelastic model is more appropriate for material characterization. The average relative error values for all the materials are 19% and 15% for the elastic and hyperelastic modelling, respectively. The highest and lowest relative error values are around 30% and 7%, and belong to the elastic behaviour of WPC60wt% at −50°C and the hyperelastic behaviour of WPC30wt% at 0°C, respectively. However, as explained in the literature review, in the rotorblades industry, the elastic model and Young's modulus are used in order to perform the material selection.

5.8 WPCs application in rotorblades

Figure 5-26 shows the material selection procedure. As it is indicated in Table 5-3 the WPC samples tested in this project do not meet the minimum material stiffness criterion and thus, are not good candidates for manufacturing rotorblades. However, concerning the manufacturing of rotorblades using hybrid materials, such as aluminium and composites, WPCs will be excellent candidates to be combined with aluminium.

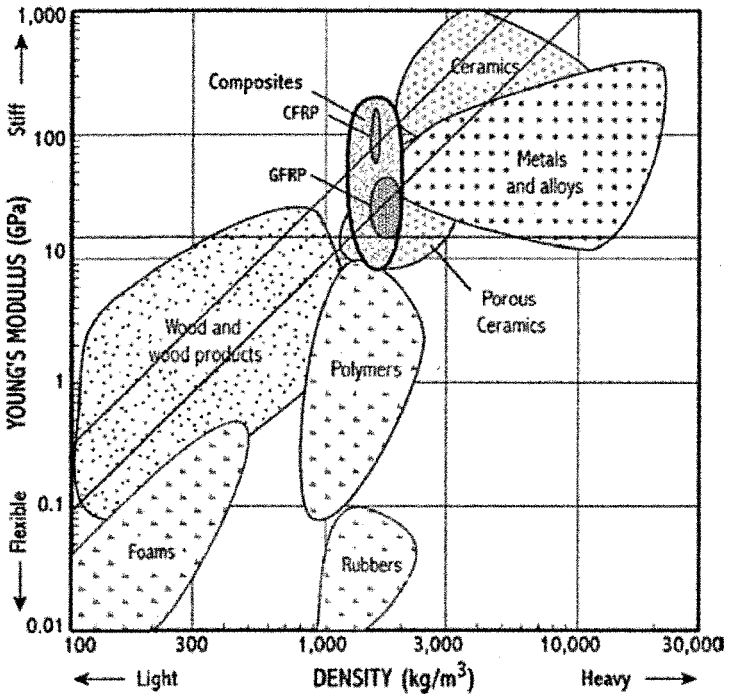

Figure 5-26 - Diagram showing stiffness versus density for all materials. The merit index for a beam $M_b = E^{0.5}/\rho$ is represented by sloping lines with M_b equal to 0.003 (lower line) and 0.006 (upper line). The criterion for absolute stiffness $E = 15\ GP\alpha$ is indicated by the horizontal line (Lovatt & Shercliff, 2002)

The samples tested in this project have randomly oriented fibres in the matrix. However, using a higher technology capable of making WPCs with oriented fibres can boost the material properties significantly.

The reason that the samples in this project are not good candidates for the rotorblades industry is mostly due to the fact that the fibres have random orientation in the material matrix. Figure 5-27 shows one of the fibre orientation requirements in a typical rotorblade.

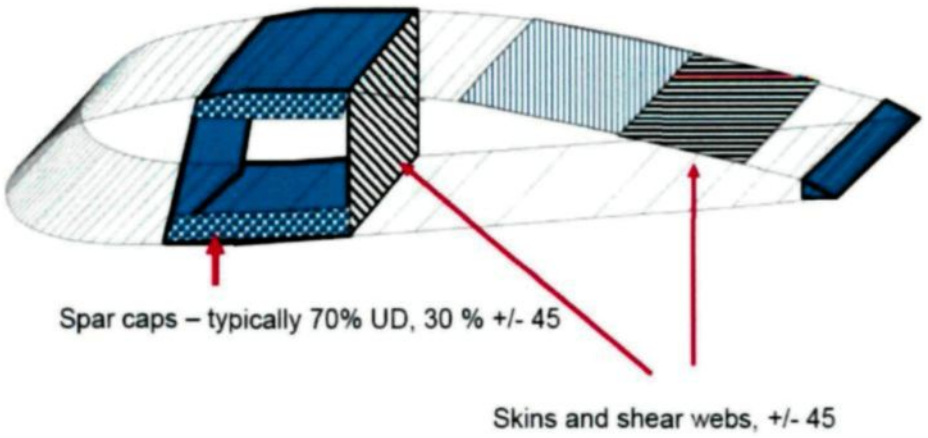

Figure 5-27 – Fibre architecture is a typical blade (Hogg, 2010)

5.9 Conclusion

In this chapter, the final goal of this project, which was to characterize the WPCs, was achieved using the Artificial Neural Networks. Based on the final results and the material constants for the elastic model (E), the material selection for the rotorblades was performed.

As discussed in this chapter, the WPC specimens used in this project do not meet the minimum material requirements in order to manufacture rotorblades. This problem is mostly due to the random orientation of the fibres in the laminate of the composite. The mechanical properties of this material can be significantly improved by using oriented fibres inside the composite material. It should be noted that WPCs studied in this project can be used in the design and manufacturing of rotorblades made with hybrid materials, such as a combination of WPC and aluminium.

In order to verify the results obtained in this chapter a set of wind tunnel experiments and computer modelling is carried out in the next chapter.

CHAPTER 6

RESULTS VERIFICATION AND ANALYSIS

6.1 Introduction

In this chapter a set of verification experiments and modelling studies are carried out in order to investigate the validity of the results obtained from the neural network. A small rotorblade is also modelled in Abaqus in order to measure and compare the deformation of the tip of the blade made of WPC and aluminium.

From the mechanical properties of the WPCs and the deformation values obtained in this project, it is understood that this composite does not meet the minimum material requirements in order to be used on its own in manufacturing rotorblades. However, it can certainly be used as the outer shell of the blade to produce the aerodynamic profile.

The study of the effects of humidity and ice accretion on the fatigue loading of the blade was outwith the scope of this project. However, at the end of this chapter a brief review of the literature on these two issues is provided in order to give the reader a view of the challenges involved in the manufacturing of rotorblades with WPCs.

6.2 Verification Experiments

To better investigate the mechanical behaviour of the specimens, a set of wind tunnel experiments are carried out. The wind tunnel at CIGELE, which is capable of delivering a maximum wind speed of 28 m/s and a minimum temperature of $-30°C$, is used for these experiments. A rectangular plate of HDPE with dimensions of 30.5 cm by 25 cm is used to observe the deformation of the plate at different combinations of temperatures and pressures (wind speeds). The thickness of the plate is 1.6 mm.

The experiments involve three different temperatures: $0°C$, $-15°C$, and $-30°C$. At each temperature the deformation under four different wind speeds (10, 15, 20, and 25 m/s) is monitored. Table 6-1 shows the results of experiments with HDPE at 0°C.

Table 6-1 – The deformation of the HDPE plate at different wind speeds at 0C

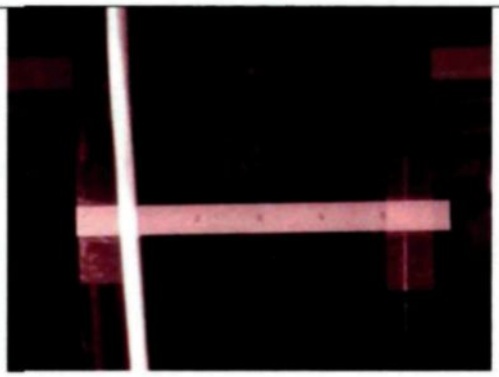

Wind speed: 0m/s

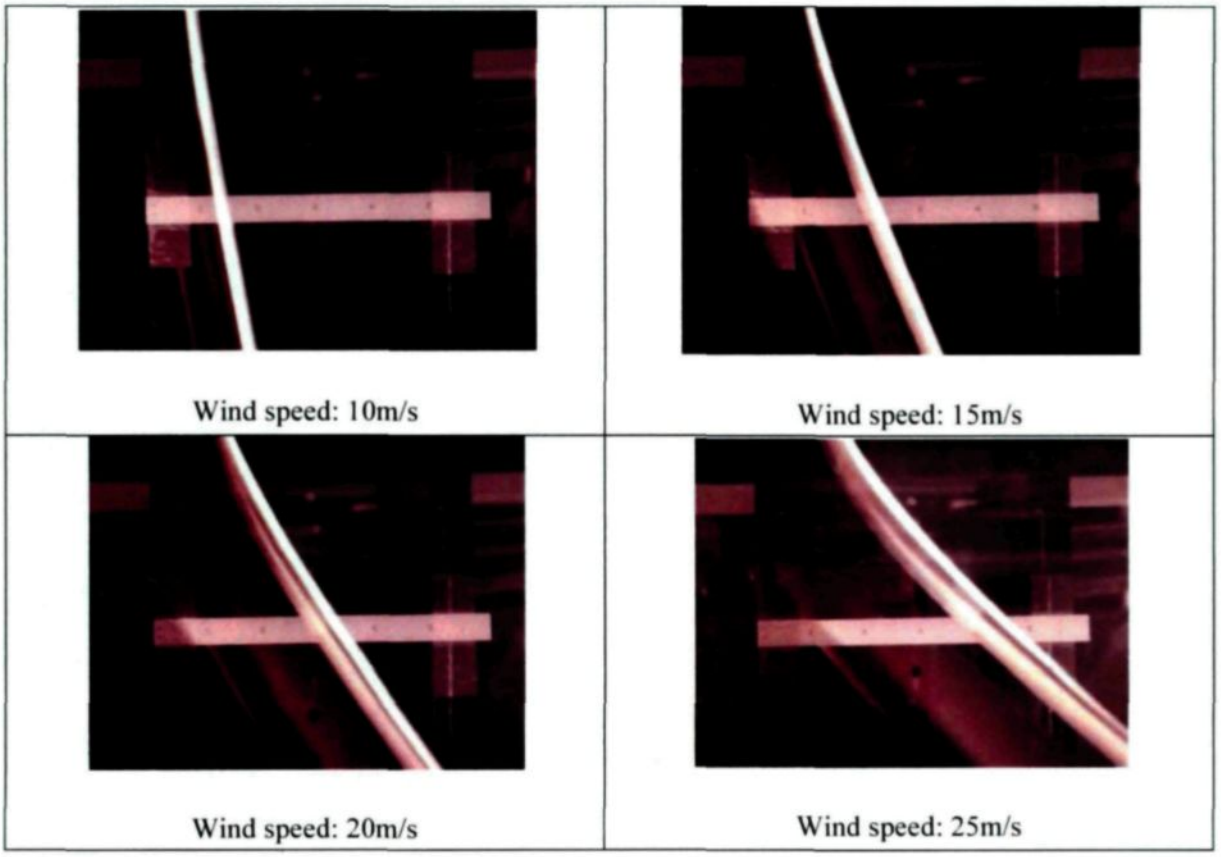

Wind speed: 10m/s

Wind speed: 15m/s

Wind speed: 20m/s

Wind speed: 25m/s

6.3 Verification modelling

In order to verify the accuracy of the material constants obtained in this project, a set of computer simulations are carried out. The results of these simulations are compared with the ones obtained from the wind tunnel experiments.

For the purpose of simulations, a rectangular plate with the same dimensions and boundary conditions as the one that is used in the wind tunnel experiments is modelled in

Abaqus using 4-node shell element. The forces on the plate are obtained using the drag force formulation (Fox, Pritchard, & McDonald, 2008).

$$F_D = \frac{1}{2}\rho_{air} V^2 C_D A \qquad (6\text{-}1)$$

F_D: drag force (N)

V: velocity of the plate relative to the wind (m/s)

C_D: drag coefficient of the plate

A: are of the plate (m^2)

The drag coefficient of the plate is assumed to be 1.86 for the turbulent flow (Fox, Pritchard, & McDonald, 2008).

The plate has been modelled using the neo-Hookean hyperelastic model. The material constant $C_1 = 219\,MPa$ that corresponds to HDPE at 0°C is used in the simulations. This material constant was obtained in the previous chapter using the neural network. The model is verified using four different wind speeds at 0°C. The density of air at 0°C is 1.3 $kg.m^{-3}$ (Van Wylen & Sonntag, 1986).

For wind speed of 10 m/s:

$$P = C_d \times P_{dynamic} = \frac{1}{2}\rho_{air} V^2 C_D = \frac{1}{2} \times 1.3 \times 100 \times 1.86 = 121\,Pa \qquad (6\text{-}2)$$

The same approach has been used to calculate the total pressure on the plate at wind speeds of 15, 20, and 25 m/s. Table 6-2 presents the total pressure values at different wind speeds.

Table 6-2 – Total pressure at different temperatures

Wind speed	Total pressure
10m/s	121 Pa
15m/s	272 Pa
20m/s	483 Pa
25m/s	756 Pa

The pressure values in the above table are used to simulate the plate deformation in Abaqus. Figure 6-1 shows a simulation of the plate under the effect of pressure.

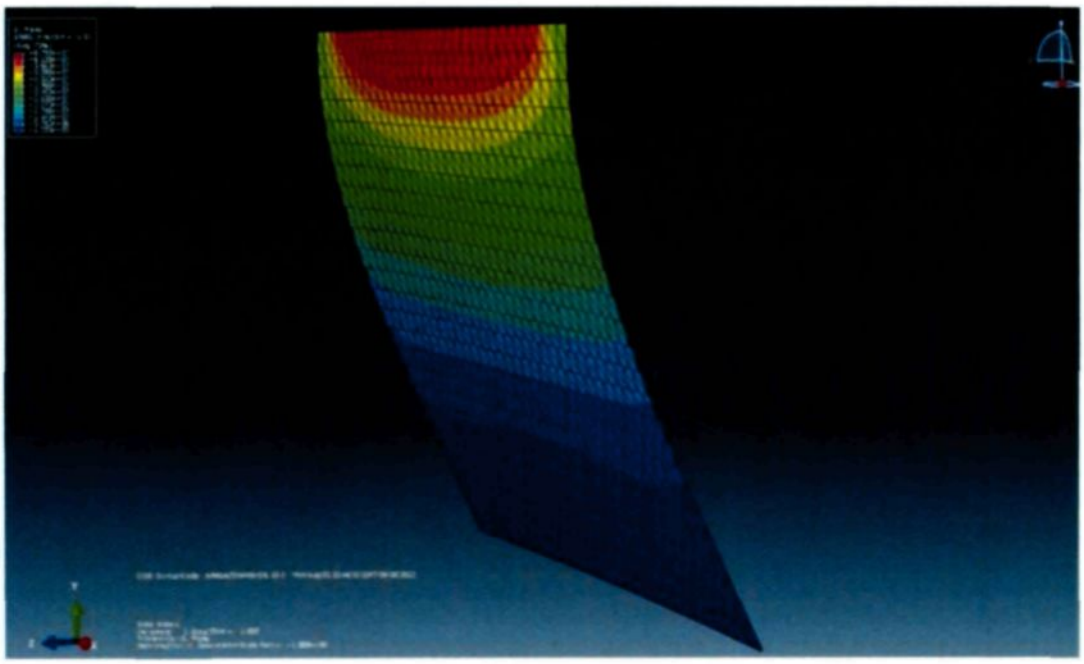

Figure 6-1 - HDPE plate under pressure modelled in Abaqus

Table 6-3 shows the deformation values of the plate obtained in the experiments and simulations.

Table 6-3 - Deformation values of the plate in both experiments and Abaqus simulations

Wind speed	Wind tunnel experiments	Simulations
10m/s	13mm	12mm
15m/s	27mm	26mm
20m/s	39mm	35mm
25m/s	59mm	52mm

It is observed that results display a good correlation and the maximum error is around 10%.

The minimum stiffness requirement of the material for the rotorblades industry is 15 GPa at ambient temperature (Brøndsted, Lilholt, & Lystruo, 2005). However, none of the WPC samples used in this study meet this minimum requirement. Nevertheless, they can be used combined with other materials such as aluminium for manufacturing rotorblades.

As the last step of the project, a small rotorblade with a length of 1 meter is modelled in Abaqus using tetrahedral element in order to observe the maximum deformation. As expected, the deformation is very large and a real size blade with the same material would lose its aerodynamic profile and hit the tower during rotation at high wind speeds.

Figures 6-2 and 6-3 show a small rotorblade with 1 meter length in both normal configuration and exposed to a wind speed of 25 m/s.

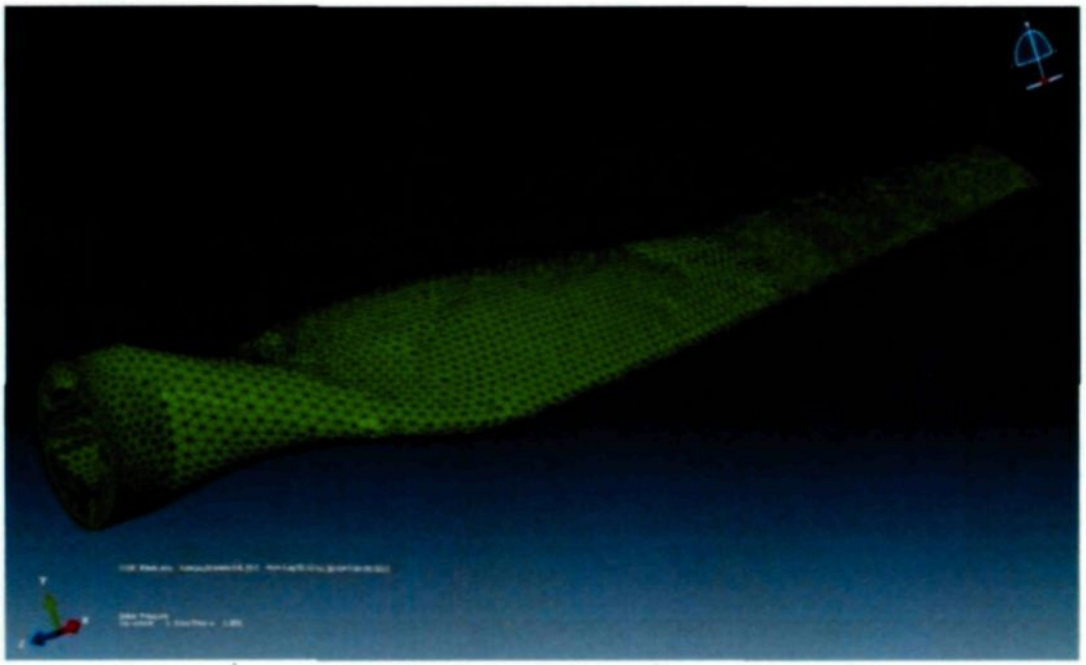

Figure 6-2 - Rotorblade with 1 meter length in normal configuration (unloaded)

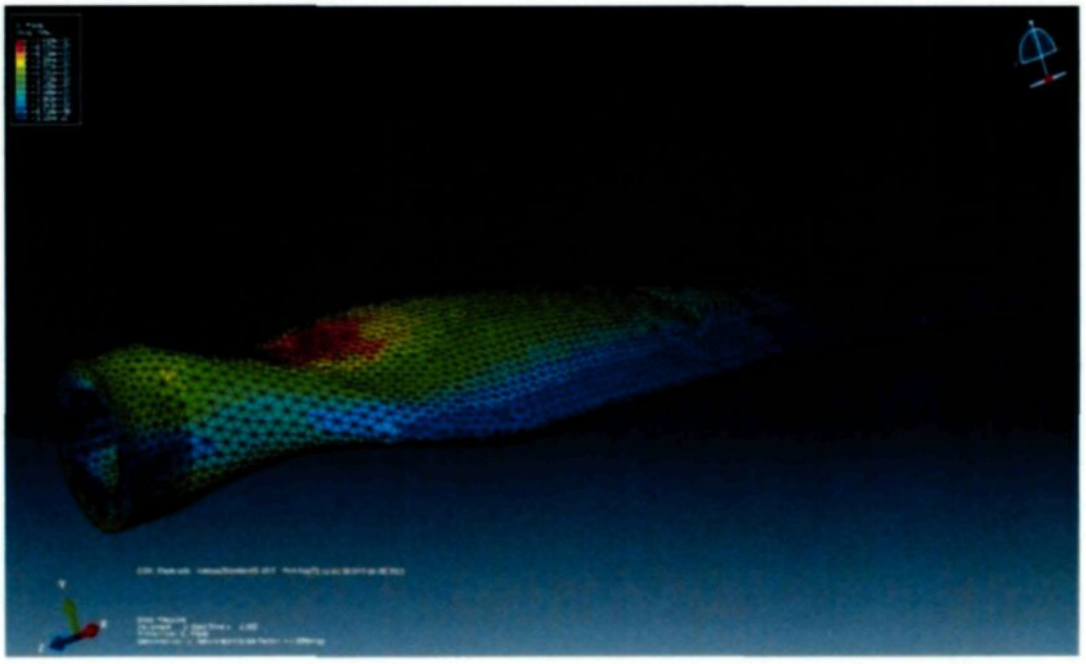

Figure 6-3 – Rotorblade with 1 meter length under the wind speed of 25m/s

The maximum deformation at the tip of the blade is calculated as 4.20 mm with WPC60wt% at 0°C, a wind speed of 25 m/s, and the elastic modulus of 12.61 GPa. This value will increase significantly in larger blades and thus, will hit the tower during rotation. However, it is a possibility to use this material combined with aluminium in order to increase the material performance. For example, a manufacturer would consider using aluminium as the central beam of the blade and produce the outer shell and the aerodynamic profile of the rotorblade using wood-plastic composites. In this case, the central beam would be the main load bearer of the blade and thus the composite would meet the material requirements as an outer shell.

The maximum deformation at the tip of the pure aluminium blade is calculated as 0.75 mm at 0°C and a wind speed of 25 m/s. Therefore, it is reasonable to believe that the deformation of the blade made with hybrid material would be somewhere between 0.75 and 4.20 mm, depending on the percentage of the aluminium in the structure. The elastic modulus of the aluminium used in the modelling is 69 GPa with Poisson ratio of 0.31 (Popov, 1976).

6.4 Effect of Humidity

One of the most remarkable features of composite materials is a relatively low water absorption compared to that of wood. When a piece of wood is immersed in water it absorbs about 25% of water by weight within 24 hours and thus becomes 25% heavier. For wood plastic composite materials, this figure is 0.7-2% after 24 hour (Klyosov, 2007).

Clearly, the belief that cellulose fibres or wood particles in composites are encapsulated with plastic is not completely valid. Particularly, it is not valid when composites contain a significant amount of cellulose, such as values above 40%. Commercial composites often contain 50–65% cellulose. There are enough cellulose particles in these composites to form extended and contacting chains, along which water penetrates into the bulk of the materials.

Water absorption mainly occurs on the outer layer of composite materials and progressively decreases into the bulk of the matrix. A relatively high water absorption by composite material leads to a higher weight of wet profile, possible decrease in their strength and increase in their deflection and swelling (Klyosov, 2007).

It is known that the longer the composite materials are immersed in water, the higher the water absorption. For composite deck boards at ambient temperature, water absorption after 24 hours is typically between 0.7 and 2% by weight, after 7 days between 1 and 5%, and after 100 days about 13–22%. These values depend on temperature and the higher the temperature, the higher the water absorption. However, water absorption by the top layer of a composite board (1 mm in depth, 50:50 mix of wood and plastic) after 24 hours is in excess of 15% (Klyosov, 2007).

Wood undergoes changes in dimension with changes in moisture content. Increase in moisture content causes swelling, and decrease content causes shrinkage. The following equation can be used in evaluating the dimensional changes (Klyosov, 2007).

$$\Delta L = LC\Delta M \tag{6-3}$$

ΔL: change in dimension (swelling)

L: initial dimension (tangential direction or radial direction) at certain moisture content

ΔM: change in moisture content

C: coefficient of dimensional change in tangential C_T or radial C_R direction.

Coefficient C numerically is a percent-dimensional change ($\Delta L/L$) at 1% change in moisture content in the material. Table 6-4 shows the values of these two coefficients.

Table 6-4 – Coefficient for dimensional change of wood within the range of moisture content of 6-14%

Species	C_T (tangential direction)	C_R (radial direction)
Cedar, yellow	0.208	0.095
Pine, ponderosa	0.216	0.133
Pine, western white	0.259	0.141
Maple, red	0.289	0.137
Red oak, commercial	0.369	0.158
Mahogany	0.238	0.172

Coefficients for dimensional change are considerable when measured in the range of moisture content of 6-14%.

Obviously, the higher the cellulose content in a WPC material, the higher the water absorption; unless each cellulose particle is fully encapsulated in the plastic and inaccessible to water. Water absorption typically shows an almost linear increase with the

increase in cellulose fraction of the composite. For example, with cellulose content in LDPE-based composite material of 10, 20, 30, 40, and 50%, the water absorption after 20-30 days is equal to 1, 4, 6, 9, and 12%, respectively (Klyosov, 2007). Another study has shown that in wood (aspen)-plastic (polypropylene) composite, the increase in wood fraction, 0, 30, 40, 50, and 60%, led to an increase in water absorption of 0, 2, 5, 7, 9, and 11%, respectively, after 10 weeks of submersion under water (Rowell, Lange, & Jacobson, 2002).

For many WPCs water absorption does not affect their flexural properties very significantly. GeoDeck provides the data from the experiments on hollow deck boards at maximum water absorption, that is, up to its saturation level. For a relatively dry composite board (moisture content 0.63%), the ultimate load was 870 lb, flexural strength was 1909 psi, and flexural modulus was 304,000 psi. After the board was saturated with water, the ultimate load was 928 lb, flexural strength was 2037 psi, and flexural modulus was 296,000 psi. This means that its flexural strength slightly increased, and flexural modulus was in the order of its initial value (Klyosov, 2007).

In another experiment with a different commercial solid WPC board, the ultimate load at ambient conditions was 1521 lb (moisture content 0.34), flexural strength was 3692 psi, and flexural modulus was 430,000 psi. After the board was saturated with water, the ultimate load was 1616 lb, flexural strength was 3789 psi, and flexural modulus was 448,000 psi. This means that its flexural strength and modulus for the water saturated board slightly increased again, by 2.6 and 4.2%, respectively (Klyosov, 2007).

6.5 Effect of icing on wind turbine fatigue loads

The extreme conditions occurring in cold climate regions affect wind turbines in different ways. The effects of ice accretion on fatigue loads of a rotorblade are very significant.

In the planning phase of a wind farm, only standard wind measurement data is available. With required considerations for cold climates, in the first step, the duration of icing and the type of icing will be evaluated. A simple and robust model should be used taking into account the marginal basis of meteorological parameters that normally are known from the site measurements. This information is used to simulate the aerodynamic effects and effects caused by mass imbalances in a common simulation program to generate site specific turbine loads (Frohboese & Anders, 2007).

6.5.1 Icing

Ice accretion is the process of ice building up on the surface of a structure. Different type of icing on structures can occur. However, with respect to ice accretion on rotorblades, only two major types of ice accretion are discussed: precipitation icing and in-cloud (atmospheric) icing (Frohboese & Anders, 2007).

6.5.2 Precipitation icing

This type of ice occurs as result of freezing rain or accumulation of wet snow and it depends on the rate of precipitation, the wind speed, and the air temperature.

6.5.3 In-cloud icing

In-cloud or atmospheric icing occurs when the structures are inside clouds and the water droplets in the air start to freeze on the structure. Rime ice is the most common type of in-cloud icing. Rime ice forms ice vans on the windward side of the object and leads to heavy loading by ice. In-cloud icing depends on the dimensions of the object exposed, the wind speed, liquid water content in the air, the drop size distribution and the air temperature (Frohboese & Anders, 2007).

6.5.4 Estimation of the ice accretion

In ISO 12494 different approaches are given to predict the in-cloud icing accretion using metrological measurement data. Standard wind measurements contains only limited data and the water content in the air and the drop size distribution are not known. Therefore, in most studies, the data from ISO 12494 standards is used (Frohboese & Anders, 2007).

The amount of accreted rime ice at each time step can be calculated according to the following equation:

$$m_i = 0.11 v_i T_i W \quad [kg/m] \tag{6-4}$$

In this equation only the wind speed, v, and the duration time, T, in the in-cloud condition in hours are taken into account. W is the width of the object.

6.5.5 Rotorblade icing

In order to estimate the ice accretion on a rotorblade, its geometrical shape is assumed to act like a slender object or large object and thus the shape is approximated as a round bar (Frohboese & Anders, 2007).

In ISO 12949, it is suggested that different models of ice accretion should be applied for slender or large objects. The distribution is made above and below diameters of 300 mm. This is applied concerning the thickness of the actual blade section. The ice masses and vane length are calculated by calculating the wind speed at hub height, determining the rotational speed and calculating the effective wind speed at the blade section.

In the GL's Wind Guideline, it is suggested that the mass distribution is assumed at the leading edge of the rotorblade. It increases linearly from zero in the rotor axis to the maximum value μ_E at half the radius, and then remains constant up to the outermost radius (Frohboese & Anders, 2007).

$$\mu_E = \rho_E k c_{min} (c_{max} + c_{min}) \tag{6-5}$$

μ_E = mass distribution on leading edge of the rotorblade at half the rotor radius [kg/m]

ρ_E = density of the ice (700 kg/m^3)

$k = 0.00675 + 0.3\ exp(-0.32\ R/R1)$

R = rotor radius

$R1$ = 1 m

c_{max} = maximum chord length

c_{min} = chord length at the blade tip, linearly extrapolated from the blade contour

6.5.6 Fatigue loads

Frohboese (Frohboese & Anders, 2007) studied the effect of ice accretion on fatigue loads of rotorblades. For the fatigue load calculation, different effects are taken into account in his study. For the ice accretion, the following effects concerned with the ice mass are altered independently and their influence on the loads is compared separately:

- Mass imbalance (2 blades iced)
- Duration of icing situation
- Distribution of ice on the blade
- Wind speed during ice event
- Ice density and the type of ice

The following parameters have been investigated but are found to be of minor interest:

- Ice centre of gravity with respect to chord length
- Turbulence intensity of the wind during ice event

The effects concerned with the aerodynamic properties are altered independently and the influence on the loads is compared separately:

- Iced aerodynamic coefficients
- Aerodynamic imbalance

In the results, Frohboese (Frohboese & Anders, 2007) reports that the main load increase is due to the unbalance in the rotor when considering two blades iced and one free, that is the worst case scenario. The influence of the additional mass without imbalance is not important. A maximum load increase of 2.3% was found. The most significant load increase is in the direction perpendicular to the thrust force direction as the imbalance will lead to the accelerations in this direction. The mass imbalance in the centre of the hub has no effects on the loads for the rotorblades. Overall, the loads increase with the increasing ice density, duration of icing event, and wind speed during the icing event. Load increases occur mainly at the following components:

- Hub stationary shear force (non-rotating hub F_y)
- Hub stationary vertical force (non-rotating hub F_z)

- Tower top shear force (tower top F_y)
- Tower top vertical force (tower top F_z)
- Tower base bending moment (tower base M_y)

6.6 Conclusion

In this chapter the results from the neural network were verified by a set of wind tunnel experiments on an HDPE plate and a computer simulation in Abaqus. The maximum deformation of a small rotorblade made of WPC and aluminium was measured in Abaqus.

The results of this project show that WPCs are not sufficient to be used alone in the rotorblades industry. However, they can be used to produce the aerodynamic shell of a rotorblade that has a central beam made of aluminium.

Finally, a brief review of the humidity and ice accretion problems on fatigue loading of the rotorblades was presented.

CHAPTER 7

CONCLUSIONS AND RECOMMENDATIONS

7.1 Conclusions and contributions of the thesis

An original experimental setup was designed and developed in CIGELE laboratory at University of Quebec at Chicoutimi. The test setup is to model the bubble inflation technique and it was installed inside an environmental test chamber to carry out experiments at cold temperatures.

A data acquisition program was developed in the LabVIEW software in order to collect the experimental data. The results of several experiments with HDPE and wood-plastic composites at different temperatures are recorded in an organized database. The values of air pressure, airflow, duration of experiments, temperature, and deformation are recorded and can be used as an accurate database for future research.

The bubble inflation of the specimens was modelled mathematically and it was implemented into the neo-Hookean hyperelastic model.

The experimental results of HDPE and wood-plastic composites with 20, 30, 40, 50, and 60wt% of wood fibres under the combined effect of temperature and pressure were

reported. The membranes were tested within the temperature range of −50°C to +50°C with 25°C increments.

Five pressure-vs-deformation graphs at five different temperatures were prepared for each class of material. The performance of different materials was compared at different temperatures. It was observed that wood plastic composites and HDPE are elastic in response to pressure at cold temperatures. The experimental results show that the deformation of the membranes, under the same pressure, decreases with decreasing temperature. Therefore, it is understood that the material has a higher stiffness at cold temperatures even though it may become more brittle.

From the comparison of deformation of different membranes, it is observed that the addition of wood fibre increases the material performance under pressure at different temperatures. However, at colder temperatures the difference between the deformations of WPCs and HDPE is much higher as compared to high temperatures.

For the purpose of material characterization, the elastic and hyperelastic behaviour of the membranes were modelled using the finite element package, Abaqus. The deformation values with different material constants from Abaqus were used to prepare a learning library for the artificial neural network. The optimum material constants for HDPE and WPCs were obtained using this original approach to material characterization.

The stress distribution in the membrane under pressure was reported in Abaqus. The von Mises stresses were reported for both elastic and hyperelastic models at three different

temperatures. It was observed that the maximum stress occurs on the edge of the membrane that is clamped to the experimental setup and the minimum stress is in the pole of the inflated membrane.

A neural network code was developed for the purpose of this project to obtain the optimum material constants. The experimental results were used as the input, and the output of the network was the optimum material constant. The material constants for HDPE and WPCs with 30 and 60wt% of wood fibre were reported at $-50°C$, $0°C$, and $+50°C$. The material constants in this project correspond to Young's modulus and C_1 for elastic and hyperelastic models, respectively.

A set of wind tunnel experiments and computer modelling in Abaqus was performed in order to verify the results from the neural network. A rectangular plate of HDPE with dimensions of 30.5 cm by 25 cm was used to observe the deformation of the plate at different combinations of temperatures and pressures (wind speeds). A rectangular plate with the same dimensions and boundary conditions as the one that was used in the wind tunnel experiments was modelled in Abaqus. The plate was modelled using the neo-Hookean hyperelastic model. The material constant $C_1 = 219\,MPa$ that corresponds to HDPE at $0°C$ was used in the simulations. This material constant was obtained using the neural network. It was observed that the results display a good correlation and the maximum error is around 10%.

In order to investigate the application of WPCs in the rotorblades industry, the performance of this material was compared with the material requirements of the industry. As a result of this study, it was understood that WPC samples tested in this project do not meet the minimum material stiffness criterion and thus, are not good candidates for manufacturing rotorblades. The reason that the samples in this project are not good candidates for the rotorblades industry is mostly due to the fact that the fibres had a random orientation in the composite's matrix.

As the last step of the project, a small rotorblade with the length of 1 meter was modelled in Abaqus to observe the maximum deformation. As expected, the deformation was very large and a real size blade with the same material would lose its aerodynamic profile and hit the tower during rotation in high wind speeds. The maximum deformation at the tip of the blade was calculated as 4.20 mm with WPC60wt% at 0°C, wind speed of 25 m/s, and the elastic modulus of 12.61 GPa. However, it is a possibility to use WPCs combined with aluminium in order to increase the material performance. For example, a manufacturer would consider using aluminium for the central beam of the blade; and the outer shell and aerodynamic profile of the rotorblade using wood-plastic composites. In this case, the central beam would be the main load bearer of the blade and thus, the composite would meet the material requirements to be used as an outer shell. Finally, the effects of humidity and icing on wood-plastic composites and rotorblades were discussed in order to understand the challenges involved in the application of WPCs in the rotorblades industry.

7.2 Recommendations for future work

The hyperelastic and viscoelastic behaviour of wood-plastic composites and polymeric materials at high temperatures, such as thermoforming temperatures, have already been investigated (Erchiqui, Ozdemir, Souli, Ezzaidi, & Dituba-Ngoma, 2011). The effects of processing method and fibre size on the structure and properties of WPCs have also been studied (Migneault, Koubaa, Erchiqui, Chaala, Englund, & Wolcott, 2009). However, the effects of the length and orientation of the fibres inside the laminate on the mechanical properties of WPCs at cold temperatures have not yet been investigated. Manufacturing WPC specimens with oriented fibres requires advanced equipment capable of controlling the fibres orientation in the matrix.

The study of effects of humidity and freezing cycles on the mechanical behaviour of WPCs at cold temperatures is strongly recommended. In cold climate regions, such as Canada, humidity and freezing cycles play a vital role in the material's performance and life cycle. Therefore, it is essential to have detailed knowledge of these effects on the material's performance before applying WPCs to any particular industry.

Ice accumulation phenomenon and the effects of humidity, temperature, and wind speed can also be investigated on ice strain adhesion on the surface of WPCs. It is also recommended to study the available solutions for developing a hydrophobic coating on the surface of the material in order to increase its performance in humid conditions.

References

Aleksander, I., & Morton, H. (1995). *An Introduction to Neural Computing.* Intl Thomson Computer Pr (T); 2nd Sub edition .

Alexander, H. (1971). The tensile instability of an inflated cylindrical membranes as effected by an axial load. *Int. J. Mech Vol. 13* , 87-95.

Benjeddou, A., Jankovich, E., & Hadhri, T. (1993). Determination of the parameters of Ogden's law using biaxial data and Levenberg-Marquardt-Fletcher algorithm. *J. of Elastomers and Plastic, Vol. 25* , 224-248.

Bird, R. B., Armstrong, R. C., & Hassager, O. (1987). *Dynamics of Polymeric Liquids Vol. 1.* New York: Fluid Mechanics, Wiley.

Blaise, A., Andre, S., Delobelle, P., Meshaka, Y., & Cunat, C. (2012). Identification of the True Elastic Modulus of High Density Polyethylene From Tensile Tests Using an Appropriate Reduced Model of the Elastoviscoplastic Behaviour. *eprint arXiv: 1206.4268* .

Brøndsted, P., Lilholt, H., & Lystruo, A. (2005). *Composite Materials for Wind Power Turbine Blades.* Materials Research Department Risoe National Laboratory, DK 4000 Roskilde, Denmark.

BTM Consult ApS. (2010). *International Wind Energy Development - World Market Update 2010.* BTM, Consult ApS, Denmark.

Carroll, M. M., & Hayes, M. A. (1996). *Nonlinear Effects in Fluids and Solids.* New York and London: Plenum Press.

Christensen, R. (1980). A nonlinear theory of viscoelaticity for applications to elastometrs. *Journal of Applied Mechanics ASME Trans. No 47* , 762-768.

Clemons, C. (2002). Wood-Plastic Composites in the United States - The Interfacing of Two Industries. *Forest Products Journal , 25* (6), 10-18.

Collier, C. S. (2010). *From the aircraft wings to wind turbine blades: NASA Software comes back to earth with green energy applications.* Hampton, VA.: Collier Research Corporation.

Collier, C., & Ashwill, T. (2011). Materials and design methods look for the 100-m blade. *Windpower Engineering Development* , 88-90.

Dennis, J. E., & Schnabel, R. B. (1983). *Numerical Methods for Unconstrained Optimization and Nonlinear Equations.* SIAM.

Derdouri, A., Erchiqui, F., Bendada, A., Verron, E., & Peseux, B. (2000). Viscoelastic behaviour of polymer membranes under inflation. *Rheology 2000-XIII International Congress on Rheology, Vol.13* , 394-396.

Erchiqui, Derdouri, A., Gakwaya, A., Godard, G., & Garcia-Rejon, A. (2001). *Finite element and experimental analysis of dynamic inflation of thermoplastic material.* Laval University.

Erchiqui, F., & Derdouri, A. (2005). Analyse experimentale et numerique du comportement des membranes thermoplastique en ABS et en HIPS dans le procede de thermoformage. *The Canadian Journal of Chemical Engineering Vol. 83, No. 3* , 527-536.

Erchiqui, F., & Kandil, N. (2006). Neuronal Networks Approach for Characterization of Softened Polymers. *Journal of Reinforced Plastics and Composites* , 463-473.

Erchiqui, F., Derdouri, A., & Verron, E. (2001). Analyse expermentale et numerique en soufflage libre d'une membrane thermoplastique. *Entropie* , 235-236.

Erchiqui, F., Ozdemir, Z., Souli, M., Ezzaidi, H., & Dituba-Ngoma, G. (2011). Neural Netwroks Approach For Characterisation of Viscoelastic Polymers. *The Canadian Journal of Chemical Engineering* , 1303-1310.

Feng, W. W. (1992). Viscoelastic behaviour of elastomeric membranes . *Journal of Applied Mech.* , Vol. 59, pp. S29-S34.

Fox, R. W., Pritchard, P. J., & McDonald, A. T. (2008). *Intoduction to Fluid Mechanics.* Wiley; 7 edition .

Frohboese, P., & Anders, A. (2007). Effects of Icing on Wind Turbine Fatigue Loads. *Journal of Physics: Conference Series* .

Griffin, D. A., & Ashwill, T. (2003). Alternative composite materials for megawatt-scale wind turbine blades: Design considerations and recomended testing. *Journal of Scolar Energy Engineering 125 (4): 515* .

Hau, E. (2005). *Wind Turbines: Fundamentals, Technologies, Application, Economics.* Springer.

Haykin, S. (1998). *Neural networks a comprehensive foundation.* Prentice Hall 2nd edition.

Hogg, P. (2010). *Wind turbine blade materials.* University of Loughborough: SUPERGEN Wind - Wind Energy Technology.

Jones, R. (1975). *Mechanics of Composite Materials.* New York: McGraw-Hill.

Joye, D. D., Poehlein, G., & Denson, C. D. (1973). A bubble inflation technique for the measurment of viscoelastic properties in equal biaxial extensional flow. *II Trans. Soc. Rheol., Vol. 17, No. 2* , 287-302.

Klyosov, A. A. (2007). *Wood-Plastic Composites.* John Wiley & Sons.

Levenberg, K. (1944). A method for the solution of certain nonlinear problems in least squars. *Quarterly of applied mathematics 2* , 164-168.

Lodge, A. (1964). Elastic Liquids,. *Academic Press* .

Lovatt, A., & Shercliff, H. (2002). Materials Selection and Processing - Cambridge University.

MacKay, D. (1992). Bayesian interpolation in neural computation. *Neural Computation , 4* (3), 415-447.

Marquard, D. (1963). An algorithm for the least-squars estimation of nenlinear. *J. Applied Mathematics 11* , 431-441.

Meissner, J., Raible, T., & Stephenson, S. E. (1981). Rotary clamp in uniaxial and biaxial rheometry of polymer melts. *J. Rheol., Vol. 25, No.1* , 1-28.

Migneault, S., Koubaa, A., Erchiqui, F., Chaala, A., Englund, K., & Wolcott, M. P. (2009). Effects of processing method and fiber size on the structure and properties of wool-plastic composites. *Composites: Part A* , 80-85.

Ogden, R. (1972). Large deformation isotropic elasticity-on the correlation of theory and experimental for incompressible rubberlike solids. *R. Soc. Lon. Vol. A326* , 565-584.

Popov, E. P. (1976). *Mechanics of Materials.* New Jersey: Prentice Hall.

Rivlin, R. S. (1948). Large Elastic Deformation of Isotropic Materials - IV: Further Development og the General Theory. *Phil. Trans. R. Soc. A241* , 379-397.

Rivlin, R. S., & Saunders, D. W. (1951). Large elastic deformations of isotropic materials - VII. Experiments on deformation of rubber. *Phil. Trans. R. Soc., Vol. A243* , 251-288.

Rowell, R. M., Lange, S. E., & Jacobson, R. E. (2002). Effects of moisture on aspen-fibre/polypropylene compoites. *Progress in Wood Fibre Plastic Composites.* Toronto: Canadian Natural Composites Council.

Stergiou, C., & Siganos, D. (1996). Neural Netwroks. *SURPRISE 96, Vol 4* .

Treolar, L. (1944). Stress-strain data for volcanised rubber under various type of deformation. *Trans. Faradar Soc., Vol.40* , 59-77.

Van Wylen, G. J., & Sonntag, R. E. (1986). *Fundamentals of Classical Thermodynamics.* Wiley; 3rd edition.

Verron, E., Marckmann, G., & Peseux, B. (2001). Dynamic inflation of non-linear elastic and viscoelastic rubberlike membrane. *Int. J. Numer. Meth. Eng., Vol. 50, No. 5* , 1233-1251.

Verron, E., Pesseux, B., Derdouri, A., & Connolly, R. (1997). Bubble inflation of heat-softened polymeric membranes above the glass transition temperature. *The 16th Canadian Congress of Applied mechanics* , (pp. 81-82). Quebec, Canada.

Watt, W., & Perov, P. (1985). *Strong Fibres, Handbook of Composites.* Amsterdam: North Holland/Elsevier.